© Copyright 2019

Mike Jeon

Iron Oxide Nanoparticles for Targeted Cellular Imaging and Drug Delivery

Mike Jeon

A dissertation

submitted in partial fulfillment of the

requirements for the degree of

Doctor of Philosophy

University of Washington

2019

Reading Committee:

Miqin Zhang, Chair

Christine Luscombe

Richard Ellenbogen

Program Authorized to Offer Degree:

Materials Science and Engineering

University of Washington

Abstract

Iron Oxide Nanoparticles for Targeted Cellular Imaging and Drug Delivery

Mike Jeon

Chair of the Supervisory Committee:
Professor Miqin Zhang
Materials Science and Engineering

Iron oxide nanoparticles (IONPs) have drawn significant interest in the field of biomedicine due to their intrinsic magnetic properties that allow contrast under magnetic resonance imaging (MRI). With proven biocompatibility, biodegradability, and flexible surface chemistry for a variety of applications, IONPs have been used as theranostic agents, combining therapy and diagnosis in a single formulation. Despite their potential, few IONPs have transitioned to the clinic due to the challenges of achieving high drug loading while maintaining proper size and stability to bypass biological barriers, minimizing off-target drug release to prevent side effects, and increasing specificity to minimize non-specific uptake for increased efficacy.

Many strategies can overcome these limitations. To increase specificity, incorporating active targeting by conjugating targeting agents onto IONPs can specifically bind and label intended sites. This approach can open up labeling and imaging of novel sites, such as neurons,

when using MRI for diagnostic purposes. For drug delivery purposes, chemotherapeutics can be loaded onto IONPs with controlled release to prevent drug leakage and the consequent side effects. Incorporating targeting agents can further reduce off-target drug release. While IONPs have historically seen great utility as T_2 contrast agents, these applications could be further expanded by designing IONPs for T_1 contrast enhancement.

This dissertation documents the development of iron oxide nanoparticle systems intended to overcome the shortcomings of various iron oxide nanoparticle applications with novel applications. First, we used IONPs conjugated with a dopaminergic neurolabeler to actively target the dopamine transporter to label and image dopaminergic neurons under MRI. The neurolabeler enhanced targeting and uptake of IONPs 3-fold over control IONPs. Labeling and imaging the brain using PET/SPECT is a tool to diagnose neurological disorders, such as Parkinson's disease. By using IONPs, this technique can be expanded to MRI to improve upon the shortcomings of PET/SPECT. Next, IONPs were loaded with paclitaxel to treat breast cancer cells. Due to their severe hydrophobicity, paclitaxel were bound close to the core of the IONP via an acid-cleavable ester bond, with longer chain PEG providing steric stabilization and hydrophilicity to stabilize the IONP. The paclitaxel loaded IONPs were further modified with folic acid, used as a targeting agent to bind to the folate receptors that are commonly over-expressed in breast cancer cells. The folic acid labeled and paclitaxel loaded IONP enhanced uptake by 2-fold, demonstrated controlled release of paclitaxel, and produced significantly higher cytotoxicity in breast cancer cells compared to free paclitaxel.

Despite their proven efficacy as T_2 contrast agents, IONPs have been hindered in their translation to clinical imaging applications due to the inherent limitations of T_2 contrast agents. The benefits of T_1 contrast has led to gadolinium-based contrast agents (GBCAs) serving as the

dominant contrast agents in the clinic, while their severe side effects have highlighted the need for a biocompatible alternative. IONPs have the ability to serve as an alternative T_1 contrast agent to GBCAs, but their potential has not been fully explored. Using the fundamentals of T_1 contrast, we developed and characterized a T_1 IONP. It demonstrated excellent physiological properties ideal for biological applications, with T_1 contrast capabilities confirmed through phantom MR imaging.

Finally, with clinical translation in mind, we investigated optimization of freeze-drying methods to prolong the stability of IONPs. Aqueous solutions can hydrolyze and degrade NPs, prohibiting long-term stability in solutions. Freeze-drying offers means of removing water to prevent degradation, yet freeze-drying stresses can cause irreversible damage to NPs. Cryoprotectants have been used to minimize or rid these freeze-drying stresses, yet their effects on IONPs have not been explored. A variety of cryoprotectants were tested for their effects on maintaining size, stability, zeta potential, and magnetic properties after freeze-drying on IONPs produced by the Zhang group and commercially available IONPs. Sucrose was the most effective cryoprotectant, with 10 wt.% sucrose offering IONPs great stability up to 6 months while preserving size, zeta potential, and magnetic properties.

TABLE OF CONTENTS

LIST OF FIGURES

LIST OF TABLES

ACKNOWLEDGEMENT

I would first like to express my sincere gratitude and appreciation to my advisor, Miqin Zhang, whose mentorship and support has guided me through the pursuit of my degree. Her passion and drive for research has been an inspiration during my graduate career, and this dissertation would not have been possible without her. I would also like to thank my committee members, Richard G. Ellenbogen, Christine K. Luscombe, and Robert E. Synovec, for taking their time out of their busy schedules to provide valuable feedback and support on my graduate work.

I am grateful to all Zhang lab members who have contributed to my dissertation. I would like to specifically thank my mentor, Zachary R. Stephen, for his patience, guidance, and encouragement through my graduate career. It has been a pleasure working with such bright, intelligent, and gifted individuals in the Zhang lab. I also thank the Department of Materials Science and Engineering for their various forms of support during my graduate study, and extend my gratitude to my undergraduate advisors: Lara Estroff, Chad Lewis, and Kyle Lancaster, who pushed me to pursue a graduate degree in science and engineering.

I am indebted to my family and friends who have cheered me on with unconditional love during the pursuit of my degree. Thank you to my parents (Byeung Bae Jeon and Jung In Jeon) and brother (Sunki Jeon) for their support during my entire academic career. Special thanks to Michael, Mackenzie, and Gina for the endless encouragement. I am endlessly grateful for all their love and support through this endeavor.

Thank you.

1. Introduction and rationale

The field of theranostics aims to overcome the shortcomings of traditional disease diagnosis and therapy by combining them into one approach. Materials at the nanoscale have drawn particular interest due to their prolonged circulation and navigation in the body along with intrinsic properties that make them detectable via imaging modalities. These nanomaterials are being engineered for specific targets, including the brain, a great challenge in the medical field. The ability to monitor treatment in real time is revolutionary, as doctors will be able to ensure targeted delivery of drugs and adjust the dosage as necessary to prevent overtreatment, which can cause harmful side effects, or undertreatment, which can be insufficient to achieve the desired result.[1]

An important consideration in the development of theranostic nanomaterials is the mechanism by which they can image cellular targets.[1] For example, liposomes can be loaded with optically active fluorophores. This offers continuous, real-time imaging, but suffers from poor resolution and limited penetration depth.[2] Radionuclide-labeled nanomaterials can be detected through positron emission tomography (PET) imaging or single-photon emission computed tomography (SPECT). These imaging methods offer excellent penetration depth and sensitivity, but suffer from poor spatial resolution.[2] Additionally, these radiotracers have extremely short half-lives, are toxic, and are not always compatible with targeting molecules, limiting possible cellular targets.[3-6]

The other important aspect is the mechanism by which these nanomaterials can load therapeutics. These drugs must be held in circulation and only released when the intended target is reached. Therapeutics, especially chemotherapeutics, are typically hydrophobic, making it

difficult to develop water-soluble systems that can load and deliver these drugs to intended targets. Liposomes have hydrophobic cores that can load chemotherapeutics via hydrophobic interactions, but are limited by their large size. Similarly, carbon nanotubes and fullerenes can load hydrophobic drug molecules in their cores, but their toxicity prohibits their utility. Magnetic nanomaterials have been coated in biocompatible polymers with functional groups that covalently bind to therapeutics. These functional groups can also be used to bind targeting agents that can help deliver the therapeutics to the intended target. [1]

Among the many classes of nanomaterials, iron oxide nanoparticles (IONPs) have attracted a considerable amount of interest due to intrinsic properties that can solve the many issues that cloud the current field of theranostics. IONPs have shown great biocompatibility, biodegradability, and well-established methods of synthesis.[7-9] IONPs also exhibit useful magnetic properties; IONPs with core sizes smaller than 20 nm are superparamagnetic, a property providing inherent contrast for magnetic resonance imaging (MRI).[10] MRI offers high soft tissue contrast, spatial resolution, and penetration depth, allowing detection of these NPs anywhere in the body.[1,10] Additionally, IONPs can be coated in a myriad of different polymers with various functional groups that not only stabilize the NPs, but also conjugate therapeutics, targeting agents, and imaging moieties.

This dissertation will explore novel applications of IONPs for targeted drug delivery, targeted cellular imaging, and MRI contrast. It is organized as follows:

Chapter 1 provides an introduction and rationale for this research, including discussion of current limitations and motivations.

Chapter 2 reviews applications of IONPs as MRI contrast agents. Fundamentals of MRI will be discussed, along with the two classes of MRI contrast agents. Limitations of current MRI contrast agents will be addressed along with potential solutions using IONPs. Other topics are MRI acquisition methods, along with multimodal imaging using IONPs.

Chapter 3 reviews applications of IONPs as theranostic agents. Strategies to specifically label cellular targets will be introduced, including passive and active targeting. Methods to load therapeutics will be discussed, along with methods for passive and active release.

Chapter 4 reviews the necessary design criteria for IONP-based theranostic agents to succeed in vivo for clinical translation. It addresses the impact of core size, morphology, composition, surface coating, hydrodynamic size, and zeta potential. Different synthetic routes in producing these iron oxide nanoparticles will be discussed, including co-precipitation and thermal decomposition methods with the classical nucleation theory in mind.

Chapter 5 demonstrates a novel application of IONPs in label and image dopaminergic neurons using MRI for potential use in diagnosing Parkinson's disease. The chapter will demonstrate how IONPs conjugated with cocaine analogues can specifically label and image neurons in vitro.

Chapter 6 demonstrates how therapeutics and targeting agents can be conjugated onto IONPs to not only specifically target breast cancer cells, but also deliver chemotherapeutic drugs with controlled release to effectively kill breast cancer in vitro.

Chapter 7 discusses the development of IONP systems for T_1 MRI contrast. This chapter includes an in-depth look at parameters that control IONP efficacy as a T_1 contrast agent. Using

these parameters enabled development and characterization of an IONP-based T_1 contrast agent, and demonstration of its capabilities with phantom MRI.

Chapter 8 presents a method to preserve IONPs for longer shelf-life in clinical conditions by freeze-drying with cryoprotectants. Two different IONPs, one produced by our lab and one commercially available, are tested with various cryoprotectants to study the effects of cryoprotectants in maintaining IONP properties when freeze-dried.

Chapter 9 summarizes the major findings of this work with conclusions.

2. Iron oxide nanoparticle for medical magnetic resonance imaging (MRI)

Magnetic resonance imaging (MRI) is an indispensable, non-invasive diagnostic tool in the clinic due to its strong soft tissue contrast and specificity, spatial resolution, and penetration depth. Images can also be acquired without the use of harmful ionizing radiation or radiotracers, which often also have short blood half-lives.[11-15] Significant research has been conducted in the development of MRI contrast agents that can be used to better target and image various biological targets. Specifically, iron oxide nanoparticles have drawn considerable attention due to their unique magnetic properties and their proven biocompatibility and biodegradability.[7,9,10,16]

Unlike many other nanoparticle-based contrast agents, IONPs have demonstrated minimal toxicity that have opened up IONPs to an array of applications including diagnosis of various diseases such as cancer[17], neurological disorders[18], and cardiovascular disease[19]. This success has led the Food and Drug Administration (FDA) to approve of several formulations of IONPs for clinical use: Feridex IV® for liver and spleen imaging[20], Lumiren® for bowel imaging[21], and Combidex® for lymph node metastases imaging.[22] IONPs have gone beyond just imaging, and are now also used as a vehicle to target and deliver therapeutics with the potential for broad clinical applications.[10,23-25]

2.1. Fundamentals of MRI

^{1}H is the dominant isotope for clinical MRI due to the high abundance of water in the human body. During a scan, the magnetic moments of hydrogen nuclei in the body exhibit a net alignment parallel to a strong external magnetic field in the z-direction, as seen in **Figure 2-1**.[26]

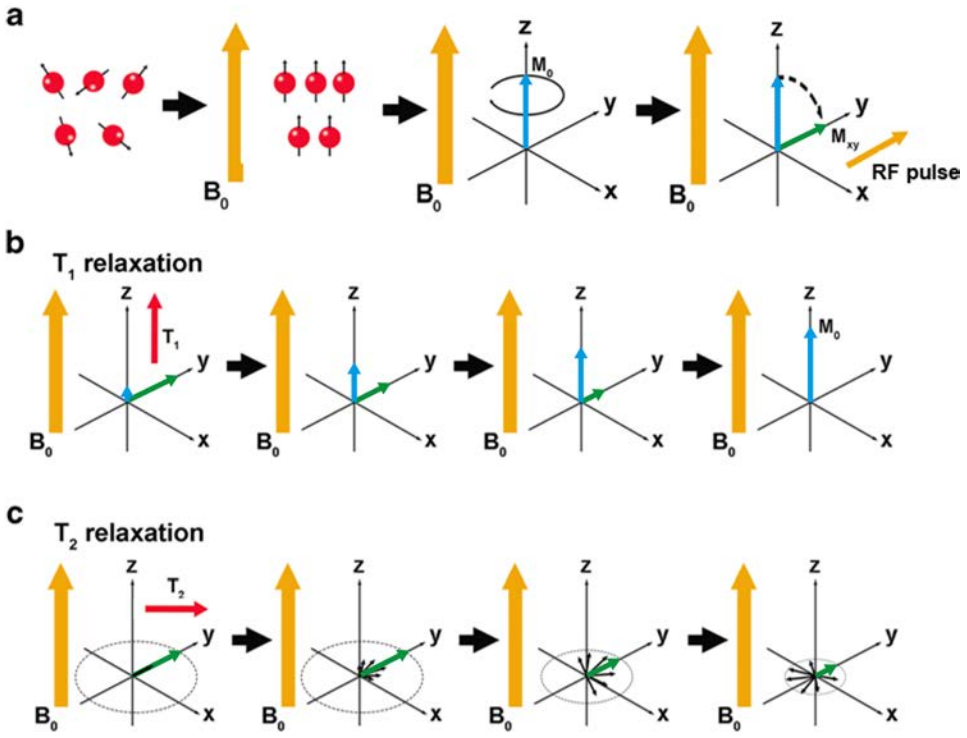

Figure 2-1. Schematic representation of the basic principles of MRI. (a) When an external magnetic field B_0 (orange arrow) is applied, protons (red spheres) tend to align with B_0 (note that the depiction here unrealistically shows all protons aligned with B_0, but there is only a slight preference for this alignment). This alignment results in a net magnetization vector (M_0, blue arrow). When an orthogonal RF pulse is applied, M_0 tilts 90° into the transverse (x-y) plane (M_{xy}, green arrow). Magnetization returns to equilibrium through two processes: T_1 and T_2 relaxation. (b) T_1 is a measure of the time it takes the initial longitudinal magnetic moment (M_0) to recover. (c) T_2 measures the loss of the transverse magnetic moment (M_{xy}) due to dephasing. (Reproduced with permission from[26], Copyright © 2019 Mastrogiacomo).

An orthogonal radiofrequency (RF) pulse is applied to rotate the magnetic moment 90 degrees into the transverse (x-y) plane (**Figure 2-1a**). When this RF pulse is removed, the hydrogen nuclei go through a recovery process, in which the magnetic moments return to the original, energetically preferable equilibrium. During the recovery process, two relaxation times are measured: spin-lattice (longitudinal, T_1) relaxation and spin-spin (transverse, T_2) relaxation.[10,27,28]

T_1 relaxation occurs when spins lose energy by interacting with their environment (hence, spin-lattice). Because alignment with the external magnetic field is a lower energy state for these

spins, alignment is more heavily favored as the spins lose energy. As the net alignment returns to the direction of the external magnetic field, the initial net magnetic moment is recovered (**Figure 2-1b**), and this recovery is measured. Contrast agents facilitate this energy loss through dipole-dipole interactions between water molecules and metal ions in the contrast agent's core. Energy exchange happens most efficiently when water molecules encounter a magnetic field fluctuating near the Larmor frequency (42.58 MHz/T for hydrogen protons), so T_1 contrast agents are most effective when their rotational motion matches this frequency. The rapid tumbling time of water molecules is slowed to nearer the Larmor frequency by interaction with the contrast agent, promoting energy loss and accelerating the recovery of the longitudinal magnetic moment.

T_2 relaxation reflects a loss of net magnetization in the transverse plane, perpendicular to the applied magnetic field. When spins are tipped 90 degrees by the RF pulse, their initial net alignment with the external magnetic field becomes a net phase coherence of their precession in the transverse plane, and thus a small magnetic moment (**Figure 2-1c**). T_2 is a measure of the loss of this transverse net magnetization. All processes causing T_1 relaxation will also cause the precession of these spins to decohere, but they are not the only mechanisms affecting T_2 relaxation. Contrast agents impact T_2 by creating local magnetic field inhomogeneities.[28,29] The induced fields create regions where the Larmor frequency, which depends on field strength, differs from that of the applied longitudinal field. As this characteristic precession of hydrogen protons is altered, the spins fall out of phase, and any net transverse magnetization is lost.

The relaxation rates, denoted as r_1 and r_2 relaxivities, are the inverse of the T_1 and T_2 relaxation times, respectively. It is important to note that the ratio of r_2/r_1 is a key parameter in distinguishing T_2 and T_1 contrast agents. T_2 contrast agents possess high r_2 relaxivity, hence have

large r_2/r_1 ratio. In comparison, T_1 contrast agents should have high r_1 relaxivity, with the r_2/r_1 ratio being smaller, ideally close to 1.[30]

2.2 T_2 contrast agents vs. T_1 contrast agents

The resolution of MRI is improved by the use of contrast agents, which enhance contrast by either shortening the longitudinal (T_1) or transverse (T_2) relaxation times of water protons.[30,31] T_1 contrast agents produce positive (bright) contrast while T_2 contrast agents produce negative (dark signal) contrast **(Figure 2-2)**.[30]

IONPs make effective T_2 contrast agents due to their high-saturation magnetization, which is largely responsible for r_2 relaxivity.[30] When under an external field, IONPs develop an induced magnetic field, and perturb the spin precession in the neighboring areas, causing phase decoherence and negative contrast in MR images. The coupling between the magnetic moments of the IONPs and the magnetic moments of water protons causes spin dephasing and T_2 relaxation, which decreases the signal intensity and appears dark in MR images, thus called negative contrast. T_2 contrast agent efficacy is largely dependent on the magnetization of the material, which can be altered via size, shape, and composition. IONP-based T_2 contrast agents have demonstrated great success, with numerous formulations being approved by the FDA.[20-22]

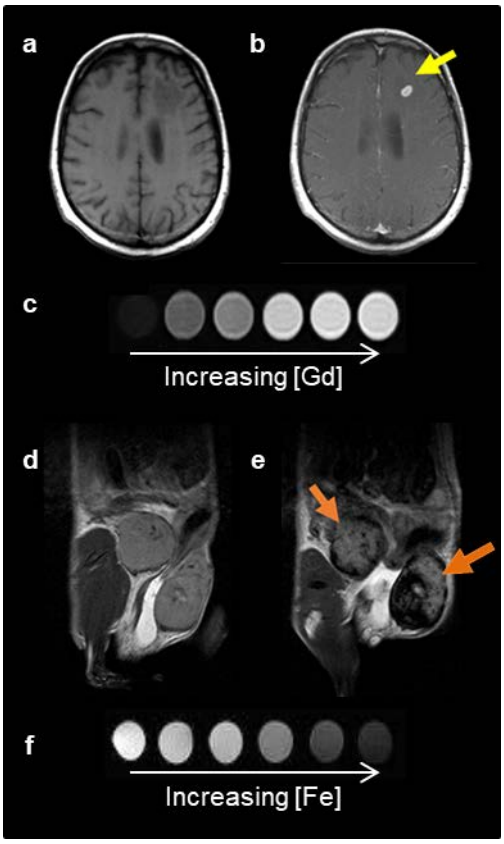

Figure 2-2. Two classes of MRI contrast agents. Pre- (a) and post- (b) GBCA T_1-weighted MRI on a brain metastasis in a melanoma patient. (c) T_1 contrast agents decrease the spin-lattice relaxation time, increasing signal with increasing concentration, and produce bright contrast images. Pre- (d) and post- (e) IONP-based contrast agent T_2-weighted MRI on inflamed mouse mammary gland tumors. (f) T_2 contrast agents decrease the spin–spin relaxation time, decreasing signal with increased concentration, and produce dark contrast images. (Reproduced with permission from[32-34], Copyright © 2017 Serkova, Copyright © 2016 Ivyspring International Publisher, Copyright © 2018 Elsevier Ltd.)

IONPs have also proven to possess superparamagnetism when their core sizes are smaller than 20 nm.[35] Superparamagnetic IONPs (SPIONs) have a combination of the high magnetization of bulk magnetite and the paramagnetic behavior of iron ions (**Figure 2-3**). This means the protons of SPIONs can be magnetized by an external magnet, but upon release, the magnetization decays and each SPION behaves independently. SPIONs are able to create large magnetic field inhomogeneities, making them highly effective at promoting rapid dephasing in the transverse plane, and thus significant negative contrast enhancement.[10]

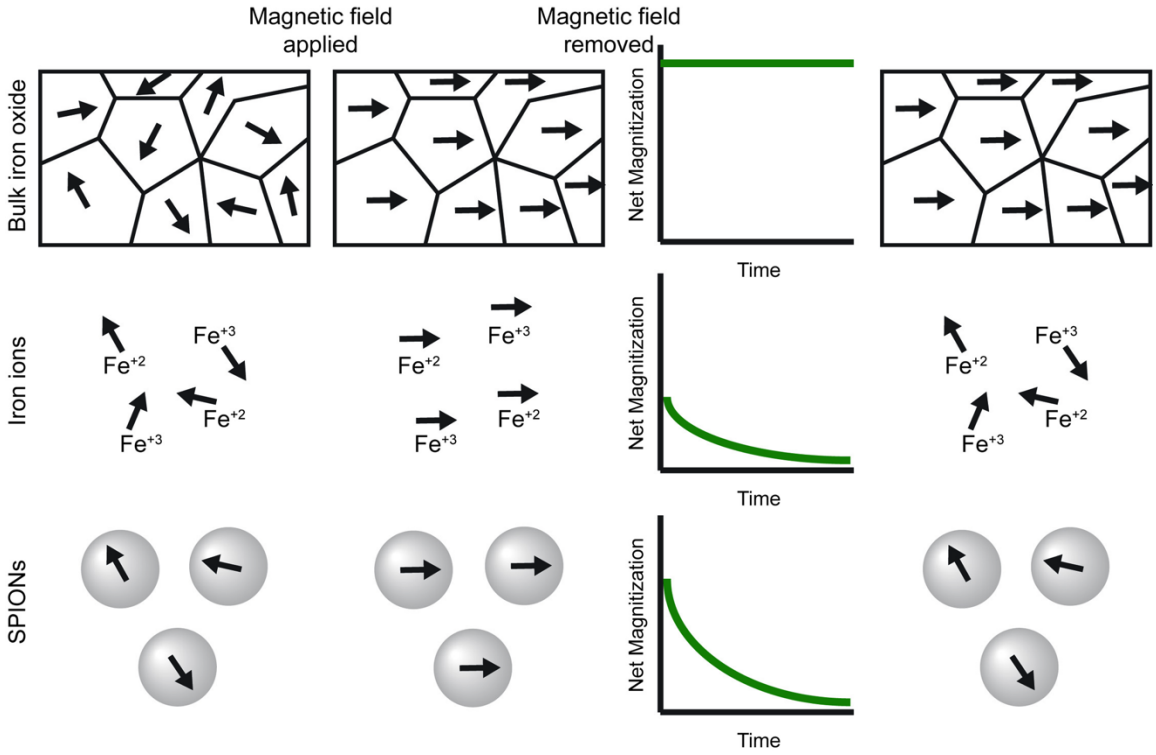

Figure 2-3. The effects of an external magnetic field on bulk magnetite (top), iron ions (middle), and SPIONs (bottom). Before an external magnetic field is applied, all magnetic moments are random. When an external magnetic field is applied, all magnetic moments are aligned in that direction. After the magnetic field is removed, bulk magnetite retains its net magnetization. The net magnetization of SPIONs are higher than that of iron ions, but less than bulk magnetite. When the magnetic field is removed, both SPIONs and iron ions relax to equilibrium.

Currently, Gd^{3+}-based contrast agents (GBCAs) are the only T_1 contrast agents used in the clinic. The superior T_1 contrast enhancement of GBCAs can be explained in terms of inner-sphere (IS) and outer-sphere (OS) mechanisms.[30,36] The inner-sphere component is influenced by the number of fast-exchanging water molecules within the inner sphere, the characteristic tumbling time of the agent (τ_R), and the characteristic water proton residence lifetime (τ_m) of the inner-sphere molecules. The outer-sphere component arises from the translational diffusion of water molecules near the Gd^{3+} ions. The overall r_1 relaxivity is the sum of the inner-sphere and the outer-sphere relaxivities. Gd^{3+} has 7 unpaired valence electrons, each of which can interact with water molecules; this along with having minimal magnetization gives GBCAs a low r_2/r_1 ratio and superior T_1 contrast enhancement.[36] Increasing water interaction slows the tumbling

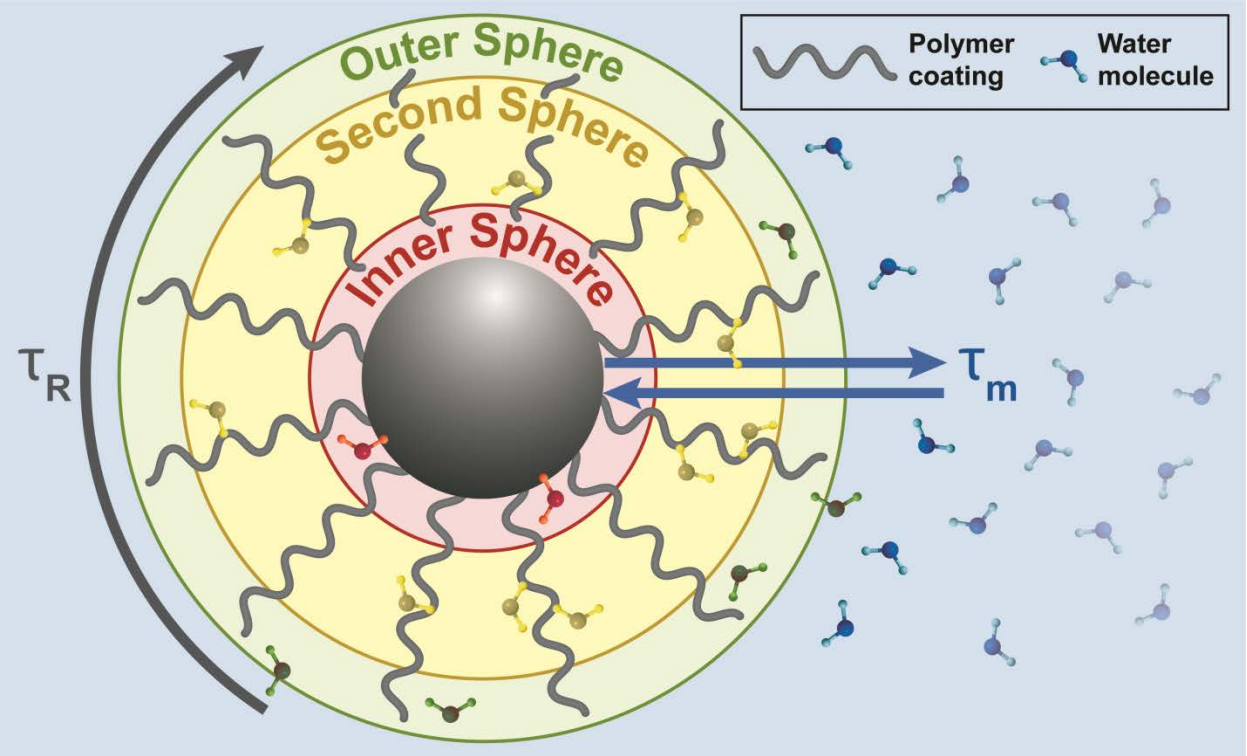

Figure 2-4. A depiction of time parameters and regions contributing to relaxivity. The time parameters are rotational correlation time (τ_R) and water residence time (τ_m for direct core interaction, τ'_m for polymer interaction). The inner sphere consists of water molecules interacting directly with metal ions of the IONP core (red). The second sphere consists of water molecules transiently bound to the polymer (yellow). The outer sphere refers to water molecules indirectly affected by magnetic field fluctuations at the surface of the IONP system (green). The motion of water molecules through these three spheres determines relaxivity.

rate of the water to nearer the Larmor frequency, which allows it to recover its magnetic moment more quickly. These parameters are illustrated in **Figure 2-4** as applied to an IONP contrast agent, with the addition of a second-sphere contribution to r_1 due to interactions between water molecules and IONP surface coating.

2.3 Limitations of current contrast agents

Despite some success of IONP-based T_2 contrast agents, they have several limitations. T_2 contrast agents have intrinsically high susceptibility that induces a long-range magnetic field, which perturbs neighboring tissues and distorts the background image, a phenomenon known as

the Blooming effect.[30] Due to this effect, the location of T_2 contrast agents can be easily misidentified with other hypointense areas caused by bleeding, calcification, and metal deposits. Additionally, in regions of low signal, the presence of IONPs can make it difficult to distinguish contrast enhancement.[37,38] As T_1 contrast agents are composed of paramagnetic ions, they do not affect the magnetic homogeneity or the anatomical backgrounds, allowing for clear detection of the contrast agent. Given the limitations of T_2 contrast agents, they are used far more frequently in the clinic than are iron oxide-based T_2 contrast agents.

Despite the efficacy of GBCAs as T_1 contrast agents, severe side effects have been observed. GBCAs have shown to cause fatal nephrogenic systemic fibrosis (NSF), leading to fibrotic skin contractures, and in extreme cases, resulting in fractured bones or even death.[39-43] Additionally, these heavy metal complexes have been reported to cause brain lesions, which are exacerbated in patients with liver or kidney problems. Due to the potential of severe side effects caused by GBCAs, the FDA has issued numerous warnings about the possible long-term deposition of Gd in the brain, and research into the potential harms is ongoing.[44-46] The toxicity is compounded by the short blood half-life of GBCAs[36,47-49], which may require patients to undergo multiple doses to acquire necessary images. Although rare, these side effects have raised trepidations about the toxicity of Gd and its potential to accumulate in the body, especially among patients who require frequent MR imaging. Clearly, there is a need for a more biocompatible T_1 contrast agent.

2.4 Potential of IONPs as T_1 contrast agents

IONPs have demonstrated long blood half-lives, low toxicity, and flexible surface chemistry.[10,50] Crucially, IONPs are known to be effectively cleared from the body, and have a

natural mechanism for degradation, a drastic departure from the toxicity of GBCAs.[9,51-53] Despite use as T_2 contrast agents, IONPs also have the potential to be effective at T_1 relaxation due to their large number of unpaired electrons. Depending on the composition of iron oxide used to form IONPs, the iron ion may possess up to 5 unpaired valence electrons available to interact with water molecules. The surface coating of the IONP can also increase T_1 relaxivity, providing sites for additional second-sphere interactions. Therefore, the key to producing effective IONP-based T_1 contrast agents is to tailor the interaction of IONPs with water molecules to increase r_1 relaxivity while reducing magnetization to decrease r_2. Mechanisms to design IONP-based T_1 contrast agents will be further discussed in Chapter 7.

2.5 MRI acquisition methods

Though IONPs can be designed to maximize transverse or longitudinal relaxivities, MRI acquisition methods can also be altered to maximize IONP detection. Acquisition methods that can detect low signal from IONPs are crucial for transition of IONPs to clinical settings. Lower detection limits can allow lower dosages of IONPs, and also potentially open up new sites to be imaged using MRI. As IONPs are typically used as T_2 contrast agents, only T_2 acquisition methods will be discussed.

MRI acquisition methods for detection of IONPs have been based on T_2-weighted spin echo (SE) pulse sequences and T_2*-weighted gradient echo (GRE) pulse sequences that give quantitative and qualitative information of the location, respectively.[54-56]

There is a linear dependence between the sensitivity of IONP detection with increasing resolution, and a hyperbolic dependence between the sensitivity of IONP detection with increasing signal-to-noise ratios.[55] By using this information, the maximum IONP detection

capability would be achieved with high resolution and high signal-to-noise ratio. However, this leads to impractically long acquisition times.

To improve upon IONP detection limits with reasonable acquisition times, nontraditional pulse sequences such as fluid attenuated inversion-recovery (FLAIR) has been developed for IONP applications.[57,58] The FLAIR sequence was designed to negate signals from fluids to increase the limit of IONP detection, and found success in diagnosing various central nervous system diseases, though it is also limited by long acquisition times.[59] This sequence was improved by the development of the FLAIR echo-planar imaging (FLAIR EPI) sequence. The FLAIR EPI sequence nullifies signals from periportal tissue, cysts, and vascular structures on top of fluids, to increase the detection limit while hastening the acquisition time. The FLAIR EPI sequence found success in detecting liver tumors in human patients.[59] Lastly, the fast imaging employing steady-state acquisition (FIESTA) sequence has been able to detect femtomolar quantities of IONPs in vitro. This detection limit is comparable to those achieved by positron emission tomography (PET) and single-photon emission computed tomography (SPECT).[55]

2.6. Multimodal imaging using iron oxide nanoparticles

MRI has found great clinical utility due to its unlimited penetration depth, high spatial resolution, and excellent soft tissue contrast without the need for ionizing agents. However, MRI also suffers from setbacks such as limited sensitivity to contrast agents, including IONPs.[60] To circumvent this issue, IONPs have been designed to incorporate other imaging moieties that can work in tandem to provide more accurate in vivo information.

Fluorophores are a common imaging moiety that can be conjugated onto IONPs to provide optical contrast, which offers superior sensitivity compared to MRI. Fluorophores of

various excitation and emission wavelengths are already commercially available, with convenient routes of labeling that offer diverse utility. However, optical imaging suffers from poor penetration depth, so while it may be useful in a research setting, its clinical utility is limited. These limitations are further exacerbated by the short half-lives and hydrophobicity of fluorophores.

Radionuclides have also been incorporated into IONPs to provide dual PET/MRI.[61-63] PET offers exceptional sensitivity to radionuclides, however it suffers from poor spatial resolution. Therefore, dual PET/MRI is used to achieve highly detailed anatomical MR images by tracing radionuclides via PET.[62] Though dual PET/MRI works well in theory, it has practical limitations: both MRI and PET have acquisition times that can run from minutes to hours, and radionuclides have incredibly short half-lives, requiring the contrast agents to be synthesized on site.[3-6] Multimodal imaging possesses great potential in overcoming the limitations of MRI and IONP-based contrast agents. However, due to insufficient multimodal imaging instrumentation, the potential has yet to be translated clinically.

3. Iron oxide nanoparticles for theranostics

After successful development of IONPs, the transition from a simple contrast agent to a theranostic agent has been a natural progression. Due to their proven biocompatibility, biodegradability, facile synthesis, and ease with which properties can be tailored, IONPs have been used successfully in vivo at the cellular and molecular level as diagnostic tools, while providing the basis to delivering therapeutics.[25] Typically, the polymeric coating of the iron oxide core can be manipulated to include targeting agents and therapeutics. To use IONPs successfully as theranostic agents, requires an ability to target and accumulate at the desired sites. The method of accumulation is categorized into two classes: passive and active targeting. Additionally, IONPs must be able to deliver the therapeutic to the desired sites. Similar to targeting, the therapeutic delivery can be passive and active. Passive delivery relies on drug release from the delivery vehicle as it degrades, while active release depends on activation from various stimuli, such as pH and redox response.

3.1 Iron oxide nanoparticles for cellular labeling: passive targeting and active targeting

Early IONPs relied on passive targeting through the enhanced permeation and retention (EPR) effect. Cancerous tissues have leaky vasculature, which allows NPs of size <100 nm to pass through the vessels into the tumor microenvironment.[64-66] The NPs remain in the microenvironment for a time that is significantly longer than the blood clearance of the NPs, allowing them to be retained in the tumors. The poor lymphatic drainage of cancerous tissues can further help NPs avoid clearance from the tumor.[67]

The EPR effect has been exploited by various nanoparticle systems, including iron oxide nanoparticles. IONPs have been used to label brain tumors[68], breast tumors[68], and pancreatic tumors[69] via the EPR effect. However, the EPR effect has its limitations, as not all tumors exhibit the EPR effect, and the permeability of the leaky vasculatures is not homogeneous.[70] However, the passive effects of EPR are modest, offering no more than a 2-fold increase in therapeutic delivery compared with normal organs.[71] Also, the EPR effect relies on long circulation times, increasing the likelihood that the drug can extravasate into healthy tissues for undesired side effects.[67]

Active targeting strategies have been used to accumulate IONPs at desired targets to overcome the limitations of the EPR effect. Active targeting takes advantage of unique molecular markers of desired cells, such as nutrient receptors or over-expressed growth factors.[72] The IONP system can target these markers by incorporating agents capable of binding to them, including peptides, antibodies, aptamers, and small molecules.[73] For instance, many solid tumors overexpress the folate receptor, so folic acid has been used to actively target these solid tumors.[74-77] Another method uses chlorotoxin, a peptide derived from the venom of a deathstalker scorpion, and has high affinity for tumors of neuroectodermal origin.[78] Active targeting has also improved the distribution of IONPs within the targeted tissue. Homogenous distribution in vivo can help maximize relaxivity to improve detection by MRI.[79,80]

It is important to note that active targeting does not negate the EPR effect, but works in tandem with it. Targeting IONPs improves specificity to the desired target and the EPR effect allows IONPs to accumulate and retain in the desired tissues for a longer time. As stated previously, the EPR effect on its own offers less than a 2-fold increase in drug delivery,

concentrations not sufficient to treat most cancers.[67] Therefore, active targeting must be encouraged and used to maximize the efficacy of IONP-based theranostic systems.

3.2 Iron oxide nanoparticles for drug delivery: drug loading

IONPs possess great potential as drug delivery systems as they can be tailored to bypass many biological barriers to specifically accumulate in diseased cells. As IONPs are composed of iron oxide cores, therapeutics are typically incorporated into the polymeric coating, though early attempts at using IONPs as drug delivery systems incorporated chemotherapeutics bound to the iron oxide core via secondary bonding.

In a study by Nadeem et al., 10 nm IONPs coated with polyvinyl alcohol were loaded with doxorubicin (DOX).[81] It was assumed that hydrogen binding enabled DOX molecules to be held on the IONP surface. Binding a hydrophobic molecule to the core can affect the IONP's magnetic properties, as it can create a hydrophobic layer around the IONP core. This hydrophobicity prevents water molecules from interacting with the IONP system, which is likely to reduce r_1 and r_2 relaxivities. Additionally, chemotherapeutic drugs bound by secondary bonding may not be secure and cause drug leakage that may harm healthy cells and cause off-target issues. To overcome this issue, covalent bonds have been commonly used to bind drugs more securely to the IONP system.

Functional groups are essential to the polymeric coating when using covalent bonding to conjugate drugs onto IONPs. Common polymer coatings, such as PEG or dextran, either naturally possess or have been engineered to have terminal functional groups for convenient conjugation of chemotherapeutics (e.g., amine, alcohol, thiol). Kohler et al. conjugated methotrexate (MTX) on the surface of amine-terminal PEG-coated IONPs to treat glioma cells.

MTX is a chemotherapeutic drug used to treat various cancers, including brain, lung, breast, and blood. Kohler's IONP system has demonstrated enhanced cytotoxicity to glioma cells compared to free MTX.

Compared to polymeric drug delivery systems, IONPs suffer from poor drug loading capacity as they can only be loaded onto the surface of the iron oxide core.[82-85] In contrast, polymeric systems such as micelles and liposomes are capable of high loading capacity due to their hydrophobic cores. Taking inspiration from hydrophobic cores, Hsiao et al. used a hydrophobic layer between the iron oxide core and a hydrophilic polymer exterior.[86] This amphiphilic polymer coating was composed of hexanoyl-chitosan-PEG. The inner hydrophobic layer was composed of hexanoic acid, while the outer hydrophilic layer was composed of chitosan-PEG. This arrangement allowed excellent paclitaxel (PTX) loading (31.1%) without sacrificing water solubility, and the system displayed great efficacy in treating glioblastoma cells.

An important point is that therapeutic agents that can be delivered using IONPs are not limited to small chemotherapeutic molecules. IONPs have shown potential to deliver many other therapeutics, including macromolecules such as peptides, antibodies, siRNA, and DNA. IONP systems may comprise multiple therapeutics, allowing versatile options for treating diseases.

3.2.1 Drug release: passive and active release

Therapeutics loaded onto IONPs require release mechanisms. Earlier developments used passive release, as the IONP degraded via hydrolysis with no specific release triggers. The studies in Chapter 3.2 all use passive release. As these IONP systems have no specific triggers, drugs leadked into the blood can accumulate in healthy tissues, causing undesired side effects.

An effort to improve control over drug release has prompted development of stimulus-responsive drug delivery systems. These sophisticated methods include encapsulation of drugs or cleavable linkages that release upon an environmental stimulus, such as pH, temperature, redox potential, ultrasound, electrical fields, or magnetic fields.[87] pH cleavable bonds are the most common, due to the acidic microenvironment of tumor cells. Ester bonds and hydrazone bonds hydrolyze in acidic conditions, while maintaining a strong covalent bond in neutral conditions.[88,89] These factors allowed Kievit et al. to load DOX onto IONPs via a hydrazone bond between the PEG and DOX. This formulation was used to treat rat glioma cells, and demonstrated pH-dependent release in acidic environment while retaining a stable bond in neutral pH. It allowed drug release only in tumor microenvironment while minimizing drug loss in the blood.

Other release mechanisms involve using magnetic fields to influence IONPs in vivo. Hardiniansyah et al. encapsulated IONPs in a thermosensitive liposomal structure loaded with curcumin, a compound known to inhibit proliferation of cancer cells while inducing apoptosis.[90] Via an inductive hyperthermia formed by high-frequency magnetic field, the IONPs heat up the liposomal system, causing the liposome to thermally degrade and release curcumin. This method gives fine control to release therapeutics and ability to monitor the system using MRI.

Several challenges surround potential clinical use of IONP-based theranostic agents: (1) insufficient drug loading caused by poor pharmacokinetics of many therapeutics and insufficient surface area for drug loading, (2) off-target accumulation of IONPs and associated therapeutics causing undesired side-effects, and (3) low signal detection from IONPs under MRI. These challenges can be overcome by developing novel methods in drug loading with precise,

controlled release, active targeting to accumulate only in desired sites, and by engineering IONPs to maximize relaxivity.

4. Design and synthesis of iron oxide nanoparticles

Depending on the intended application of IONPs, many factors need to be considered in NP design and synthesis. IONPs must be an effective MRI contrast agent, maintain biological stability, and be able to bypass biological barriers. The iron oxide core and the polymer surface coating can be tailored to achieve these three aims. Magnetic properties, which determine whether an IONP will be suitable for T_1 or T_2 contrast enhancement, are primarily governed by composition, size, and morphology of the iron oxide core, along with second- and outer-sphere contributions to r_1 from the polymer coating, plus some surface effects from the chemical group binding the polymer to the iron oxide core. The polymer coating and its effects on surface charge, hydrodynamic size, and hydrophobicity largely determine stability and ability to avoid biological barriers. Size and morphology of the iron oxide core are key for any theranostic application, and ability to tailor these properties by altering the method of IONP synthesis is essential. However, current methods are often unreliable and thus far elude description by classical nucleation theory.

4.1 Design parameters for biological applications

IONPs have proven their efficacy as T_2 contrast agents, yet their potential as T_1 contrast agent has yet to be fully explored. Many factors contribute to T_1, including core size, morphology, composition, and polymer coating. These factors and how they contribute to IONP's unique magnetic properties will be discussed. IONPs must also be able to bypass biological barriers to succeed in biological applications. Strict parameters in terms of size and zeta potential must be met for efficacy.

4.1.1 Core size, morphology, and composition

Core size plays an important role in how effective of a contrast agent IONPs can be. As stated previously, IONPs have proven to be effective T_2 contrast agents, but also possess great potential as T_1 contrast agents. IONPs are effective T_2 contrast agents because of their high magnetization, which creates local magnetic field inhomogeneities leading to high transverse relaxivity (r_2). However, core size can be manipulated to make IONPs into suitable T_1 contrast agents. Reducing core size is the most straightforward method in suppressing the magnetic moment of IONPs to reduce r_2 relaxivity. This can be explained by the spin-canting effect: the spins on the surface of the nanoparticles become disordered as the crystal structure is interrupted. Because these surface spins do not fully align with the bulk spins of the nanoparticle, they form a magnetically dead region at the particle surface. As the core size decreases, a greater proportion of the particle's volume is composed of the magnetically dead region (**Figure 4-1)**.[30] When the iron oxide core is 5 nm, roughly half the region is magnetically dead, and this proportion increases to 78% for a 2.5 nm iron oxide core.

The dependence on core size in reducing net magnetization has been well-established in literature.[91-93] In a study by Chen et al., IONPs of varying core sizes (14–26 nm) were developed via thermal decomposition method. After PEGylation, the IONPs were evaluated for their magnetic properties, which showed a clear correlation between core size and magnetization.[94] The saturation magnetization increased with core size, as did r_2 relaxivity value. This trend was also observed in a study by Hyeon et al. using IONPs of core sizes 1.5–12 nm.[95] Magnetization and r_2 both decreased with size, with the 1.5 nm particles exhibiting almost no magnetization. The thickness of the spin-canting layer has been observed to be between 0.4 to 0.9 nm across a range of IONP sizes[96-100], suggesting that ultrasmall IONPs, with almost their entire volume

composed of disordered spins, could reach r_2/r_1 ratio close to 1. However, the high surface energy of ultrasmall IONPs, due to their large surface area/volume ratio, can lead to aggregation, and passivating the surface of these IONPs to confer stability in biological media remains a challenge.

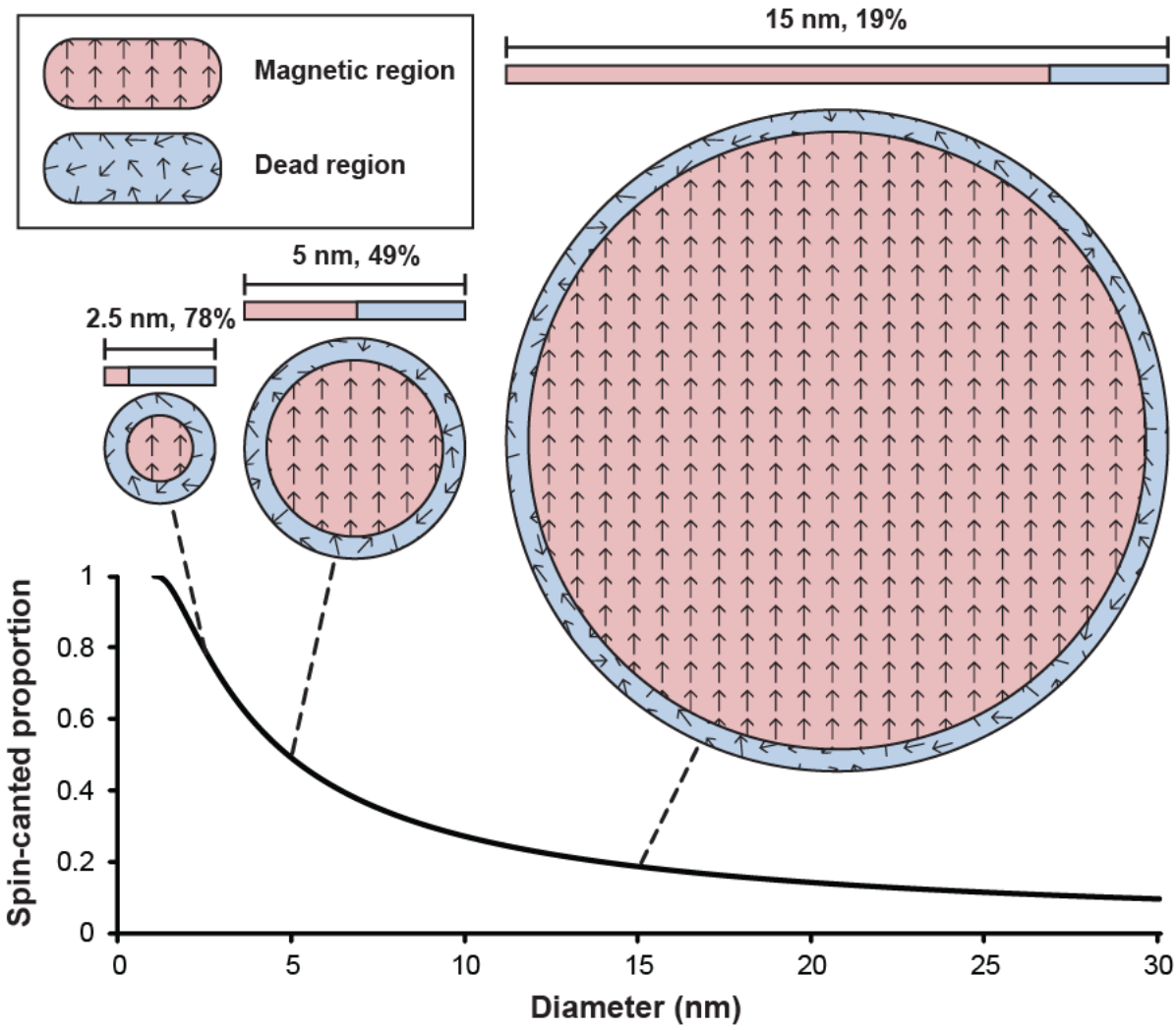

Figure 4-1. The proportion of IONP volume consisting of the magnetically dead spin-canted region as a function of particle size (assuming a 0.5 nm spin-canted layer[96-98,100]), with a depiction of representative IONP core cross-sections. The thickness of this region remains constant regardless of IONP size, therefore, comprises a greater proportion of smaller particles leading to a decrease in magnetization, and thus r_2, with IONP size.

Similarly, morphology can also affect the magnetic properties of IONPs. Spherical IONPs are the most commonly researched, yet changes in core morphology can influence both r_1 and r_2 relaxivity. Morphologies with particularly high surface area to volume ratios may increase r_1 by exposing a greater number of metal ions, which allows for more inner-sphere interactions with water molecules. The shape of the core can also reduce r_2 by increasing the proportion of the spin-canted region for a given volume, but edge effects may increase local magnetic field inhomogeneity. A suitable core morphology must balance these effects to obtain an acceptable r_2/r_1 ratio.

Rod-shaped IONPs are generally less suitable as T_1 contrast agents than spheres. In one study of nanorods of length 30–70 nm and diameter 4–12 nm, r_2 values doubled in comparison to spheres of equivalent volume.[101] This is because the induced magnetic field of a sphere decreases with the inverse cube of the distance from the core, while that of a cylinder decreases with the inverse square, so the nanorod's magnetic field remains stronger at a greater distance from the core. Because it remains relevant over a larger volume, the nanorod's magnetic field will reach a greater number of protons, thus increasing dephasing (and increasing r_2) more efficiently than the spherical IONP.

A spherical core, however, does not always have a T_1 advantage over a rod. Extremely thin iron oxide nanorods can also be appropriate T_1 contrast agents. Nanowhiskers of length 20 nm and an exceptionally small diameter of 2 nm have been shown to have r_1 and r_2/r_1 values (6.13 mM^{-1} s^{-1} and 1.83, respectively) comparable to commercially available GBCAs.[102] The small diameter of the nanowhiskers leads to a high proportion of their volume composed of the magnetically dead spin-canted layer, severely reducing their magnetization. Moreover, the high

surface area to volume ratio provides significant area for water molecules to interact directly with the core, and thus an increased inner sphere contribution to r_1.

More exotic shapes affect r_1 and r_2 in ways that may not be immediately obvious. Yang et al. proposed a framework for understanding these effects in a study of unusually shaped Mn-IONPs.[103] Six Mn-IONP shapes of similar volume were considered: sphere, cube, hexagonal plate, tetrahedron, rhombohedron, and octapod (**Figure 4-2**). A greater effective radius (defined as half the length of the body diagonal of the particle) increased r_2, as did an increase in the number and sharpness of corners. Effective radius gives an approximation of aspect ratio, and a greater aspect ratio, as in the case of the nanorods, increases r_2. Additionally, sharp corners have

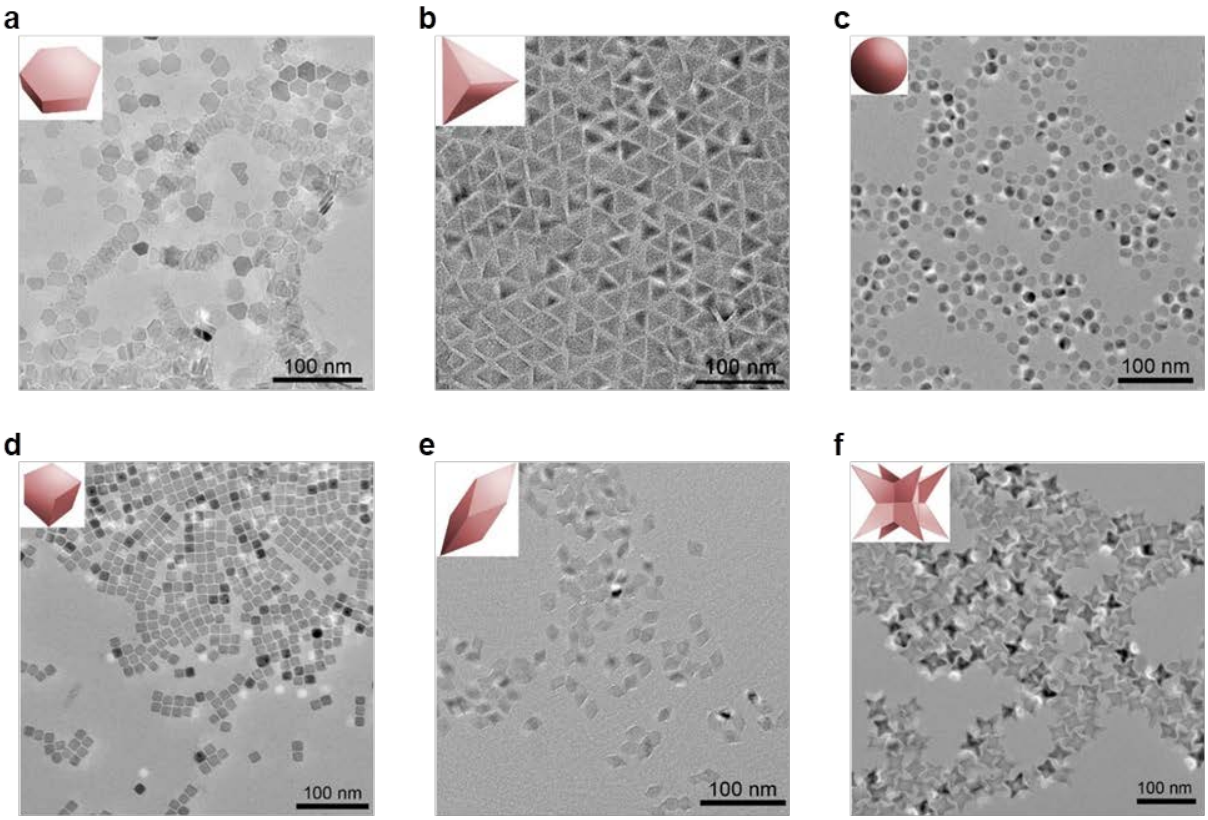

Figure 4-2. TEM images of Mn-IONPs with various morphologies, listed in order of increasing r_2/r_1: (a) hexagonal plate, (b) tetrahedron, (c) sphere, (d) cube, (e) rhombohedron, and (f) octapod. (Reproduced with permission from[103] , Copyright © American Chemical Society 2018.)

a high density of magnetic surface charge, producing stray magnetic fields that promote rapid dephasing.

While the relationship between r_1 and shape was roughly based on the surface area to volume ratio, the clearest correlation was an increase in r_1 with the number of effective metal ions on the exposed faces. The number of exposed metal ions depends on surface area, but also on which facets of the crystal structure are exposed. The (100) facet, for instance, only has 2 effective Fe^{3+} ions, while the (110) facet has 2.83 Fe^{3+} and 2.83 Fe^{2+} (or, in this case, Mn^{2+}). Water molecules interact with these exposed ions, resulting in inner sphere contribution to r_1 relaxivity.

The most important distinction between the six shapes of Mn-IONP is their r_2/r_1 ratio. The octapod, with its eight sharp points, has the highest r_2/r_1 ratio (16.5 at 1.5 T). However, it is not the sphere, but the hexagonal plate with the lowest r_2/r_1 ratio (10 at 1.5 T). It has neither the highest nor the lowest value for either relaxivity, but a balance of minimal edge/corner effects and a high number of effective metal ions at its surface. The six morphologies arranged in order of increasing r_2/r_1 ratio are shown in **Figure 4-2**. Despite the lowest r_2/r_1 ratios of hexagonal plates and tetrahedron, exotic morphologies are often challenging to synthesize and stabilize due to their high surface energy to volume ratios. Also, the lower r_2/r_1 ratios are only modest improvements over the sphere's, and as spheres are widely studied, spheres may be the logical morphology to investigate.

Lastly, IONPs can come in many different compositions, controlled by synthesis method and ratio of reagents. Composition plays a significant role in determining the magnetic properties of the nanoparticles. In most cases, including those synthesized by the popular thermal decomposition method, iron oxide nanoparticles are in the form of Fe_3O_4 (magnetite) and γ-

Fe_2O_3 (maghemite). Bulk magnetite possesses higher saturation magnetization than maghemite, making it more suitable for enhancing T_2 contrast.[104] Additionally, the Fe in magnetite is composed of a ratio of 2 Fe^{3+} ions (each with 5 unpaired d electrons) to 1 Fe^{2+} ion (4 unpaired electrons), whereas the Fe in maghemite is composed entirely of Fe^{3+} ions. As stated previously, the 7 unpaired electrons in Gd^{3+} allow ample interaction with water molecules, making GBCAs an effective T_1 contrast agent.[36] Because it has more unpaired electrons available, maghemite is expected to have slightly higher r1 relaxivity than magnetite. Therefore, maghemite can reduce r_2 by reducing IONP magnetization, without decreasing $r_{1,}$ making it preferable to magnetite for T_1 contrast.

Park et al. report the dependence on core size in the amount of magnetite and maghemite present in IONPs synthesized from thermal decomposition.[7] Via XAS and XMCD results, the amount of maghemite was found to increase with smaller core sizes, with maghemite being the dominant phase with 5 nm IONPs. As the core size decreases, the ratio of surface area to volume increases, increasing the proportion of oxidized maghemite at the IONP surface.

The magnetic properties of magnetite and maghemite nanoparticles have been investigated by many groups. However, it is important to note the challenge in distinguishing magnetite from maghemite. XRD patterns of both structures are very similar, with distinguishing peaks often marred by noise. In a study by Kucheryavy et al., IONPs composed of either magnetite or maghemite with core diameter of 4.8 nm were evaluated for their magnetization.[93] Magnetite vs. maghemite was confirmed via redox titration as an alternative to XRD. The IONP composed of maghemite possessed lower net magnetization than the IONP composed of magnetite, making it the preferred composition to reduce r_2 relaxivity.

In another study by Hyeon et al., 3 nm IONPs were synthesized via thermal decomposition.[95] XRD patterns revealed maghemite to be the primary crystal structure, and these IONPs were able to achieve an r_2/r_1 ratio of 6.12 using a 3 T MRI. This idea has been further explored by Wei et al. using IONPs synthesized via thermal decomposition, which were fully oxidized using trimethylamine N-oxide to convert all magnetite into maghemite.[49] After coating with zwitterions, an r_2/r_1 ratio of 2.0 was achieved at 1.5 T. Given its advantageous effects on both r_1 and r_2, oxidation does not need to be avoided, but rather encouraged for IONPs designed for T_1 contrast.

Doping has been a commonly used technique to develop dual-mode T_1-T_2 contrast agents using IONPs. Such systems often use Gd to enhance T_1 while retaining the T_2 properties of IONPs. However, in most situations, dual-mode T_1-T_2 contrast agents are less effective than T_1 or T_2 contrast agents individually. Additionally, this does not address the issue of Gd toxicity. Similarly, Park et al. doped IONPs with europium.[105] Eu^{2+} possesses 7 valence electrons, the same number as Gd^{3+}, resulting in high relaxivity. Despite the claims of nontoxicity of Eu^{2+}, Eu^{2+} is wildly reactive and readily oxidizes to Eu^{3+}, which possess low relaxivity and severe toxicity.[106]

However, the idea of doping could prove to be useful if IONPs were doped with materials that can interrupt the crystal structure of IONPs to increase spin-canting. Instead of producing a dual-mode T_1-T_2 contrast agent, doping IONPs with materials that diminish overall magnetization could be an effective strategy to reduce r_2/r_1 and make a more suitable T_1 contrast agent. For example, Peng et al. developed FeOOH nanoparticles that are antiferromagnetic possessing low r_2, resulting in a low r_2/r_1 ratio.[107] However, challenges in monodispersity and homogeneity limit FeOOH nanoparticles from being effective on their own. An

antiferromagnetic material like FeOOH doped into maghemite could potentially suppress r_2 enough to produce an effective T_1 contrast agent. In considering such a strategy, the benefits to r_2/r_1 must be weighed against the possibility of increased toxicity and the increased cost of a more complex synthesis if the goal for such IONPs is widespread clinical utility.

4.1.2 Surface coating

Surface coatings of IONP systems can be tailored to improve T_1 contrast, primarily by affecting the time parameters that contribute to r_1. These are τ_{1e} (electron relaxation time), τ_R (rotational correlation time), and τ_m (water residence time). Each of these affects r_1 relaxation by altering the efficiency of energy exchange between the IONP system and the hydrogen protons of bulk water, but different parameters will dominate depending on conditions. τ_{1e} increases with the square of the magnetic field strength, so it is only short enough to be relevant in weak fields, and has no significant impact on r_1 at clinical field strengths of 1.5 T or more.[108] The dominant parameters affecting relaxivity, τ_R and τ_m, can be visualized in **Figure 2-4**.

The rotational correlation time (τ_R) is the time for the IONP system to rotate one radian. The magnetic field fluctuations produced by this rotation induce relaxation most efficiently near the proton Larmor frequency (42.58 MHz/T), at which maximum energy exchange occurs. Traditional gadolinium chelate contrast agents, for instance, tumble quickly because of their small size, but their rotation can be slowed, and r_1 increased, with the addition of ligands that bind to human serum albumin or other large proteins in vivo. For large, flexible systems, it should be noted that τ_R comprises both the IONP system's rotation and the motion of the metal or metal oxide core in relation to the system as a whole. It has been shown in GBCAs that r_1 can be increased if this relative motion is inhibited by using coatings with rigid ring structures or secondary bonds.[109]

The final time parameter is water residence time, which is divided into τ_m, the amount of time a water molecule is in direct contact with the iron ions in the core (typically 0.1 ns to tens of μs), and τ'_m, the residence time in the secondary or outer sphere (generally a few ps).[108] Increasing either of these time parameters will generally increase r_1, because they are usually shorter than the time it takes water molecules to relax. This, of course, depends on the value of τ_R: as τ_R increases to near the Larmor frequency, relaxation happens more efficiently, and a shorter τ_m may be preferred so that relaxed water molecules return to the bulk water more quickly.[110] For instance, typical values of τ_m to maximize r_1 are between 10–30 ns for GBCAs, but may be less than 10 ns for those systems with longer τ_R.[108] There is no universal ideal value for τ_m or τ'_m; they must be optimized for the specific circumstances of the IONP system, such as τ_R, magnetic field strength, and the magnetic moment of the core.

The time parameters τ_R, τ_m, and τ'_m, as well as associated r_2 values, are influenced by the chemical and physical properties of the coating of the iron oxide core. Unfortunately, these parameters are not independent of each other, nor are the physical and chemical properties of the coating. A clearer understanding of the effects of surface coatings can provide guidance in improving IONP contrast agent design.

4.1.2.1 Molecular weight

Altering the molecular weight (MW) or chain length of the polymer coating would seem to be the most straightforward method to tailor r_1, however, the reality is not so simple. The tumbling time, τ_R, depends on the mass of the complex, but also on factors such as the viscosity of the solvent, the density of the system, and the hydration radius of the coated IONP.[111] Additionally, the hydrated volume of the IONP complex will affect the number of water molecules interacting with it, and the density of the polymer coating will alter τ_m or τ'_m as the

diffusivity within this hydrated layer changes. All of these interrelated factors play a role in determining r_1.

Studies of the effect of molecular weight of the coating polymer on relaxivity found little direct correlation between them. In one such study, Khandhar et al. coated IONPs synthesized via thermal decomposition with PEGs with MW ranging from 1–20 kDa.[91] In all their samples the hydrodynamic size increased linearly with increase in chain length, as expected. However, they found no correlation between chain length and r_2, r_1, or r_2/r_1. No noticeable trends were observed, likely because the chain length of the PEG impacts the coating density: higher MW PEG has more steric hindrance than lower MW PEG. Coating density also changes hydrophilicity, which impacts the diffusivity of water molecules through the system.

In a similar study conducted by LaConte et al., IONPs were coated with PEG with MW ranging from 550–5000 Da.[112] In this study, there was no linear correlation between PEG chain length and hydrodynamic size. IONPs coated with PEG550 had a hydrodynamic size larger than those coated with PEG1000. This is likely because such low MW PEGs are not able to stabilize IONPs. Similar to the Khandhar study, no firm correlation was established between relaxivity values and chain length. Some distinction could be made between larger MW PEGs (1000, 2000, 3000 Da) and smaller PEGs (550, 750 Da), with the former having higher r_1 and lower r_2 values. This could be attributed to the increase of hydrodynamic volume with chain length, resulting in a greater number of water molecules exchanging energy with the nanoparticle complex. It may also be the effect of the greater mass of the IONP system on τ_R. Similar experiments have been performed by many other groups, with similarly inconclusive correlations.[92,113,114]

Monte Carlo simulations by LaConte et al. may shed some light on the mechanisms behind these seemingly inconsistent results.[112] They used a model consisting of three layers: an

IONP core, an inner layer that excludes water from direct interaction with the core, and an outer layer treated as either bulk water or an area of slower diffusion. This model allowed for investigation of second- and outer-sphere effects independent of any inner-sphere contribution to relaxivity. When the outer layer was treated as an area of fast diffusion, like bulk water, increasing its thickness was effective at increasing r_1. However, when treated more realistically as an area of slower diffusion, a thicker outer layer also caused an increase in r_2. Water molecules diffusing more slowly through the IONP coating were relaxed more completely as they had more time to interact with the complex (increasing r_1), but they also remained in proximity to the core's magnetic field for longer (increasing r_2) (**Figure 4-3**). While this IONP model is fairly unique, the balancing act of promoting water molecule interaction with the complex but avoiding the influence of the magnetic field, is a fundamental difficulty for designing any IONP system suitable for T_1 contrast.

In addition to the challenge in minimizing r_2/r_1, there are practical challenges in maximizing r_1. Increasing the molecular weight of the polymer coating does not reliably increase r_1. There are many interrelated factors influencing longitudinal relaxation, and the way they affect water diffusion through the IONP system is not always controllable or well understood. Clearly a simple consideration of polymer chain length is not enough; polymer packing will change water mobility in the IONP system, and its effect undermines any clear relationship between r_1 and molecular weight. Polymer chain length, ligand density, hydrophilicity, and other chemical properties of the polymer coating are all proxies for the time parameters that cannot be directly altered: τ_R, τ_m, and τ'_m

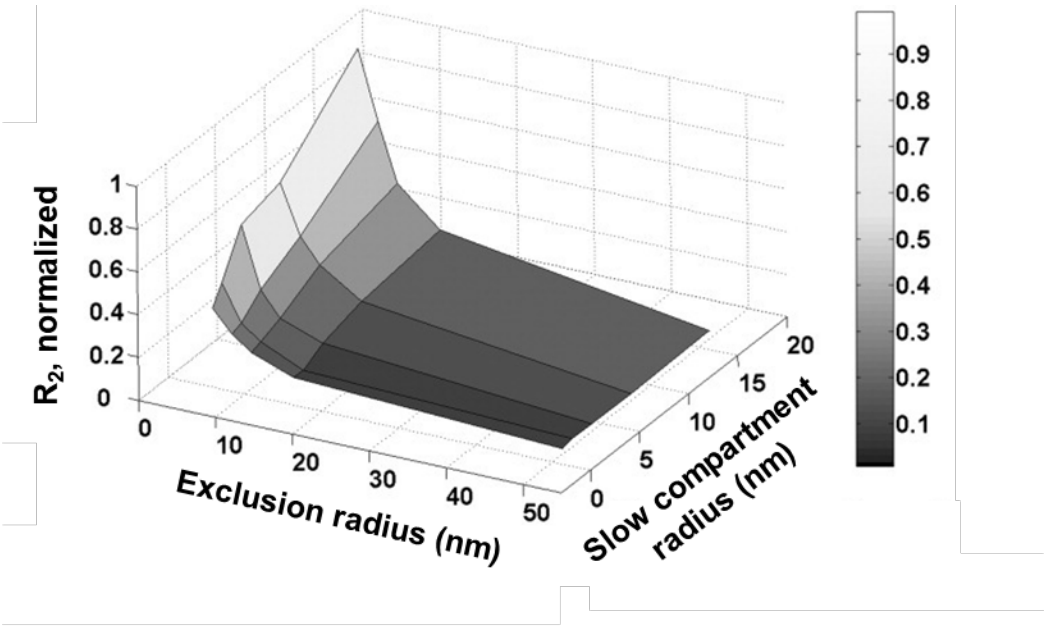

Figure 4-3. Modeling and computer simulation of IONP relaxivity. R_2 (normalized r_2) is plotted as a function of both exclusion radius (hydrophobic region around the core that excludes water molecules from direction interaction) and slow compartment radius (region where water molecule diffusion is slowed by the polymer coating), with high values of R_2 represented by lighter shading. Note that a larger slow compartment radius can increase r_1 but it also increases r_2 as water molecules reside longer at the strongest region of the core's magnetic field. (Reproduced with permission from[112], Copyright © Wiley-Liss, Inc. 2007.)

While it is not possible to directly alter these parameters individually, it is possible to measure them, at least approximately. τ_R can be estimated using several techniques, including NMR and EPR spectroscopy, and fluorometry, and τ_m can be determined by ^{17}O NMR at high field strength.[109,115] Measuring these parameters in addition to r_1 and r_2 may improve our understanding of how IONP-based systems can be designed to maximize r_1.

4.1.2.2 Chemical composition of surface coating: anchoring groups

Altering the anchoring groups that bind the ligand to the IONP core may be a promising approach to reducing r_2. Anchoring groups are thought to alter IONP magnetization by changing

the oxidation and spin-canting of the IONP surface. Determining the exact mechanism of this effect is challenging, however, several studies provide a framework for rational selection of anchoring groups.

In one study, Zeng et al. conjugated PEG 2000 to Fe_3O_4 NPs using three different groups: diphosphate, hydroxamate, and catechol.[116] All three reduced the magnetization of the IONP, with diphosphate causing the most significant decrease, followed by catechol, then hydroxamate. This is tentatively suggested to be the result of decreasing binding affinity, but how this reduces the magnetization is not entirely clear. Smolensky et al. performed a similar experiment, coating IONPs with PEG using four anchoring groups: dopamide, 2,3-dihydroxybenzamide (DHB), carboxylate, and phosphonate.[117] Both dopamide and DHB largely maintained the magnetization of the IONP, while phosphonate and carboxylate groups were able to reduce the magnetization. In other studies, citric acid and meso-2,3-dimercaptosuccinic acid (DMSA) have been found to reduce IONP magnetization compared to oleic acid.[118] 3-aminopropyltriethoxysilane (APTS) reduces IONP magnetization by 50% compared to no coating at all.[119]

The mechanism by which anchoring groups alter magnetization is not entirely clear, but direct analysis of the degree of spin-canting may provide guidance in optimizing r_2 values for IONPs designed as T_1 contrast agents by isolating the effect of the anchoring group from other factors affecting magnetization and r_2. The thickness of the spin-canting layer can be determined using ^{57}Fe Mössbauer spectrometry, and NMR.[98] When the spin-canting layer is present, it is typically found to be about 0.5 nm, corresponding to two atomic layers with broken symmetry, across various particle sizes.[96-98,100]

Several studies have taken advantage of spin-canting analysis of IONPs with various anchoring groups in an effort to improve T_2 contrast by minimizing spin-canting. Daou et al.

found that carboxylate groups decreased the magnetization of IONPs, but phosphonate did not.[97] Both anchoring groups created an oxidized layer of about 2.8 nm, but only the IONP coated with carboxylates exhibited a spin-canting layer of 0.5 nm. They speculated that phosphonate groups replace missing oxygen atoms at the IONP surface, thus reducing spin-disorder by bolstering the crystal structure at the edges of the IONP where it has been interrupted. Costo et al. found that carboxylate and phosphonate both increased magnetization by lessening the degree of spin-canting, but, consistent with Daou, found that phosphonate decreased spin-canting more than carboxylate.[97,120] They suggest that this is due to phosphonate's double-monodentate or bidentate bonds increasing IONP surface order compared to carboxylate's single bond.[120] Similarly, Nagesha et al. reported that dopamine coating increases magnetization over oleic acid coating, confirming a smaller magnetic radius for the oleic acid-coated IONP despite TEM showing a comparable core size for both coatings.[121] It is possible that the catechol group from dopamine acts analogously to phosphonate in this situation, filling in the crystal structure of iron oxide at its surface and promoting higher magnetization. Anchoring groups that maintain or increase spin-canting at the IONP surface could be applied to reduce magnetization, and therefore r_2, and would be advantageous in the development of T_1 contrast agents. There are relatively few studies investigating the effects on magnetization of only anchoring groups, as opposed to the whole polymer coating, but key findings with pertinent chemical structures are summarized in **Table 4-1**.

In addition to the effects of anchoring groups on oxidation and spin-canting, there is evidence that π-electrons in the anchoring group may increase r_2 by creating a small magnetic field in opposition to the induced magnetic field of the whole IONP core, and this additional magnetic field homogeneity may increase the rate of dephasing. Zeng et al. found that the r_2/r_1

Table 4-1. Chemical structure of various anchoring groups and their effects on magnetization.

Anchoring group	Structure	Notes	Reference
Diphosphate	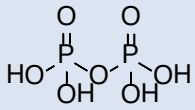	In order of most significant magnetization decrease: Diphosphate > Catechol > Hydroxamate	116
Catechol	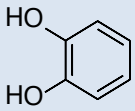		
Hydroxamate	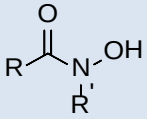		
Carboxylate	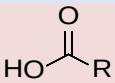	Phosphonate and carboxylate groups reduced IONP magnetization Dopamide and DHB had little effect on magnetization	117
Phosphonate	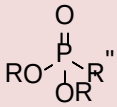		
Dopamide	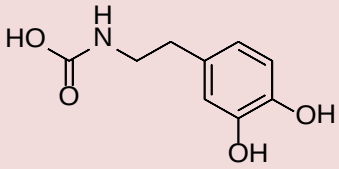		
2,3-dihydroxybenzamide (DHB)	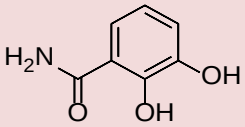		
Citric acid	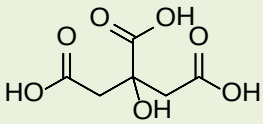	Both citric acid and DMSA reduced IONP magnetization compared to oleic acid	118
meso-2,3-dimercaptosuccinic acid (DMSA)	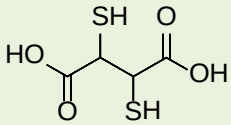		
Oleic acid	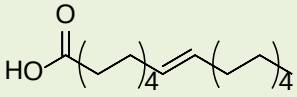		
3-aminopropyltriethoxysilane (APTS)	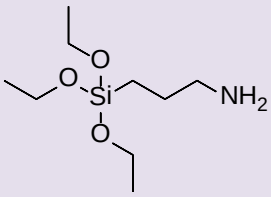	Reduced IONP magnetization by 50% compared to no coating	119

ratio of the IONP system was greatest with the π-π conjugation of a catechol group, lower for the p-π conjugation of a hydroxamate group, and lowest for the non-conjugation of diphosphate.[116] The r_2/r_1 ratio is an imperfect way to measure this effect, but it does suggest that avoiding π-π interaction could improve an IONP system's suitability as a T_1 contrast agent.

4.1.2.3 Chemical composition of surface coating: terminal groups

While there are many coatings used for IONPs in the literature, there is little data isolating the effects of their chemical properties on longitudinal relaxivity, independent of the effects of their anchoring group or their molecular weight. Altering the composition of the outer sphere, however, could prove to be a valuable approach to tailoring τ_m and τ'_m, especially τ'_m in IONP systems that are designed to minimize r_2 by excluding water from the volume nearest the core.

In a study of GBCAs, Dumas et al. measured the effect of various donor groups on τ_m.[115] Inner sphere water residence time ranged from 0.7 to 612 ns with donor groups, ordered from fastest to slowest τ_m: phosphonate ~ phenolate < alpha-substituted acetate < hydroxamate ~ sulfonamide < amide ~ pyridyl ~ imidazole. Maximizing r_1 was not as simple as minimizing or maximizing τ_m. Amide, pyridyl, and imidazole groups had residence times too long to exchange efficiently with bulk water, while the short residence times of phosphonate and phenolate meant that the exchange was too fast for efficient relaxation. Measuring τ_m directly, however, helped determine which donor group was suitable for the specific GBCAs. In IONP systems, the addition of appropriate groups in the outer sphere could help slow τ'_m to increase its contribution to r_1.

Core size, morphology, composition, and polymer coating are all factors that affect magnetic properties. Depending on the intended application of the IONP, these factors can be altered to suit their particular application.

4.1.3 Hydrodynamic size

Nanoparticle size is an important property of theranostic agents, as it can impact uptake, deposition, and clearance. Size also plays an important role when bypassing biological barriers. Hydrodynamic size is defined as the hypothetical size of a colloid as it behaves in a fluid, taking into consideration the water layer surrounding the colloid. Hydrodynamic size is measured using dynamic light scattering (DLS), which provides size and also its polydispersity index, is an effective measure of the dispersity of the system.

When designing therapeutic agents to bypass biological barriers, there are specific hydrodynamic size restrictions. For example, IONPs that are smaller than 10 nm are likely to be cleared by the kidneys. This could be used as an advantage; if the goal is to target the kidneys to treat renal disease, designing the IONP system to be smaller than 10 nm can be incredibly effective.[122] However, if the intended target is elsewhere in the body, NPs must be greater than 10 nm in order to prevent renal clearance. There also exists an upper limit in hydrodynamic size, as IONPs greater than 100 nm are prone to be cleared through the liver, spleen, or the mononuclear phagocyte system (MPS).[123,124] IONPs greater than 100 nm can also no longer benefit from the EPR effect, and are not able to bypass the blood-brain barrier (BBB).

Due to the many biological barriers that IONPs must overcome, hydrodynamic size is an important property that must be characterized and reported. The ideal size range for IONP-based

theranostic agents falls between 10–100 nm for most biological applications to prevent clearance, maximizing therapeutic efficacy.

4.1.4 Zeta potential

Zeta potential is another important property when designing theranostic agents. Like hydrodynamic size, zeta potential is measured using DLS, which measures the electrokinetic potential in colloidal systems. In the case of IONPs dispersed in water, zeta potential is the potential difference between bulk water and the outer layer of water surrounding the IONP. Zeta potential directly impacts both the short-term and long-term stability of IONPs and indicates the tendency of IONPs to aggregate.[125] Crucially, zeta potential also influences how IONPs can interact with biological systems. For example, IONPs with a strong negative surface charge can be rapidly opsonized and cleared by macrophages. Similarly, strong positive charge on the surface of IONPs can electrostatically interact with the negatively charged cell membranes or extracellular matrices, leading to nonspecific uptake.[126] Therefore, IONPs should be near neutral or with slight negative charge for most theranostic applications. As zeta potential has a direct impact on how IONPs interact with various biological barriers, zeta potential is an important property that must be measured.

4.2 Synthesis of nanoparticles

Over the past two decades, various methods in synthesizing IONPs have been developed. Although many report reliable synthesis methods, there is a lack of studies delving into the principles of nucleation and growth. This is the case for most nanomaterials, and the "chemical synthesis of metal nanocrystals remain an art rather than a science."[127] As magnetic properties are largely dependent on the core's size, morphology, and composition, having precise control

over the synthetic process is important, which requires better understanding of how the principles governing nucleation and growth apply in IONP synthesis.

4.2.1 Thermal decomposition

Thermal decomposition has been the method of choice to synthesize uniform nanocrystals, including IONPs, originally developed by Park et al.[7] This method involves gradual heating of an iron oleate complex in a high-temperature solvent, and holding at the reflux temperature to age the NPs for growth. Park's method has been the industry standard in IONP development and the method has been used to commercialize IONPs. This is due to the precise control over uniformity in shape and size that can be achieved (**Figure 4-3**). Additionally, this method can be scaled up for large-scale productions. Despite this success, the kinetics of this procedure is poorly understood, and, as will be discussed in 4.2.4, fits poorly with the classical theory of nucleation and growth.

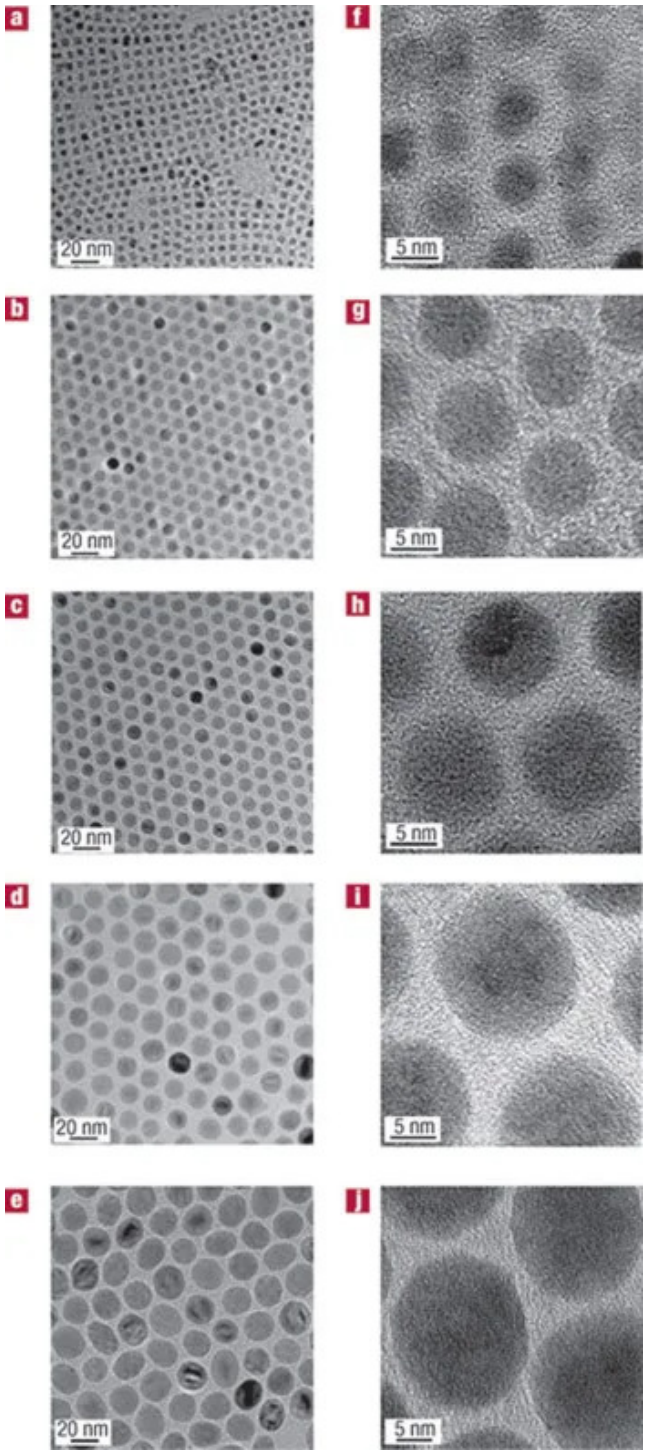

Figure 4-4. (**a**, **f**) 5 nm; (**b**, **g**) 9 nm; (**c**, **h**) 12 nm; (**d**, **i**) 16 nm; and (**e**, **j**) 22 nm nanocrystals. TEM images showed the highly monodisperse particle size distributions and HRTEM images revealed the highly crystalline nature of the nanocrystals. (Reproduced with permission from[7] , Copyright © Springer Nature 2004.)

4.2.2 Co-precipitation method

The co-precipitation method is perhaps the simplest: IONPs are synthesized via co-precipitation of Fe^{2+} and Fe^{3+} iron ions in a basic solution. While the thermal decomposition method produces hydrophobic IONPs that require ligand exchange with a water soluble polymer to make them water soluble, the co-precipitation method occurs in an aqueous solution, and produces water soluble IONPs. Additionally, the thermal decomposition method is time-extensive, while the co-precipitation method can be done in hours. However, there are challenges in producing uniform IONPs (**Figure 4-4**) via the co-precipitation method, and scaling up has yet to be demonstrated.

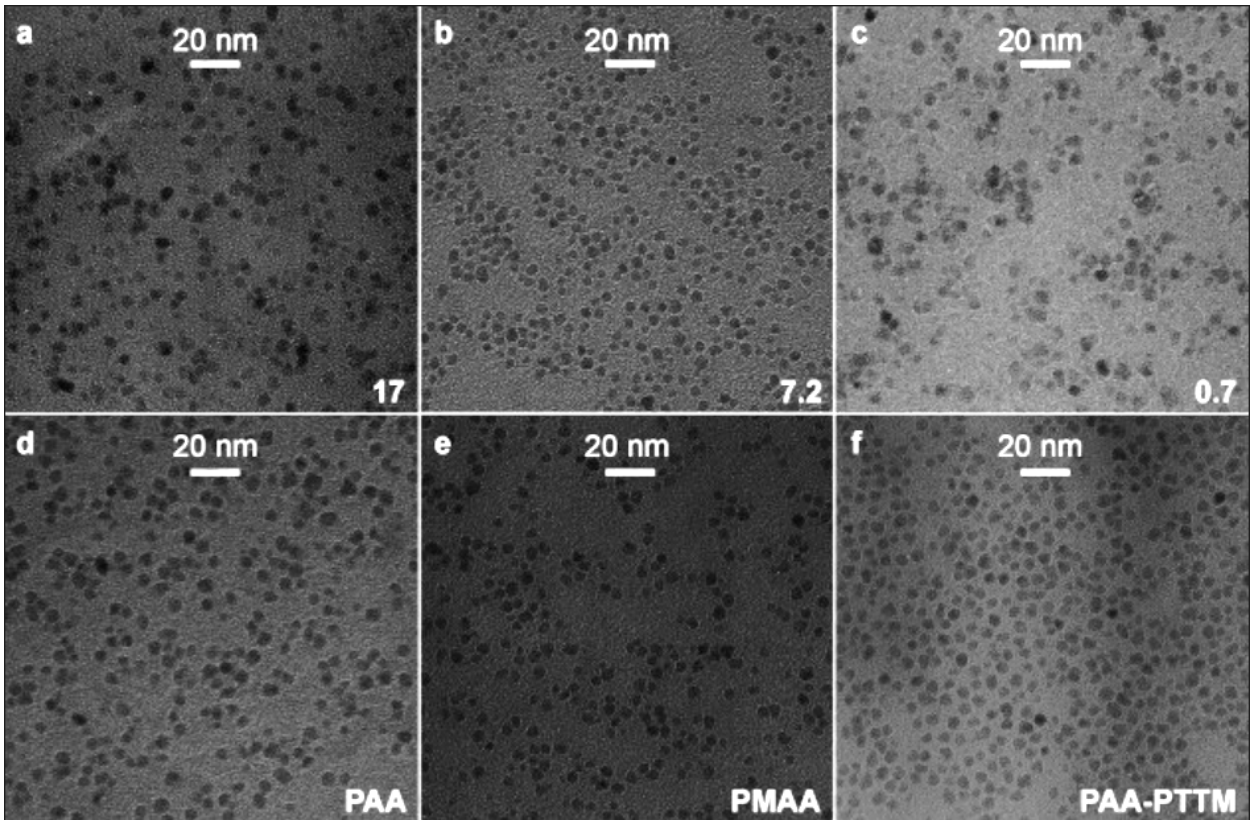

Figure 4-5. TEM images of IONPs produced through the co-precipitation method with various ratios of iron:polymer (a-c) and with different polymers (d-f). IONPs produced through the co-precipitation method show less uniformity than IONPs produced through the thermal decomposition method. (Reproduced with permission from[128], Copyright © John Wiley and Sons 2008.)

4.2.3 Hot injection method

The hot injection method is often used in the semiconductor industry to synthesize transition metal oxides.[129,130] The hot injection method utilizes induction of supersaturation via injecting reagents into a solution of hot surfactants. This method produces a quick nucleation step, followed by growth by diffusion. This method is not very common for IONP synthesis as the method is more labor intensive compared to the co-precipitation method, and produces nonuniform IONPs (**Figure 4-5**).

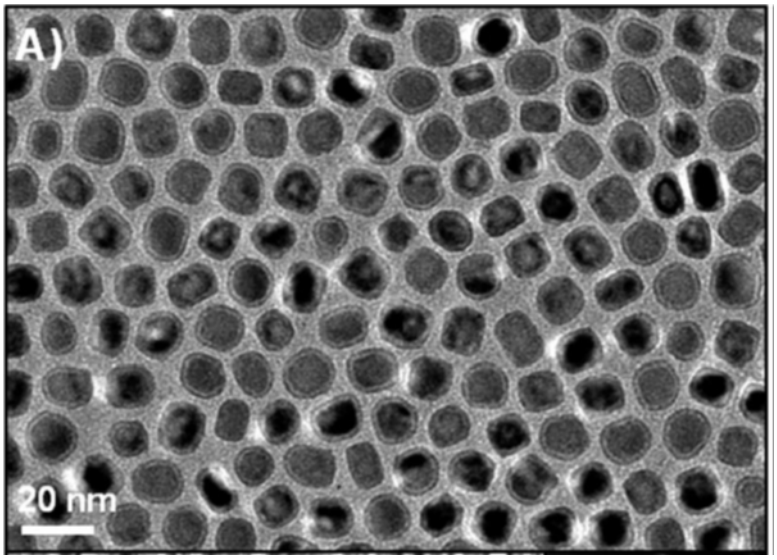

Figure 4-6. Iron core/iron oxide shell NPs produced using the hot injection method. Although these exhibit better size distribution, the morphology is not as uniform. (Reproduced with permission from,[131] Copyright © The Royal Society of Chemistry (RSC) 2011.)

4.2.4 Classical nucleation theory

Classical nucleation theory describes the process of nucleation using Gibbs free energy. The model assumes a particle of radius r, and the Gibbs free energy is composed of two opposing factors, given as,

$$\Delta G = -\frac{4}{3}\pi r^3 |\Delta G_v| + 4\pi^2 \gamma \quad (1)$$

where ΔG_v is the difference in Gibbs bulk free energy per unit volume between the cluster and the surrounding solution, and γ is the surface energy per unit area.[132] The opposing two factors are composed of the negative term that represents bond making, and the positive term that represents the surface energy. The Gibbs free energy reach its maxima at critical radius r_c. When the radius is smaller than the critical radius, to minimize Gibbs free energy, the cluster will tend to dissipate.[133] When the radius is larger than this radius, continued growth of the cluster becomes energetically favorable.[133]

LaMer et al. were the first to explain nanoparticle synthesis using classical nucleation theory. As the concentration of available monomers increases, there exists a critical level of supersaturation, C_s, where nucleation becomes possible. As the saturation continues to increase, it hits C_{min} where the activation energy required to form a stable cluster is easily achieved and nucleation occurs. As nucleation uses up the available monomers, saturation decreases below the rapid nucleation level and growth begins.[134,135] The classical nucleation theory and LaMer's model are illustrated in **Figure 4-6**.

The classical nucleation theory and LaMer's model in describing nanoparticle synthesis have many limitations, and the reality strays further from the model as any bit of homogeneity is lost within the process. Modeling growth has proven to be even more complex than modeling nucleation. Reiss developed a model of growth in which growth is dependent on the flux of monomers available for nanoparticles to grow.[136] This model also assumes ideal situations where homogeneity is maintained, and fails to take into consideration many other possible pathways for growth including aggregation, Ostwald ripening, and coalescence.

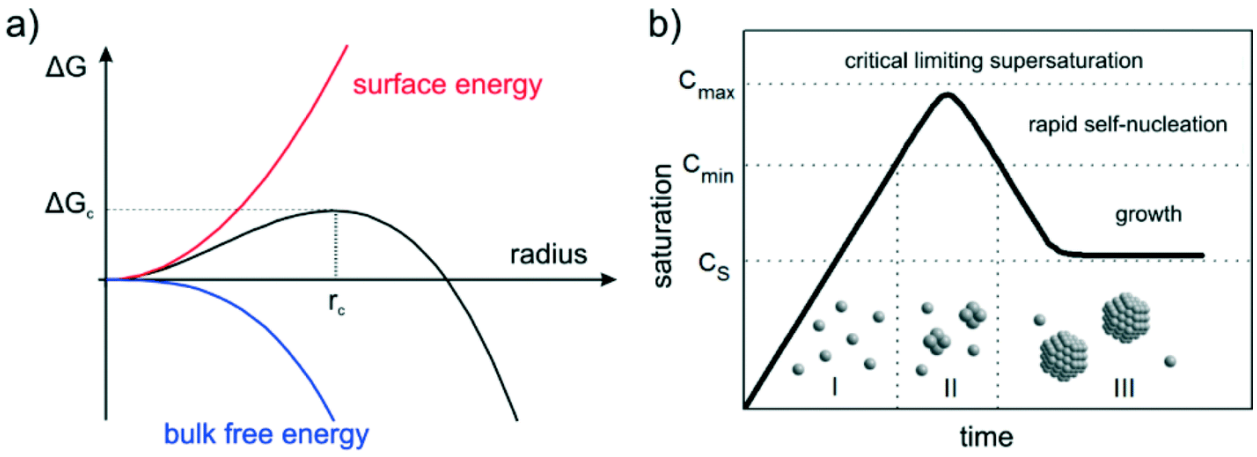

Figure 4-7. Diagrams illustrating classical nucleation theory (a) Dependence on Gibbs free energy on radius, showing the critical radius necessary growth. (b) LaMer model of saturation (monomer concentration) as a function of time, showing regions of nucleation and growth. (Reproduced with permission from[133] , Copyright © The Royal Society of Chemistry (RSC) 2015.)

Although many other theoretical models have been developed taking consideration of other pathways, there are still a large number of factors that hinder reproducible nanoparticle synthesis. These theoretical models fail to have in situ data to prove their models, and fail to take into consideration many other factors including the kinetics of the chemical reaction supplying the monomers, concentrations of reagents involved, temperature, surfactants, and even something as simple as stir rate or heating rate.

5. Cocaine analogue conjugated magnetic nanoparticles for labeling and imaging dopaminergic neurons

Neurological disorders including Parkinson's disease, Alzheimer's, and drug addiction are associated with impaired dopamine regulation. Imaging the dopamine transporter (DAT) has shown promise as a diagnostic modality for early detection of Parkinson's disease (PD). Clinically, positron emission tomography (PET) and single photon emission computed tomography (SPECT) dominate neuroimaging, yet their poor spatiotemporal resolution has frequently led to false positive or inconclusive diagnoses. The superior spatial resolution of magnetic resonance imaging (MRI), in combination with DAT targeted contrast agents, could offer a more detailed spatiotemporal view of DAT-expressing neurons and facilitate earlier detection of PD. Here we present an iron oxide-based nanoparticle (NP) that specifically targets dopaminergic neurons and provides contrast enhancement for MRI. The NP is composed of an iron oxide core and a polyethylene glycol (PEG) coating to which a dopaminergic neurolabeler, DN, is conjugated to form NP-DN. It displayed long-term stability with favorable hydrodynamic size and surface charge for in vivo application. In vitro studies showed NP-DN was non-toxic, displayed specificity towards DAT-expressing neurons, and demonstrated a 3-fold increase in DAT labeling over non-targeted NP. Our study shows NP-DN provided excellent contrast enhancement in MRI, demonstrating great potential for neuroimaging.

5.1 Introduction

Irregular dopamine regulation is largely related to neurological disorders including Parkinson's disease (PD), schizophrenia, attention deficit hyperactivity disorder (ADHD), drug addiction, depression, and anxiety.[137-139] The dopamine transporter (DAT) is a symporter responsible for regulating presynaptic dopamine transmission by removing extracellular

dopamine released from neurotransmission and redistributing it to nearby neurons.[140] Imaging the dopamine transporter has shown promise as a diagnostic modality for PD and other neurodegenerative diseases, but existing imaging methods have many limitations.[138]

Positron emission tomography (PET) and single photon emission computed tomography (SPECT) currently dominate clinical neuroimaging. These modalities in combination with radiolabeled cocaine analogues have been used to map the distribution of various transporters in the brain.[141,142] (^{123}I)-ioflupane and (^{123}I)-FP-CIT radiotracers, composed of ^{123}I bound to cocaine analogues with high binding affinity for DAT, are commonly used to diagnose Parkinson's disease.[138,143,144] In clinical studies, DAT imaging by PET and SPECT has shown promising utility in early detection of PD and distinguishing PD from other non-degenerative parkinsonian disorders by detecting the deficiency of presynaptic dopamine.[138,145-149] However, PET and SPECT provide poor spatiotemporal resolution[2] — which has led to false positive and inconclusive diagnoses of PD.[145,147,150-152] The radiotracers used are toxic, require complex syntheses that can only be performed in specialized facilities and, due to their short half-lives, the synthesis is typically done on-site immediately prior to imaging.[3-6] The inherent limitations of PET/SPECT and the scarcity of radiotracer-based imaging facilities have hindered the progression of neuroimaging in clinical and research settings, highlighting the need for new imaging modalities.

The application of magnetic resonance imaging (MRI) to dopaminergic neuron imaging would provide a new approach capable of overcoming many limitations associated with PET/SPECT. MRI is a ubiquitous, noninvasive technique, and can provide superior spatial resolution to improve the accuracy of PD diagnosis and offer another tool to investigate dopamine regulation. MRI contrast agents, especially superparamagnetic iron oxide

nanoparticles (SPIONs), are less toxic and more stable than radiotracers, which allows greater possible imaging time and avoids the need for on-site synthesis. The intrinsic magnetic properties of SPIONs, combined with their excellent biocompatibility, biodegradability, and surface chemistry that allows the addition of targeting ligands, provides means to image DAT expressing neurons via MRI in vitro and in vivo.[12,13,24]

Here we report the development of an iron oxide nanoparticle capable of labeling live dopaminergic neurons and providing contrast for MRI. The nanoparticle consists of a superparamagnetic iron oxide core coated with poly(ethylene) glycol (PEG), and subsequently labeled with dopaminergic neurolabeler (DN, NP-DN), and Cy5 fluorophore (NP-DN-Cy5). We characterized the morphology, size distribution, zeta potential, and stability of these nanoparticles by transmission electron microscopy (TEM) and dynamic light scattering (DLS). We used UV-vis spectroscopy to quantify Cy5 and DN on the nanoparticles. The targeting efficacy was assessed using flow cytometry, and the labeling was monitored using confocal fluorescence microscopy. Targeting specificity of NP-DN was evaluated in human DAT expressing cell line, EM4-hDAT (positive control, DAT^+), and null-transfected EM4 cells (negative control, DAT^-). The viability of the two cell lines after treatment was evaluated using the Alamar Blue assay.

5.2 Experimental

5.2.1 Materials

All chemicals were purchased from Sigma-Aldrich (St. Louis, MO, USA) unless otherwise specified. We purchased 3-(triethoxysilyl)propyl succinic anhydride (SATES) from Gelest (Arlington, VA, USA); 2000 MW mono-amine functionalized poly(ethylene) glycol

($mPEG_{2K}$-NH_2) from Laysan Bio (Arab, AL, USA); Cyanine5 NHS from Lumiprobe (Hallandale Beach, FL, USA); NHS-PEG_{12}-maleimide and succinimidyl 3-(2-pyridyldithio)propionate (SPDP) from Pierce Biotechnology (Rockford, IL, USA).

5.2.2 Modification of DN

DN-NH_2 was first synthesized following published methods.[153] DN-NH_2 (1 mg) was thiolated via SPDP activation and reduction via TCEP. We reacted 1 mg of DN-NH_2 with 0.98 mg of succinimidyl 3-(2-pyridyldithio)propionate (SPDP) in 100 μL DMSO with 2% N,N-diisopropylethylamine (DIPEA). The solution was reacted for 48 hours at room temperature. We then reduced the SPDP-activated DN by reaction with an excess of tris(2-carboxyethyl) phosphine hydrochloride (TCEP) (4 mg TCEP in 100 μL thiolation buffer, pH = 8.5) for 30 min.

5.2.3 NP synthesis and conjugation of Cy5 and DN

Following the reported procedures, we synthesized 8 nm oleic acid coated iron oxide and coated with PEG[23,154]. Cy5 was conjugated directly onto the NPs, while DN was conjugated via a heterobifunctional PEG crosslinker. To form NP-Cy5, 2 mg of NP was reacted with Cy5 NHS ester (0.1 mg in 10 μL DMSO) in 1 mL 0.1 M $NaHCO_3$ buffer (pH 8.5). The solution was reacted for 1 hour at room temperature, and excess Cy5 was removed via S-200 sephacryl resin equilibrated with deionized water. Then, 1 mg of NP-Cy5 was reacted with 0.926 mg of NHS-PEG_{12}-maleimide ($sm(PEG)_{12}$) in 1 mL 0.1 M $NaHCO_3$ buffer (pH 8.5) for 30 minutes at room temperature. The excess crosslinker was removed with a Zeba spin column equilibrated in deionized water. The product was collected and split in two equal portions. The control NPs were synthesized by reacting with excess hydrolyzed Traut's reagent, while targeted NPs were

synthesized by reacting with 0.2 mg DN-SH (dissolved in 20 µL DMSO). After overnight rocking, the particles were purified with an S-200 column equilibrated into deionized water.

5.2.4. Physiological characterization of NP-DN

The core size and morphology were determined via TEM images obtained using an FEI TECNAI F20 TEM (Hillsboro, OR). The core diameters were analyzed using Image J to obtain average size and standard deviation. Hydrodynamic size, stability, and zeta potential were obtained using a DTS Zetasizer Nano (Malvern Instruments, Worcestershire, UK). DLS samples were prepared at 50 µg Fe/mL. Hydrodynamic size distribution was obtained in PBS, biological stability was analyzed in DMEM with 10% FBS and 1% antibiotic-antimycotic, and zeta potential was measured in 20 mM HEPES, pH = 7.4.

5.2.5 Quantification of Cy5 on NP

The number of Cy5 molecules per NP was determined using UV-vis spectroscopy. Samples of NP and NP-Cy5 were run at a concentration of 10 µg/ml. The spectrum of NP was subtracted from the spectrum of NP-Cy5, to properly blank the system. The absorbance at 646 nm, along with Cy5's extinction coefficient of 271,000 $L \cdot mol^{-1} \cdot cm^{-1}$ was used to determine the molar ratio of Cy5:NP to be 2:1

5.2.6 Chemical analysis by FTIR

FTIR spectra of DN, NP-TR, and NP-DN were obtained using a Nicolet 6700 spectrometer (Thermo Scientific Inc., Waltham, MA). The spectra were obtained at 4 cm^{-1} resolution and the signal was averaged over 64 scans. The samples were freeze-dried and ground

with a mortar and pestle to a fine powder. The powder was pressed into a pellet with KBr for analysis.

5.2.7 Quantification of DN per NP

The number of DN molecules per NP was determined using UV-vis spectroscopy. Samples of NP-TR and NP-DN were run at a NP concentration of 10 μg/ml. Additionally, standards of DN at 0–50 μg/ml in DMSO were analyzed at 275 nm, and the absorbance values were used to produce a standard curve. The difference in absorbance at 275 nm between the spectrum of NP-DN and the spectrum of NP-TR was calculated and fitted onto the standard curve. The molar ratio of DN:NP was evaluated to be ~137 DN/NP.

5.2.8 Viability of cells treated with NPs

Cells were seeded in a 96-well plate (2,000 cells per well) and incubated overnight. Cells were incubated with NP-TR and NP-DN at equivalent iron concentrations of 0–100 μg Fe/ml for 24 or 72 hours. Alamar Blue reagent (Invitrogen, Carlsbad, CA) was added and incubated for 2 hours following manufacturer's instruction. A microplate reader (Spectra i3, Molecular Devices, Sunnyvale, CA) was used to measure the fluorescence at 550 nm excitation and 590 nm emission.

5.2.9 Assessment of NP targeting

EM4 and EM4-hDAT cells were seeded onto 24-well plates (125,000 cells per well) and incubated overnight. Cells were then incubated with NPs at 50 μg/ml for 30 minutes at 37 °C, followed by washing thrice with PBS. Cells were trypsinized, fixed in 4% formaldehyde, washed and suspended in PBS. The samples were then analyzed by flow cytometry (FACSCanto, II, BD Biosciences).

5.2.10 Confocal imaging

Cells were plated on glass coverslips and attached overnight. Cells were then transfected as described above, washed thrice in PBS and fixed in 4% formaldehyde for 0.5 hours at room temperature. Cells were washed thrice with PBS to remove the formaldehyde, and were stained with WGA-AF555 and DAPI. Coverslips were mounted on slides with Prolong Gold antifade solution (Invitrogen, Carlsbad, CA). Images were taken on a LSM 510 Meta confocal fluorescence microscope (Carl Zeiss, Inc., Peabody, MA).

5.2.11 In vitro MR imaging

Quantitative T_2 MR imaging scan sequences were used to investigate the contrast enhancing capabilities of NP-DN. MR imaging was conducted on a Bruker Avance III 600 MHz, 14 T wide bore spectrometer. NP-DN in PBS were pipetted into glass vials (3.25 mm I.D., 5 mm O.D., 200 μL volume) at concentrations of 0–25 ug Fe/mL. The vials were fixed in place inside a water reservoir; the water served as a homogeneous background signal to minimize magnetic susceptibility variations near samples. The secured vials were placed in a 25-mm single-channel ^{1}H radiofrequency receiving coil (PB Micro 2.5). Quantitative T_2 values of NP-DN were measured using a multi-spin multi-echo (MSME) pulse sequence with TR = 2500 ms, TE = 6.7 + 6n ms (n = 0–16), and 78 × 156 μm^2 in-plane resolution with 0.5 mm slice thickness for 14 slices. Analysis of MR imaging data was accomplished with the FMRIB software library (FSL), Paravision 5.1 analysis package (Bruker), and ImageJ (NIH). T_1 values were determined within a circular, 100-voxel region of interest. Similarly, cells at 250,000 cells/mL were incubated with NP-DN and NP-TR at 100 μg Fe/ml in compete medium for 2 hours. The cells were washed

thrice with PBS and resuspended in 50 μL 0.5% agarose to fix the cells, which were analyzed in the same manner as described above.

5.3 Results and Discussion

5.3.1 Synthesis and characterization of NPs

The NP was synthesized as previously described.[84] The NP is composed of an iron oxide core that has shown to be an effective contrast agent for MRI in vitro and in vivo.[50,155] The PEG coating allows the NP to have great biocompatibility and biodegradability while offering terminal amine groups for conjugations.

The dopaminergic neurolabeler (DN) was synthesized following published methods.[153] **Figure 5-1a** schematically illustrates the synthesis of NP-DN. DN was first thiolated via reaction with succinimidyl 3-(2-pyridyldithio) propionate (SPDP), followed by reduction with tris(2-carboxyethyl) phosphine hydrochloride (TCEP). Concurrently, the NP was modified via a bifunctional PEG_{12}-crosslinker; the NHS-ester moiety of the PEG crosslinker was reacted to the amine-terminal-NP to form NP-mal. DN-SH was then reacted to the maleimide moiety of NP-mal to create NP-DN. Hydrolyzed Traut's reagent served as a dummy molecule for our non-targeted control NPs (NP-TR). **Figure 5-1b** shows a schematic representation of targeting and labeling of dopaminergic neurons by NP-DN.

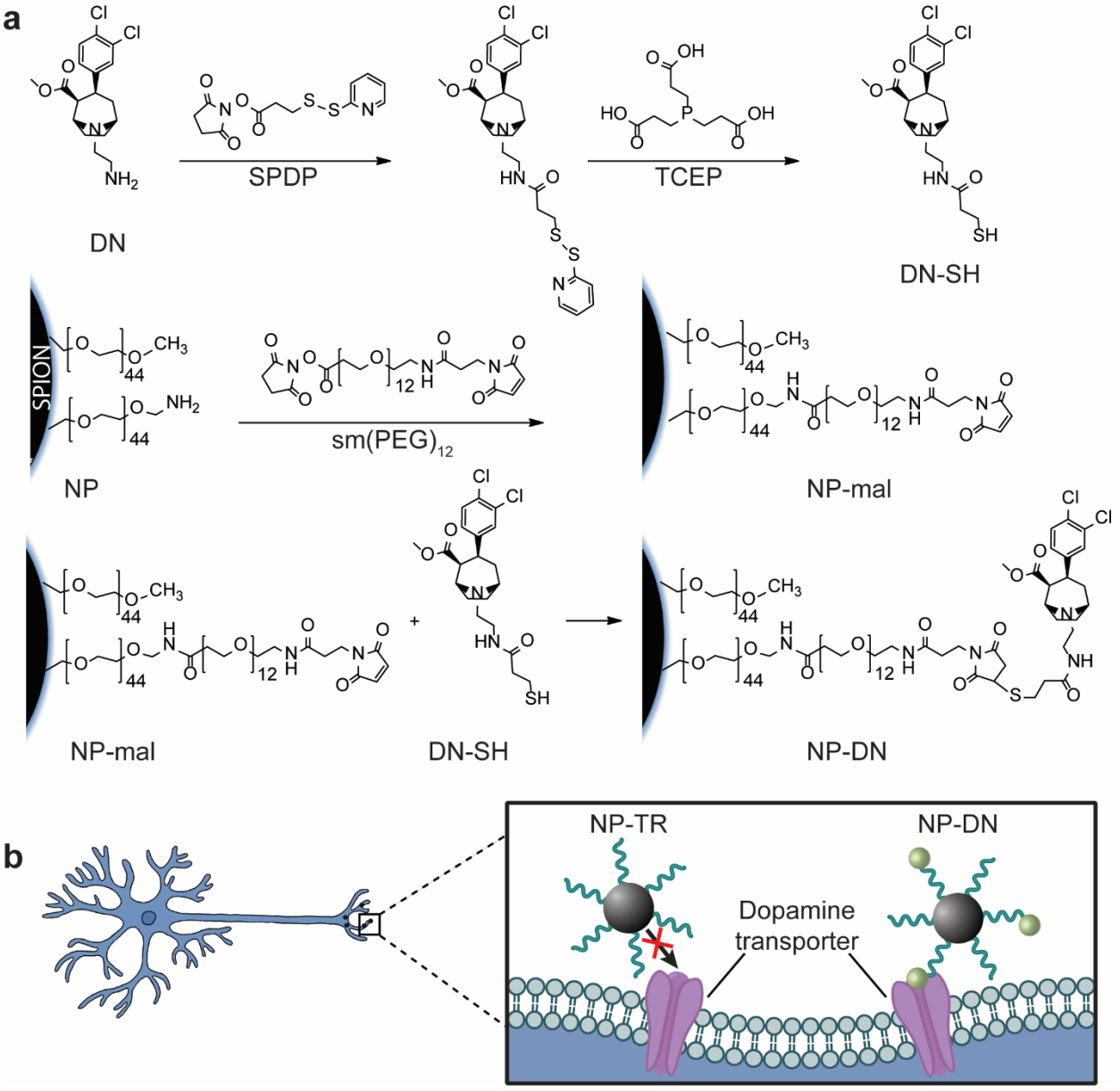

Figure 5-1. Synthesis of NP-DN and schematic representation of neuron labeling. (a) DN was modified via SPDP and TCEP to create thiolated DN-SH. Separately, NP was reacted with sm(PEG)$_{12}$ crosslinker, in which the amine group from the NP reacted with the NHS-ester moiety of the crosslinker to form NP-mal, leaving a terminal maleimide group. The thiol group from DN-SH is then reacted with the maleimide group of the NP-mal to form NP-DN. (b) Schematic representation of DAT-mediated labeling of neurons with NP-DN.

Table 5-1. Physiochemical properties of NP, NP-TR, and NP-DN.

	core size (nm)	hydrodynamic size (nm)	polydispersity index	zeta potential (mV)	DN/NP	Cy5/NP
NP	8.2 ± 0.7	25.9 ± 0.59	0.084	-8.78 ± 6.4	0	0
NP-TR	8.2 ± 0.7	29.1 ± 0.97	0.181	-9.2 ± 4.7	0	2
NP-DN	8.2 ± 0.7	30.2 ± 1.3	0.238	-9.23 ± 2.7	~137	2

The physiochemical properties of NP, NP-TR, and NP-DN are summarized in **Table 5-1**. The core morphology and size play important roles: the former can affect cellular uptake due to the differences in cellular interaction, while the latter affects the magnetic properties of iron oxide core.[156-158] TEM was used to identify the core size and morphology (**Figure 5-2a**). The iron oxide cores were spherical with an average diameter of 8 nm, which falls within the appropriate size range to enable superparamagnetism.[25]

Hydrodynamic size and zeta potential are important factors that influence NP interaction with physiological and cellular barriers. Dynamic light scattering (DLS) was used to obtain the hydrodynamic sizes and zeta potentials of NP, NP-TR, and NP-DN (**Figure 2b-d**). The NP had an average hydrodynamic size of 25.9 ± 0.59 nm with a polydispersity index of 0.084 in saline. The conjugation of ligand DN via bifunctional PEG_{12}-crosslinker to form NP-DN increased the hydrodynamic size to 30.2 ± 1.25 nm. Similarly, conjugation of hydrolyzed Traut's reagent via the same crosslinker to form NP-TR (non-targeted control) increased the size to 29.1 ± 0.97 nm. (**Figure 5-2b**). The addition of the PEG crosslinker is likely responsible for the increase in hydrodynamic size of NP-TR and NP-DN. Both NP-TR and NP-DN showed minimal growth in cell culture media (Dulbecco's modified Eagle's medium with 10% serum), demonstrating prolonged colloidal stability (**Figure 5-2d**). Both NPs remained within the optimal range of 10–100 nm preferable for in vivo application, wherein they are large enough to avoid filtration by the kidneys, yet small enough to avoid elimination by the mononuclear phagocyte system. Zeta

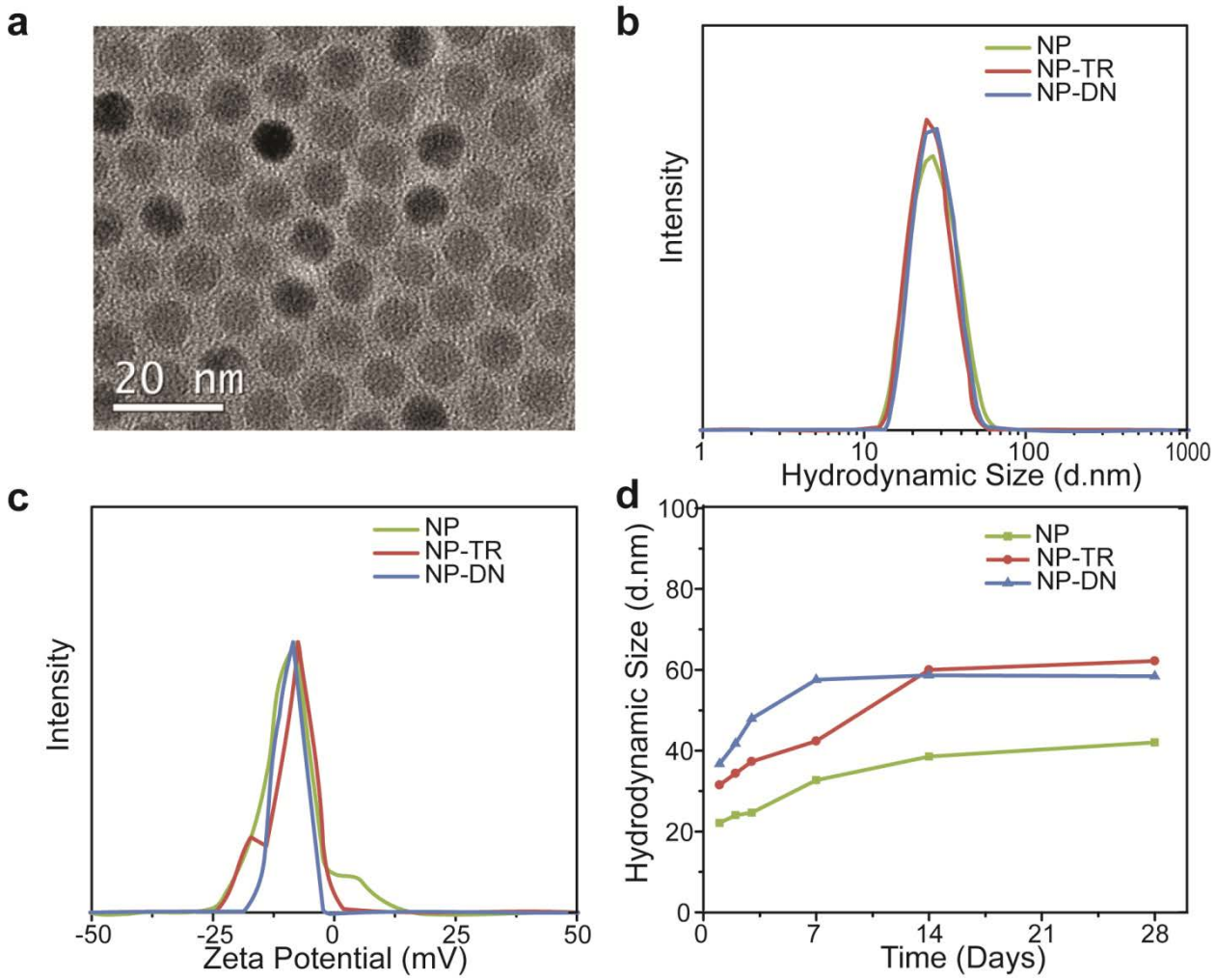

Figure 5-2. Physical properties of NPs. (a) TEM images of NP. (b) Hydrodynamic size distributions and (c) Zeta potential distributions of NP (purple), NP-TR (red), and NP-DN (blue). (d) Hydrodynamic sizes of NP (purple), NP-TR (red), and NP-DN (blue) in cell culture media at 37 °C as a function of time for a period of 28 days.

potential impacts nonspecific uptake through charge interactions. The zeta potential of the NP was measured to be –8.78 ± 6.41 mV, while NP-TR and NP-DN have zeta potentials of –9.2 ± 4.72 and –9.23 ± 2.72 mV, respectively (**Figure 5-2c**), both slightly negative or near neutral, minimizing electrostatic interaction with non-target cells and extracellular matrix.

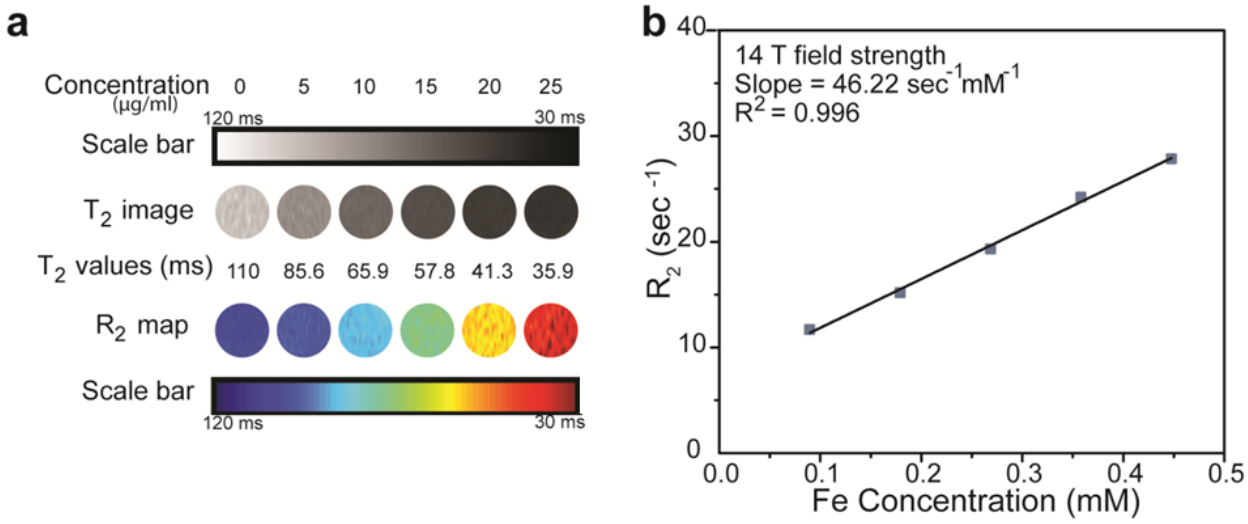

Figure 5-3. Magnetic properties of NP-DN. (a) T_2-weighted MR images and R_2 maps of MRI phantom images of NP-DN at various Fe concentrations. (b) Plot of R_2 as a function of Fe concentration. The slope of the fitted linear line gives the specific relaxivity of r_2.

The ability of NP-DN to serve as an MRI contrast agent is shown in **Figure 5-3a-b**. The T_2 signal intensity increases with increasing NP (i.e., Fe) concentration, and the resulting $1/T_2$ (R_2) vs. Fe concentration plot shows a linear relation, yielding a transverse relaxivity (slope of the curve) of 46.22 s^{-1} mM^{-1}, at 14 T field strength.

The conjugation of ligand DN was verified and quantified using FTIR and UV-vis spectroscopy, respectively. There are two representative FTIR peaks from DN: 1733 cm^{-1} from C=O stretching from the ketone attached to the tropane group, and 668 cm^{-1} from C-Cl bonds from the 3*β*-3,4-diCl-phenyl ring substitution on the tropane group (**Figure 5-4a**). These two representative peaks are not visible on the FTIR spectrum for NP-TR, but they are present on the FTIR spectrum for NP-DN, indicating DN is successfully conjugated onto NP-DN. DN exhibits a broad peak centered approximately at 275 nm under UV-vis (**Figure 5-4b**). The difference in absorbance of NP-TR (no DN) and NP-DN at 275 nm was used to calculate the amount of DN conjugated to NP-DN using Beer's Law. NP-DN exhibited ~137 molecules of DN per NP.

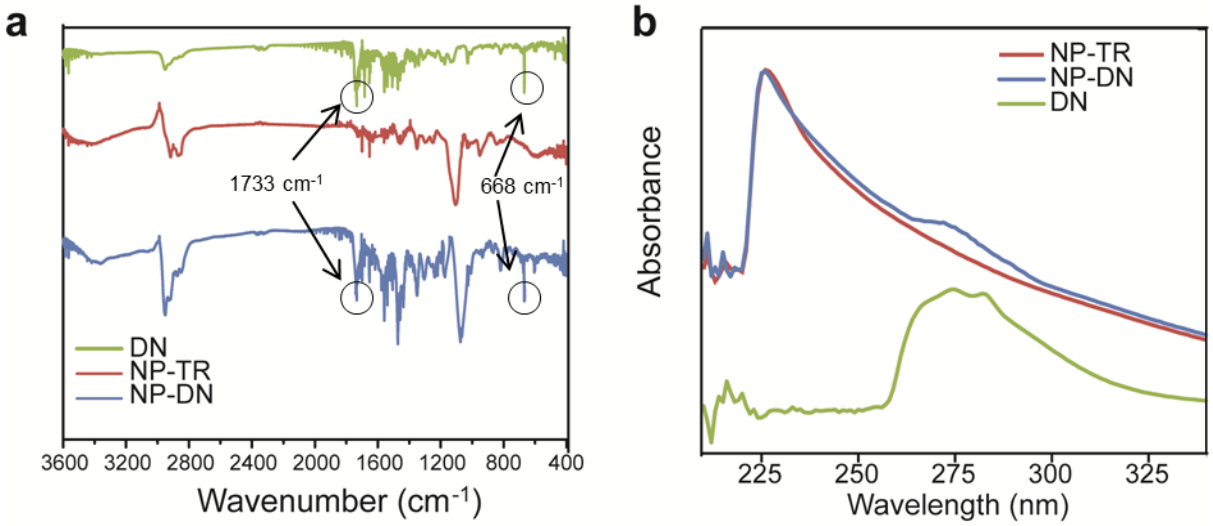

Figure 5-4. Chemical analysis of NP-DN. (a) FTIR spectra of DN (green), NP-TR (red), and NP-DN (blue). (b) UV-vis spectra of NP-TR (red), NP-DN (blue), and DN (green). The DN ligand exhibits a broad peak around 275 nm, corresponding to the shoulder peak of NP-DN spectrum.

Despite the large number of hydrophobic DN molecules per NP, the conjugation of DN did not affect the stability of NP-DN in a biologically relevant solution (**Figure 5-2d**).

5.3.2 Cell viability of NP-DNs

Effective in vivo application of NP-DN requires the NP formulation to be non-cytotoxic. It is common for small molecule targeting agents to be toxic due to their inherent hydrophobicity. Therefore, we tested the cell viability of both NP-TR and NP-DN on two cell lines: EM4 and EM4-hDAT. The EM4 cells are derived from the human embryonic kidney cell line, HEK 293, transfected with macrophage embryonic receptor to increase their culture plastic, and were used as the host cells for stable expression of hDAT. EM4-hDAT cells express the DAT (positive control, DAT^{+}) while the EM4 cells are devoid of the DAT (negative control, DAT^{-}). [159-164]

The two cell lines were treated at various NP concentrations in cell culture media for 24 and 72 hours, and cell viability was evaluated using Alamar Blue. **Figures 5a-b** show the viability for the DAT$^-$ cell line at 24 and 72 hours, respectively, while **Figure 5c-d** shows the

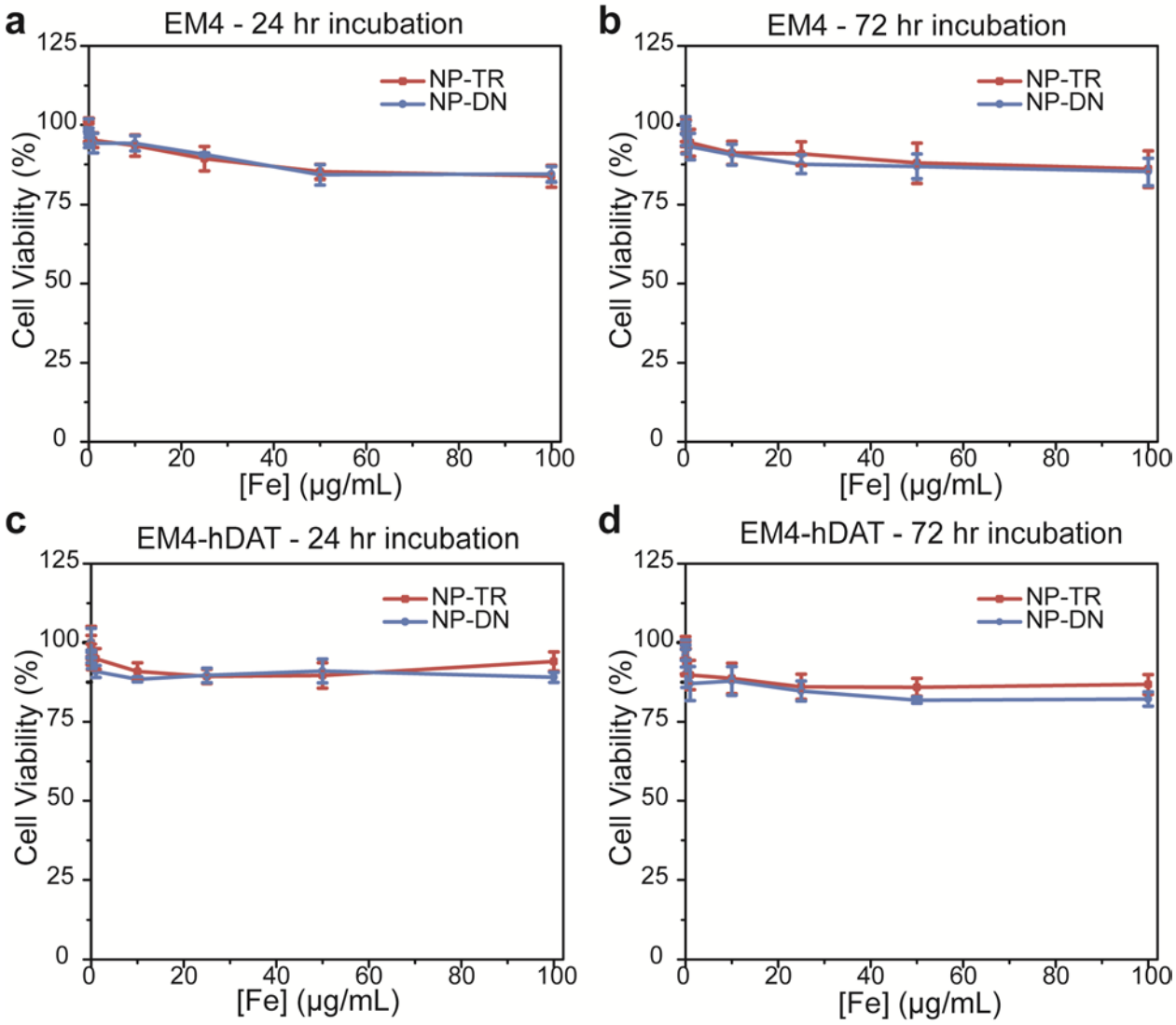

Figure 5-5. Cell viability of EM4 (DAT$^-$) and EM4-hDAT (DAT$^+$)cells treated with NP-TR and NP-DN. (a-b) Cell viability of EM4 cells as a function of Fe concentration after incubation for (a) 24 hr or (b) 72 hr with NP-TR (red) or NP-DN (blue) in cell culture media. (c-d) Cell viability of EM4-hDAT cells as a function of Fe concentration after incubation for (a) 24 hr or (b) 72 hr with NP-TR (red) or NP-DN (blue) in cell culture media.

viability for the DAT^+ cell line at 24 and 72 hours, respectively. Both NP-TR and NP-DN were minimally cytotoxic, even at the highest NP concentration (100 μg Fe/ml) after 72 hours of incubation, highlighting the biocompatibility of both NP-TR and NP-DN on dopaminergic neurons.

5.3.3 NP-DN targeting of DAT

Targeting specificity of NP-DN was evaluated using the DAT^+ and DAT^- cell lines. NPs were labeled with Cy5 fluorophore at a molar ratio of 2:1 Cy5:NP. DAT^+ and DAT^- cell lines were treated with equal amounts of NP-TR and NP-DN, and incubated for 2 hours at 37 °C. Following the incubation, the cells were fixed and analyzed by flow cytometry (**Figure 5-6a-c**). NP-TR and NP-DN exhibited some nonspecific labeling of DAT^- cells, but no significant difference was observed between NP-TR and NP-DN in the negative control cells (**Figure 5-6a**). Evaluation of NP-TR and NP-DN targeting of DAT^+ showed that NP-TR had similar labeling to the DAT^- cells, while the NP-DN exhibited a nearly 300% higher labeling than NP-TR on the DAT^+ cells. This suggests that the NP-DN is capable of targeting and labeling DAT expressing neurons.

NP targeting of DAT was further examined by MRI to demonstrate NP-DN can label DAT expressing cells and provide contrast in MRI. DAT^+ and DAT^- cells were treated with equal amounts of NP-TR and NP-DN for 2 hours, suspended in agarose, and imaged with a 14 T MRI magnet (**Figure 5-6d**). A considerable difference in contrast between samples was observed. The DAT^+ cell samples treated with NP-DN show considerably higher (more negative) contrast than do other samples. This suggests that NP-DN can specifically target and image neurons, and also serve as a contrast agent for MRI.

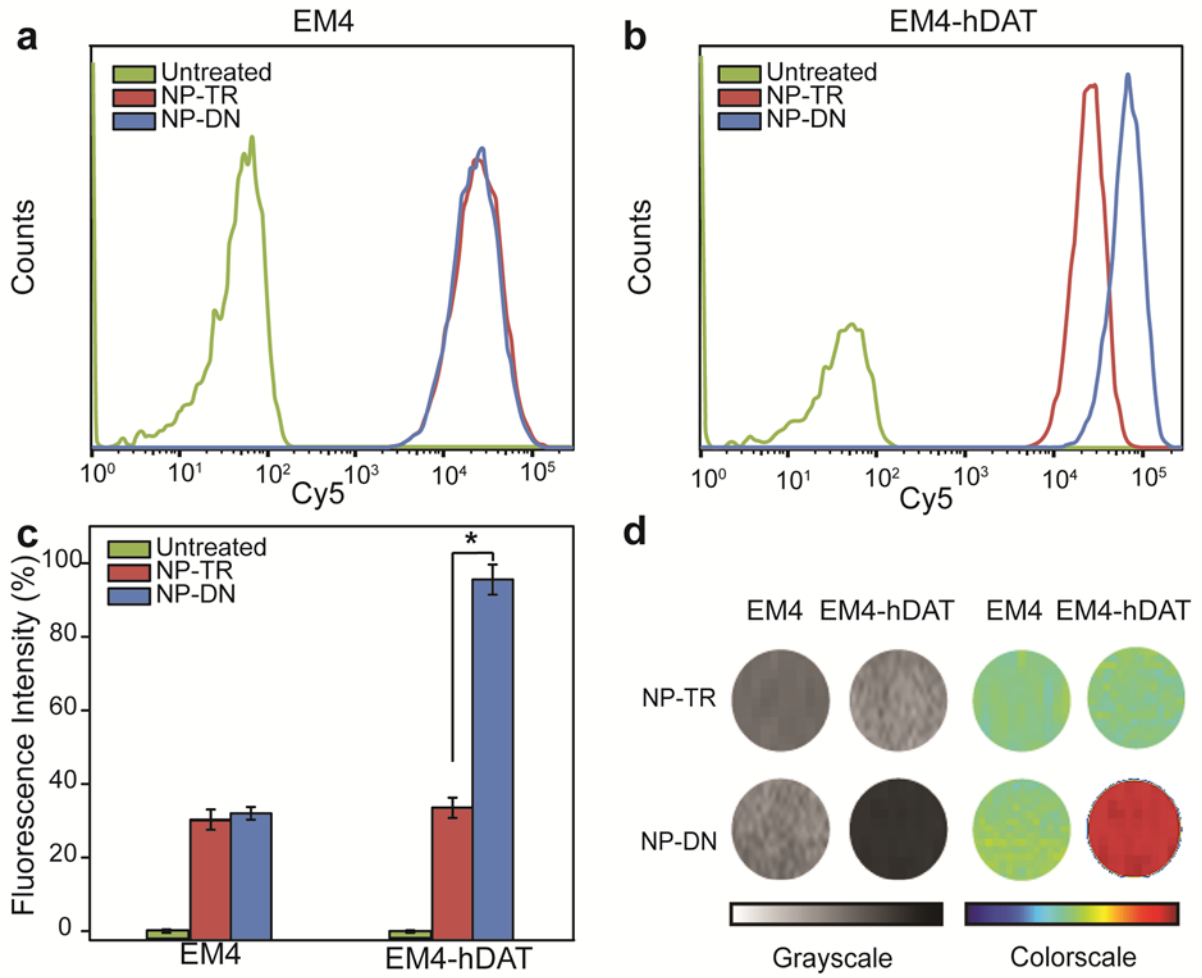

Figure 5-6. Flow cytometry analysis and phantom MR analysis of NP-DN targeting of DAT expressing cells. Cellular labeling of NP-TR and NP-DN on (a) EM4 (DAT^-) and (b) EM4-hDAT (DAT^+). (c) Quantitative mean fluorescence intensities of NP-TR and NP-DN from flow analysis (* $p < 0.0005$). (d) T_2-weighted and R_2-mapped images of NP-TR and NP-DN on EM4 and EM4-hDAT cells.

Confocal microscopy was used to visualize NP-DN targeting of DAT^+. DAT^+ and DAT^- cells were incubated in cell culture media containing Cy5-labeled NP-TR or NP-DN at equal concentration for 2 hours (**Figure 6-7**). Cells were then fixed and stained to visualize the nuclei (blue, first column) and membranes (red, second column) via DAPI and WGA-555, respectively. The NPs fluoresce green in the third column, and the overlay image is shown in the last column, indicating NP-DN specifically labels DAT^+ cells. Cocaine analogues have proven to possess high affinity to the DAT, specifically by the 3-phenyltropane group. Additionally, DN possesses

a 3*β*-3,4-diCl-phenyl ring substitution on the tropane ring (**Figure 5-1a**), which has demonstrated optimal DAT affinity.[153,165] EM4-hDAT cells treated with NP-DN show considerably higher NP labeling than DAT^+ cells treated with NP-TR and DAT^- cells treated with either NP-TR or NP-DN. Meanwhile, NP-TR show minimal labeling in both cell lines. This result indicates that the NP-DN can target and label DAT expressing cells, and thus can be used to effectively image dopaminergic neurons.

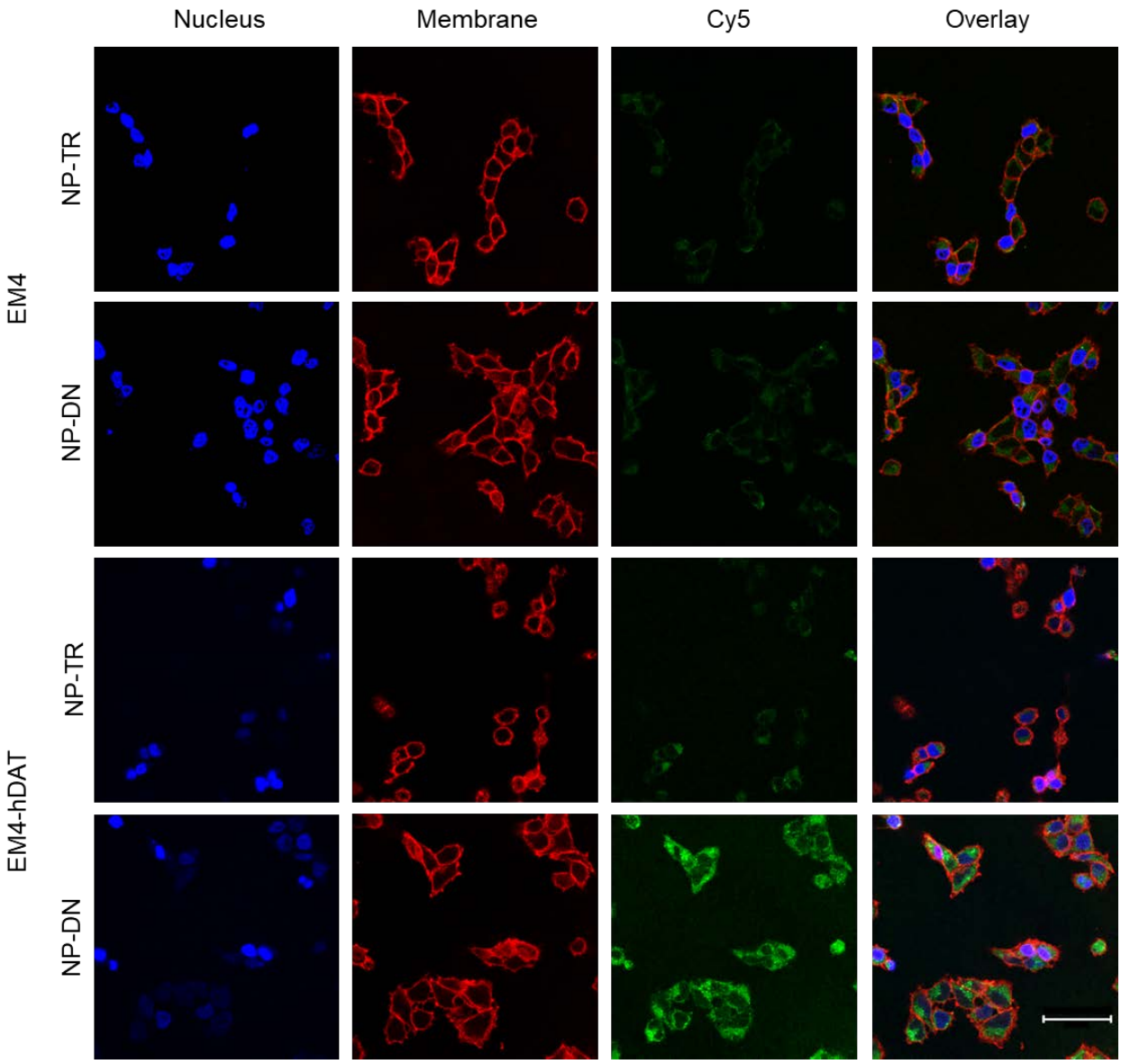

Figure 5-7. Confocal fluorescence images of EM4 (DAT^-) and EM4-hDAT (DAT^+) cells treated with NP-TR and NP-DN. EM4 cells (top two rows) and EM4-hDAT (bottom two rows) were treated for 2 hrs with either NP-TR or NP-DN. The first column shows nuclei stained in blue, the second column shows the membrane stained in red, and the third column shows the fluorescent NP-TR and NP-DN in green, and the fourth column shows the overlay of all three. The scale bar corresponds to 50 µm.

5.4 Conclusions

Iron oxide nanoparticles conjugated with a dopaminergic neuron targeting ligand, DN, were developed to label and image dopaminergic neurons by MRI. The NPs displayed great

biocompatibility and long-term stability in cell culture media, and were monodisperse and of appropriate size demonstrating favorable characteristics for in vivo applications. The ligand DN on the NP was quantified via UV-vis spectroscopy. Cell viability assessment of NP-TR (non-targeted control) and NP-DN produced minimal toxicity. Flow cytometry analysis demonstrated that NP-DN exhibited a nearly 300% increase in labeling of EM4-hDAT (DAT^+) cells as compared to NP-TR. DAT^+ cells treated with NP-DN showed considerably higher (more negative) MR contrast than cells treated with NP-TR. Confocal microscopy showed that DAT^+ cells treated with NP-DN showed vastly higher labeling compared to NP-TR. These results indicate the great potential of NP-DN to successfully label and image neurons in vivo, taking a step forward in bringing MR-based neuroimaging to the clinical setting.

6. *Paclitaxel-Loaded Iron Oxide Nanoparticles for Targeted Breast Cancer Therapy*

Paclitaxel (PTX) is a potent drug for treating advanced solid carcinomas, however, its clinical utility is limited by its poor water solubility. Despite the promise of using nanoparticles to deliver hydrophobic PTX, achieving sufficient drug loading while maintaining small particle size and stability in biological media remains a challenge. Here we present a PTX nanoparticle (NP) formulation with small size and great stability, that targets breast cancer cells, and enables controlled release of PTX. This NP formulation (NP-PTX-FA) comprises a superparamagnetic iron oxide core coated with short- and long-chain polyethylene glycol (PEG): the former for conjugation of hydrophobic PTX and folic acid (FA), and the latter as an outer layer for improved hydrophilicity. The NP-PTX-FA has a uniform size distribution (averaging 28.2 ± 0.64 nm) and high drug loading capacity of 22.8 wt.% (vs. <10 wt.% normally). NP-PTX-FA released the drug under conditions mimicking the acidic intracellular pH of breast cancer cells and the FA conjugation led to higher NP uptake by target cells, enhancing the cytotoxicity to target cells compared to free PTX. This NP formulation holds great promise to improve breast cancer therapy, and potential to deliver other hydrophobic drugs for treating various cancer types.

6.1. Introduction

Despite recent advances in cancer treatment technology, chemotherapy remains the preeminent treatment option, with more than 50% of all cancer patients receiving some form of chemotherapy.[166] Paclitaxel (PTX) in particular has garnered significant interest due to its great potency in treating advanced solid carcinomas, including lung, ovarian, and breast cancer.[167] PTX promotes and stabilizes microtubules and inhibits late G1 or M phases of the cell cycle to induce cell death.[168] Clinically, PTX is administered under the trademark “Taxol,” which is a

formulation of PTX in dehydrated ethanol and polyoxyethylated castor oil. Despite of PTX's strong potency, the clinical applications are limited by its poor water solubility (~0.4 μg/mL), and non-specific biodistribution.[169] Poor water solubility often leads to early clearance of the drug from the body while nonspecific drug release can harm healthy tissue, hindering the translation of many hydrophobic drugs to clinical settings.[170] Though Taxol attempted to solve the issue of the poor water solubility by using different solvents, the approach causes severe side effects such as nephrotoxicity, neurotoxicity, and cardiotoxicity[171], increasing the urgent need of more effective methods of delivering anti-cancer drugs like PTX.

Nanoparticle-based drug delivery systems have shown great promise in solving many of the issues surrounding chemotherapeutic drug delivery. Nanoparticle (NP) systems can improve the water solubility of hydrophobic drugs to improve pharmacokinetic profiles, enhancing biocompatibility to reduce side effects. Additionally, these NPs can provide active targeting by conjugation of tumor-specific ligands and control drug release via cleavable bonds that respond to the acidic conditions of tumor microenvironments.[74,88,172-174] Biological barriers constrain particle sizes to 10–100 nm range (the kidneys clear out particles <10 nm, and the liver and spleen remove particles >100 nm).[64] Due to the severe hydrophobicity of chemotherapeutic drugs, achieving high drug loading while meeting the size constraints remains a challenge for all NP systems. For example, many PTX-loaded metallic and iron oxide NPs can achieve the appropriate size typically in the range of 20–100 nm but often have a poor drug loading capacity of <10 wt.%.[82-85] In contrast, many liposomal nanocarriers can achieve high drug loading, but they are often large in size (100–400 nm) resulting in a poor blood half-life leading to early clearance.[175-177] Abraxane®, an albumin-bound PTX nanoformulation approved by the FDA for metastatic breast cancer therapy, has a similarly large size of 130 nm and low loading capacity of

10 wt.%.[178,179] Active targeting can also be incorporated into NP systems to limit off-target effects of chemotherapeutics, but adding hydrophobic targeting agents means additional difficulties in maintaining appropriate size and achieving adequate drug loading. Any NP formulation seeking to improve PTX delivery must address these challenges.

Here, we report the development of a superparamagnetic iron oxide nanoparticle (SPION) system with small particle size, high drug loading, and pH-dependent drug release for targeted breast cancer therapy. SPIONs have proven to be both biocompatible and biodegradable, and provide strong contrast in magnetic resonance imaging (MRI), which can be used to monitor treatment in real time.[10] The SPION core is coated with a dual-layer of polyethylene glycol (PEG): an inner layer where the hydrophobic PTX and folic acid (FA) are conjugated, and an outer layer to improve hydrophilicity. This dual layer system allows high drug loading without the loss of stability that is common among other metallic NPs. PTX was modified with an acid-labile linker so that its release occurs only in the acidic compartments of tumor cells or acidic microenvironment of the tumor. Additionally, FA was conjugated to target the folate receptor, because several epithelial tumors, including breast cancer, over-express the folate receptor.[180] Various physiochemical properties including core size, hydrodynamic size, zeta potential, and stability of NPs in biological media were characterized. Drug loading and release profiles were also characterized. Cell targeting, internalization, and viability studies were conducted on highly-aggressive murine 4T1 mammary epithelial carcinoma cells to evaluate the in vitro efficacy.

6.2. Experimental

6.2.1 Materials

All materials were purchased from Sigma-Aldrich (St. Louis, MO) unless otherwise stated. Paclitaxel was purchased from LC Laboratories (Woburn, MA). Cy5-NHS ester was purchased from Lumiprobe (Hunt Valley, MD). Functionalized PEGs were purchased from Laysan Bio, Inc. (Arab, AL).

6.2.2 Synthesis of NP-PTX-FA

Base NP (Fe_3O_4 core + PEG) was first synthesized using a previously reported method with noted adjustments. Briefly, 8 nm oleic-acid coated iron oxide nanoparticles were formed via thermal decomposition of iron-oleate complex.[7] A ligand exchange was then performed following an established procedure with adjustments:[23] for every 50 mg of oleic-acid coated iron oxide, $mPEG_{2k}$-NH_2 (375 mg, 0.1875 mmol) and H_2NHN-PEG_{600}-$NHNH_2$ (240 mg, 0.4 mmol) were used to form the base NP. PTX was carboxylated using succinic anhydride to form PTX-COOH.[181] PTX-COOH was then activated by 1'-carbonyldiimidazole (CDI). PTX-COOH (0.2 mg, 0.2 mmol) and CDI (0.324 mg, 0.2 mmol) were dissolved in DMSO (20 μL), and sonicated at 40°C for 2 hours. Following the reaction, the activated PTX was added to 2 mg of NP dissolved in DMSO (0.8 mL) with DIPEA (5 μL). The solution was rocked overnight, followed by purification via dialysis in methanol until no free PTX was detected, and then the NP-PTX transferred into 0.1 M $NaHCO_3$ (pH 8.5) buffer. Following PTX conjugation, folic acid (FA) was activated by CDI: FA (0.2 mg, 0.4 mmol) and CDI (0.073 mg, 0.4 mmol) were dissolved in DMSO (20 μL), and sonicated at 40°C for 2 hours. The activated FA was added to 1 mg of NP-PTX and rocked overnight. The resulting NP-PTX-FA was purified via dialysis in 0.1 M

$NaHCO_3$ (pH 8.5) buffer until no free FA was detected. The purified NP-PTX-FA was transferred into DI water. NP-PTX, without further conjugation of FA, was used as control in this experiment. For targeting experiments, Cy5 was conjugated to NP prior to PTX and FA conjugation to ensure normalized Cy5 labeling among all NP formulations: NP was reacted with Cy5-NHS ester at a ratio of 10 NP:1 Cy5 by mass in thiolation buffer (pH = 8). Excess Cy5 was removed via S200 column, and the ratio of Cy5:NP was determined to be 2:1 by UV-vis spectroscopy.

6.2.3 NP core size and zeta potential characterization

TEM images of NPs were obtained using an FEI TECNAI F20 TEM (Hillsboro, OR). Iron oxide core diameters were analyzed using ImageJ to obtain size distribution, mean diameter, and standard deviation. Hydrodynamic size and zeta potential of the NPs in this experiment were obtained using a DTS Zetasizer Nano (Malvern Instruments, Worcestershire, UK). The particles were analyzed at 50 μg/mL in DI. The distribution of particles was obtained in PBS while the stability of the particles was analyzed in DMEM with 10% FBS and 1% antibiotic-antimycotic.

6.2.4 Chemical analysis by FTIR

FTIR spectra were obtained using a Nicolet 6700 spectrometer (Thermo Scientific Inc., Waltham, MA). The spectra were obtained at 4 cm^{-1} resolution and the signal was averaged over 64 scans. The samples were pressed into a pellet with KBr for analysis.

6.2.5 Quantification of PTX and FA conjugations

PTX conjugation was quantified using HPLC. The column used was Magic Bullet C-18 Column (Michrom Bioresources, Auburn, CA) (25 mm, tapered ID 2.1 to 0.5 mm and 5 um). To

cleave the ester bond to release the PTX from the NP, 0.5 mg of NP-PTX-FA was dissolved in trifluoroacetic acid (TFA). The released PTX was extracted in acetonitrile (ACN). The mobile phase was composed of phase A (DI water with 0.1% TFA) and phase B (ACN with 0.1% TFA) at a flow rate of 1 mL/min. Then, 10 μL of the extracted PTX was measured at a wavelength of 227 nm at 40°C. The sample was run with 50% mobile phase A and 50% mobile phase B for 10 minutes, followed by thorough washing of the column. Similarly, standards of PTX were measured in the same manner to develop a standard curve of PTX.

PTX conjugation was further verified using UV absorbance, and FA conjugation was quantified using UV absorbance. Standard linear-fit curves of free PTX and FA were created by plotting the UV-vis spectra at various concentrations at 227 nm and 272 nm, respectively. NP samples were run at 10 μg/mL. The concentrations of PTX and FA were determined by subtracting the background absorbance of NP from the absorbance spectrum of NP-PTX and NP-PTX-FA with a normalized amount of iron.

6.2.6 Drug release

We dialyzed 0.5 mg of NP-PTX-FA using an 8kDa MWCO dialysis membrane against 20 mL of varying buffers: 0.1 M MES buffer (pH 5.4) and 0.1 M PBS buffer (pH 7.4). At predefined time intervals, 1 mL aliquots were retrieved and replaced with 1 mL of fresh buffer. The samples were analyzed with HPLC in the same manner as described previously.

6.2.7 Targeting and internalization

6.2.7.1 Targeting

We seeded 4T1 cells into 24-well plates (125,000 cells per well) and incubated overnight. Cells were then incubated with NPs at 25 μg/mL for 30 minutes at 37°C, followed by washing with PBS. Cells were trypsinized, fixed in 4% formaldehyde, washed, and suspended in PBS. Cellular uptake of NPs was quantified by flow cytometry (FACSCanto II, BD Biosciences).

6.2.7.2 Internalization

This process is similar to the experiment for targeting, except that treated cells were plated on glass coverslips, and detached overnight. Cells were washed with PBS and fixed in 4% formaldehyde. Membrane was stained with WGA-AF555 (Invitrogen, Carlsbad, CA). Coverslips were mounted on microscope slides with Prolong Gold antifade solution (Invitrogen, Carlsbad, CA) containing DAPI for nuclei staining. Images were acquired on a LSM 510 Meta confocal fluorescence microscope (Carl Zeiss, Inc., Peabody, MA).

6.2.8 Viability studies

Cells were seeded in a 96-well plate (2,000 cells per well) and incubated overnight. Cells were incubated with PTX, NP, NP-PTX, or NP-PTX-FA at equivalent PTX concentrations of 0–150 μM. Cells were treated for 24 or 48 hours. Cell viability was determined using the Alamar Blue assay. Following incubation with the dye, a microplate reader (SpectraMax i3, Molecular Devices, Sunnyvale, CA) was used to determine the fluorescence intensity at 550 nm excitation and 590 nm emission. The fluorescence intensity of treated cells was compared to the fluorescence intensity of untreated cells to determine viability.

6.3 Results and discussion

6.3.1 Synthesis and characterization of NP-PTX-FA

Figure 6-1 shows a schematic representation of the synthesis of NP-PTX-FA. The base NP is composed of an iron oxide core, coated with PEG of two different lengths: 2000 MW (methoxy terminated) and 600 MW (hydrazide terminated). The iron oxide core was synthesized via thermal decomposition of iron oleate, resulting in oleic acid coated SPION.[7] The oleic acid was then displaced via a ligand exchange, and PEG was grafted to produce a hydrophilic iron oxide nanoparticle. The longer-chain PEG (methoxy terminated) acts to stabilize the particle system by increasing water solubility and minimizing cross-linking and aggregation. The reactive hydrazide of the shorter-chain PEG allows easy conjugation of various molecules; the hydrazide group was chosen over the amine group due to its higher reactivity.[182] The short length of the reactive PEG allows conjugation of hydrophobic molecules closer to the iron oxide core, minimizing the hydrophobic interaction on the polymer surface that otherwise could lead to clearance of NPs.[170] This allows high drug loading while maintaining appropriate particle size and stability. We followed a published procedure to modify PTX by using succinic anhydride to form a carboxylic acid functionalized PTX (PTX-COOH) containing a cleavable ester bond (**Figure 6-1a**).[181] PTX-COOH was then conjugated to the hydrazide group on the NP via 1'-carbonyldiimidazole (CDI) chemistry (Figure 1c). Similarly, CDI was used to conjugate folic acid onto the NP (**Figure 6-1b-c**).

Figure 6-1c shows a schematic representation of the synthesis of NP-PTX-FA. The base NP is composed of an iron oxide core, coated with PEG of two different lengths: 2000 MW (methoxy terminated) and 600 MW (hydrazide terminated). The iron oxide core was synthesized via thermal decomposition of iron oleate, resulting in oleic acid coated SPION.[7] The oleic acid

was then displaced via a ligand exchange, and PEG was grafted to produce a hydrophilic iron oxide nanoparticle. The longer-chain PEG (methoxy terminated) act to stabilize the particle system by increasing water solubility and minimize cross-linking and aggregation. The reactive hydrazide of the shorter-chain PEG allows easy conjugation of various molecules; the hydrazide group was chosen over the amine group due to its higher reactivity.[182] The short length of the reactive PEG allows conjugation of hydrophobic molecules closer to the iron oxide core, minimizing the hydrophobic interaction on the polymer surface that otherwise could lead to clearance of NPs.[170] This allows high drug loading while maintaining appropriate particle size and stability. PTX was modified using succinic anhydride following a published procedure to form a carboxylic acid functionalized PTX (PTX-COOH) containing a cleavable ester bond (Figure 1a).[181,183] PTX-COOH was then conjugated to the hydrazide group on the NP via 1'-carbonyldiimidazole (CDI) chemistry (Figure 1c). Similarly, CDI was used to conjugate folic acid onto the NP (Figure 1b-c).

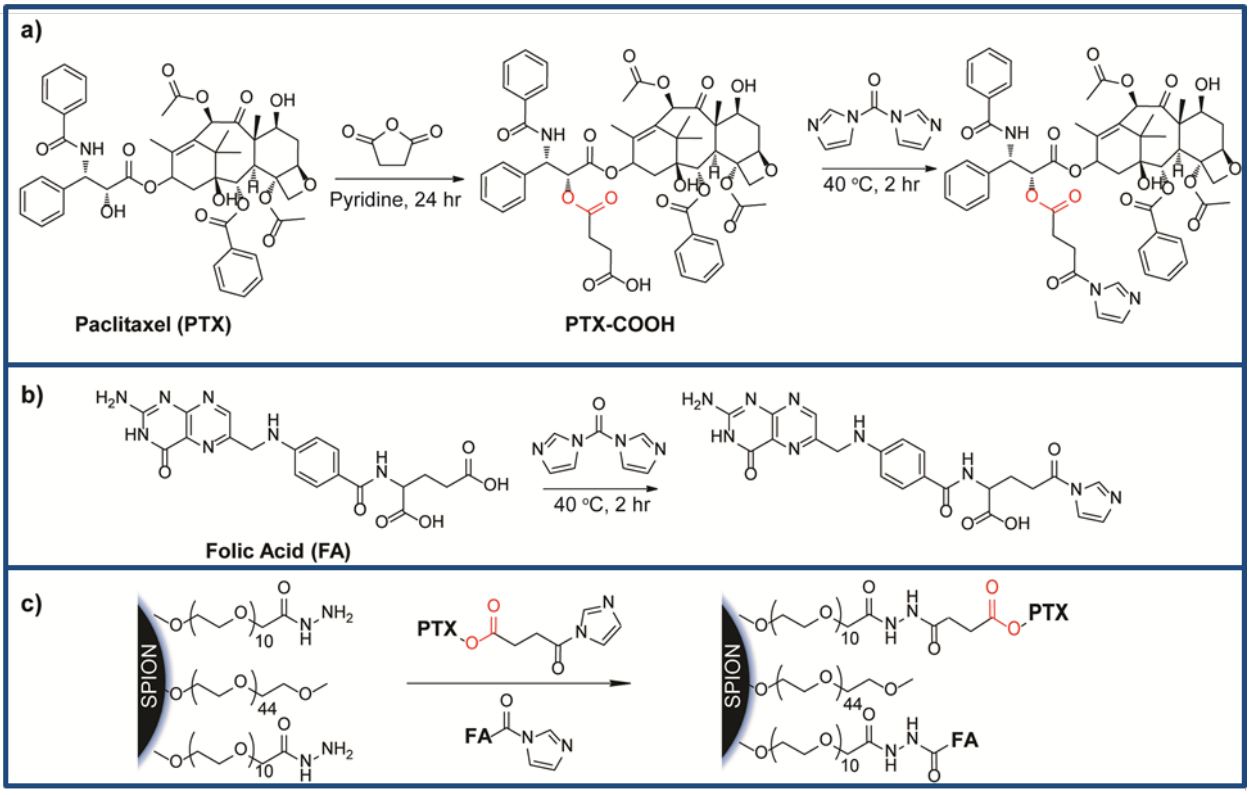

Figure 6-1. Synthesis of NP-PTX-FA. (a) PTX was modified to create PTX-COOH, which has a pH-sensitive ester bond (in red). Then, 1,1'-carbonyldiimidazole (CDI) was used to activate the carboxylic acid. (b) FA was modified via CDI chemistry to activate the carboxylic acid. (c) The activated PTX and FA were conjugated to iron oxide NPs to form NP-PTX-FA.

Table 6-1 summarizes basic physiochemical properties of NP, NP-PTX, and NP-PTX-FA. The morphology and core size of the iron oxide core were determined using TEM (**Figure 6-2a**). The core was spherical in shape and 7.9 ± 0.6 nm in diameter. We used dynamic light scatting (DLS) to obtain the intensity-based hydrodynamic sizes and zeta potential. The base NP had an average hydrodynamic size of 24.6 ± 0.62 nm and a polydispersity index of 0.095 in PBS. PTX and FA conjugation minimally increased the hydrodynamic size to 28.24 ± 0.64 nm (**Figure 6-2b**); the particle maintained this size over a period of one month in biological media (Dulbecco's modified Eagle's medium (DMEM) with 10% FBS and 1% AA) (**Figure 6-2d**), indicating great stability in the presence of serum proteins. The minimal growth after the

Table 6-1. Physicochemical properties of NP, NP-PTX, and NP-PTX-FA.

	core size (nm)	hydrodynamic size (nm)	polydispersity index	zeta potential (mV)	PTX molecules/NP; % by weight	FA molecules/NP
NP	7.9 ± 0.6	24.6 ± 0.62	0.095	-5.22 ± 3.21	0; 0 wt.%	0
NP-PTX	7.9 ± 0.6	25.3 ± 0.41	0.155	-10.5 ± 6.48	~162; 22.8 wt.%	0
NP-PTX-FA	7.9 ± 0.6	28.2 ± 0.64	0.251	-13.1 ± 5.71	~162; 22.8 wt.%	~82

conjugation can be attributed to the shorter reactive PEG that keeps these molecules sequestered from the surface, demonstrating the effectiveness of the dual-layer system. This NP system maintains a hydrodynamic size well within the 10–100 nm range needed to minimize clearance by the spleen, liver, and kidneys.[64] The zeta potential of NP-PTX-FA was measured to be –13.1 ± 5.71 mV (Figure 6-2c). Zeta potential regulates NP interaction with cells and extracellular matrices.[184] Since most cells have negative surface charge, it is desirable to have a system that is slightly negative or near neutral to minimize off-target cell-nanoparticle interaction.[126]

Conjugation and component quantification were characterized using FTIR, HPLC, and UV-vis spectroscopy. After conjugating PTX and FA, thorough purification was made via dialysis until no free PTX and FA were detected in the dialysate via UV-vis spectroscopy. Compared to the spectrum of NP, NP-PTX-FA displayed accentuated peaks at ~1609 cm^{-1} and 828 cm^{-1} (**Figure 6-3a**). The former is due to C=O stretch from the amide bond formations from the conjugation of PTX and FA, while the latter is due to C-H bending from the aromatic groups in PTX and FA. This confirms the presence of amide bonds from both PTX and FA. Then UV-vis spectra of NP, NP-PTX and NP-PTX-FA were acquired to ensure both molecules were present. The resulting blanked spectrum overlaid with PTX and FA spectra is shown in **Figure 6-3c**. The shoulder peaks at 227 nm and 272 nm are characteristic of PTX and FA, respectively,

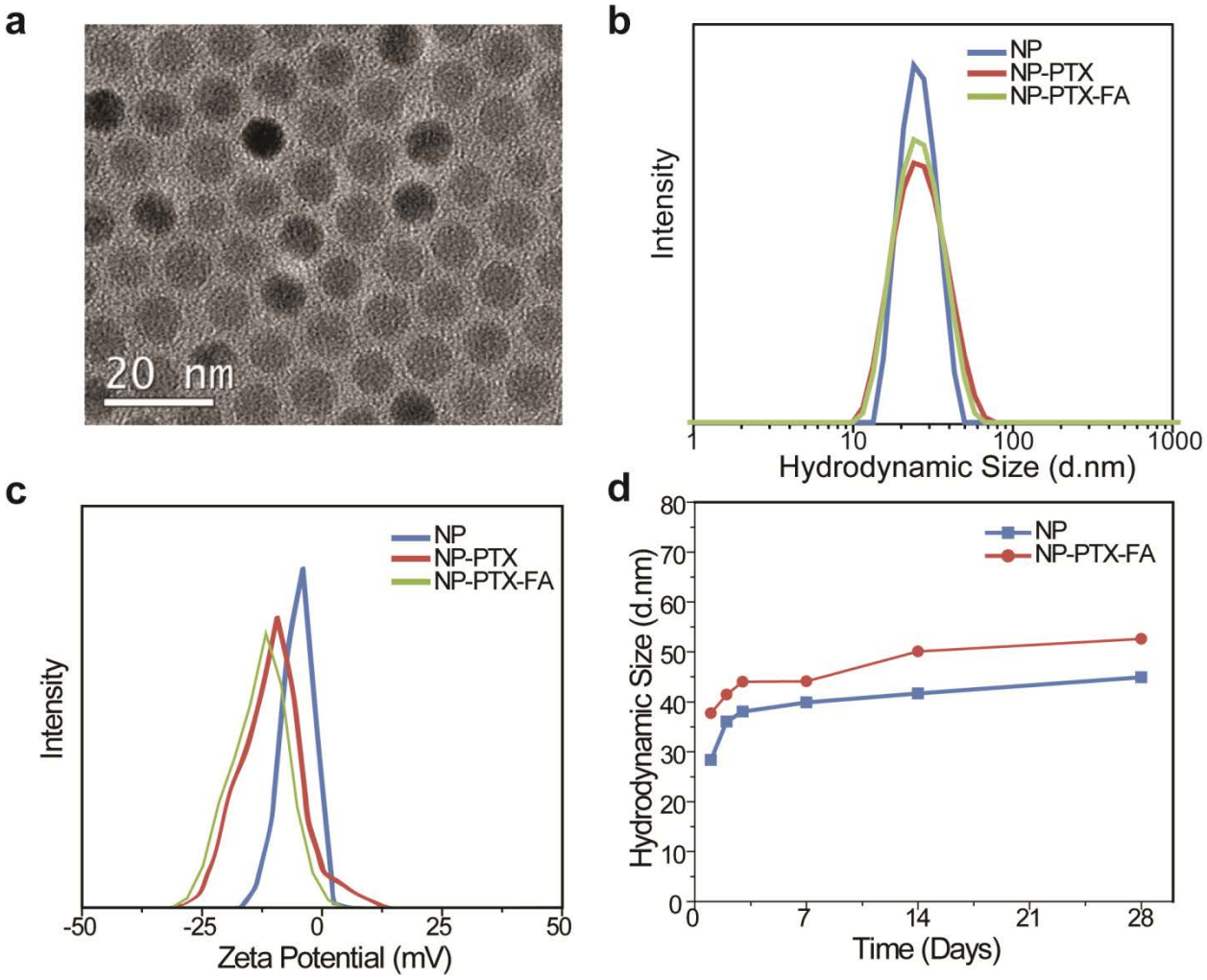

Figure 6-2. Morphology, size, stability, and zeta potential of NP-PTX-FA. (a) TEM images of NP-PTX-FA. (b) Hydrodynamic size distributions of NP (blue), NP-PTX (red) and NP-PTX-FA (green). (c) Zeta potential distributions of NP (blue), NP-PTX (red), and NP-PTX-FA (green). (d) Hydrodynamic size of NP and NP-PTX-FA in cell culture media at 37°C over a course of 28 days.

confirming the presence of the both molecules.[172,185] The amount of PTX and FA was quantified by using Beer's Law and spectrophotometry; approximately 173 PTX molecules and 82 FA molecules per NP were detected. To verify the high PTX loading capacity, NP-PTX-FA was further analyzed using HPLC. Briefly, a known amount of NP-PTX-FA was dissolved in trifluroacetic acid (TFA) to cleave the ester bonds to release the PTX. The PTX was extracted using acetonitrile, which was then analyzed using HPLC. The elution profile of the

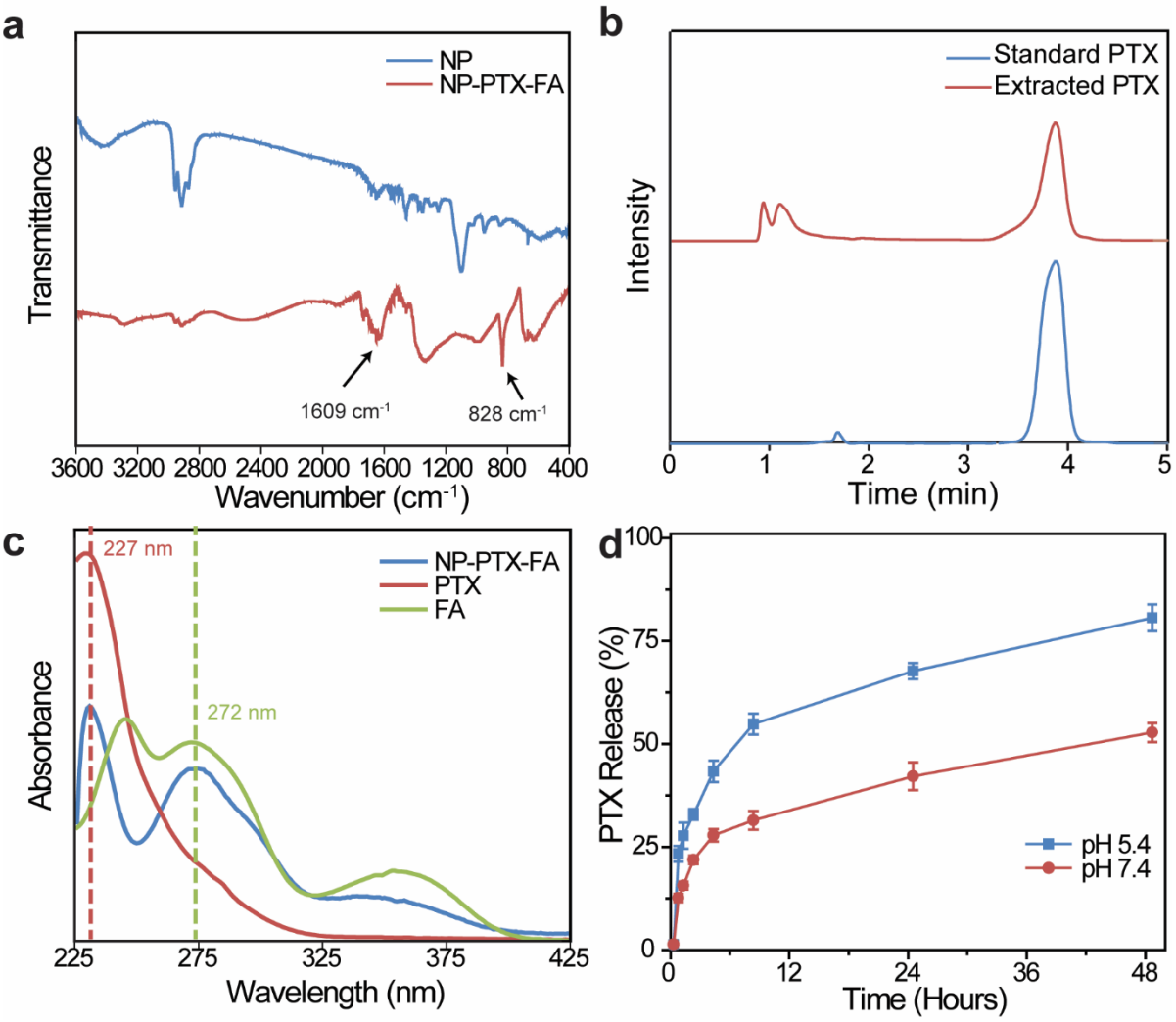

Figure 6-3. Chemical analysis of NP-PTX-FA. (a) FTIR spectra of NP (blue) and NP-PTX-FA (red). (b) HPLC chromatogram of standard PTX (blue) and extracted PTX (red) from NP-PTX-FA. (c) UV-vis spectra of NP-PTX-FA (blue), PTX (red) and FA (green). (d) PTX release curves of NP-PTX-FA at pH 5.4 (blue) and pH 7.4 (red) determined by UV-vis spectroscopy.

extracted PTX was consistent with standard PTX, seen in **Figure 6-3b**. HPLC results showed approximately 162 PTX molecules per NP, consistent with the UV-vis results. The discrepancy could be explained by not all of PTX being extracted for HPLC. This correlates to a loading capacity of ~22.8 wt.% PTX/Fe, which is substantially higher than the 10 wt.% provided by PTX solid core nanoformulations.[83,84,186,187] The high drug loading while achieving small size and stability is due to the presence of a dual PEG layer: the hydrophobic molecules are bound to the

short-chain PEG close to the core, which minimizes the hydrophobic interaction, while the long-chain PEG provides steric stability and hydrophilicity. Importantly, PTX and FA conjugations did not affect solubility of the NPs in water. NP-PTX-FA showed great solubility with no precipitation at 1 mg/mL, which correlates to 240.3 μg PTX/mL in water; this is a ~600 fold greater than the water solubility of free PTX.

6.3.2 pH-dependent drug release

PTX was modified using succinic anhydride to form an ester derivative PTX-COOH. This previously established approach creates a hydrolytic ester bond that breaks down in acidic environments.[181] The hydrolytic ester bond facilitates PTX release in tumor microenvironments while minimizing release in the higher pH environment of the bloodstream. In vitro drug release was evaluated in two physiological conditions: PBS, pH 7.4 and MES buffer, pH 5.4 (**Figure 6-3d**). Unlike many drug formulations that display initial burst release, NP-PTX-FA showed a slow, gradual release with minimal release in neutral pH. On the other hand, ~83% of PTX was released in an acidic environment in 48 hours. This indicates that upon reaching the tumor cells, PTX will be preferentially released in endosomes and lysosomes, minimizing non-targeted drug release.

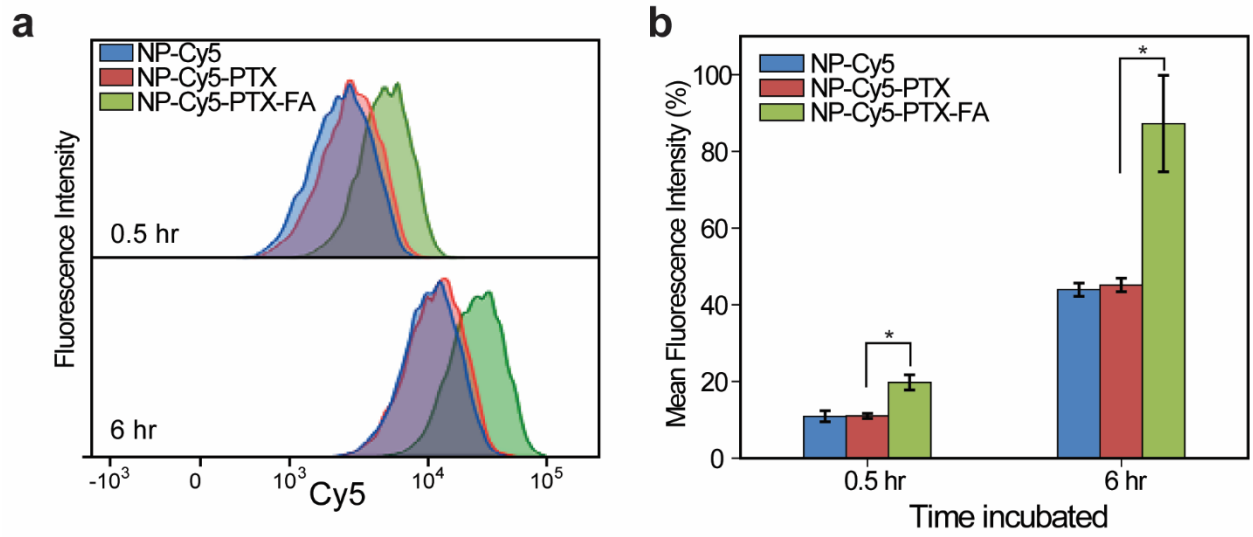

Figure 6-4. Flow cytometric analysis of 4T1 cells treated with NP-PTX-FA. (a) Cellular uptake of NP-Cy5 (blue), NP-Cy5-PTX (red), NP-Cy5-PTX-FA (green) by 4T1 cells incubated for 0.5 hr (upper panel) and 6 hr (lower panel). (b) Quantitative mean fluorescence intensities from cells treated with various NP formulations, obtained from flow cytometric analysis (*$p < 0.05$ by Student's t-test, sample size n = 3).

6.3.3 Targeting, internalization, and enhanced cell killing of NP-PTX-FA

For PTX to be delivered effectively to tumor cells and minimize off-target side effects, NPs must be able to target and bind to tumor cells with high specificity. Folic acid has proven to have high affinity towards folate receptors that are over-expressed in many solid tumors, including breast cancers.[74-77]

Targeting specificity of the NPs to tumor cells was accessed using 4T1 cells. This cell line was chosen because murine 4T1 mammary epithelial carcinoma is widely used as a model of human breast cancer; it shares many features of stage IV breast cancer including its metastatic behavior and its overexpression of the folate receptor. All NPs were labeled with Cy5 flurophore for flow cytometry and confocal imaging. We treated 4T1 cells with equal amounts of NP-Cy5, NP-Cy5-PTX or NP-Cy5-PTX-FA, and incubated for 0.5 hour or 6 hours at 37°C. After incubation, the cells were fixed and analyzed with flow cytometry, and the results are shown in

Figure 6-4a-b. Nonspecific uptake of NPs was observed, but the FA conjugation considerably enhanced the uptake of NPs to target cells as compared to control NPs. The FA-conjugation nearly doubled the uptake of NPs by cells, suggesting NP-PTX-FA are capable of targeting breast cancer cells.

To confirm cellular internalization of the NPs, we used confocal microscopy on murine mammary carcinoma cells of 4T1. Cells were treated with NP-Cy5-PTX as control or NP-Cy5-PTX-FA for 0.5 hours. Cells were fixed after treatment, stained with DAPI for the nuclei (blue, first column) and WGA-555 for the membrane (green, second column), and imaged with a confocal fluorescence microscope (**Figure 6-5**). The particles labeled with Cy5 can be seen in the treated cells in the third column in red. The overlay image (fourth column) reveals that the particles were internalized in the cells. As 4T1 cells express folate receptors on the surface, FA-conjugated NPs are likely internalized into cells through a receptor-mediated mechanism. Comparing the images of cellular uptake of NP-Cy5-PTX vs. NP-Cy5-PTX-FA, reveals that the FA-conjugation increased the cellular uptake for both 0.5-hour and 6-hour incubations. After 0.5-hour incubation, NP-Cy5-PTX-FA showed visibly higher uptake than NP-Cy5-PTX, and after 6-hour incubation, NP-Cy5-PTX-FA showed substantially higher uptake than NP-Cy5-PTX. This visualization shows consistency with the flow cytometry results that FA conjugation does indeed enhance cellular internalization of the NPs.

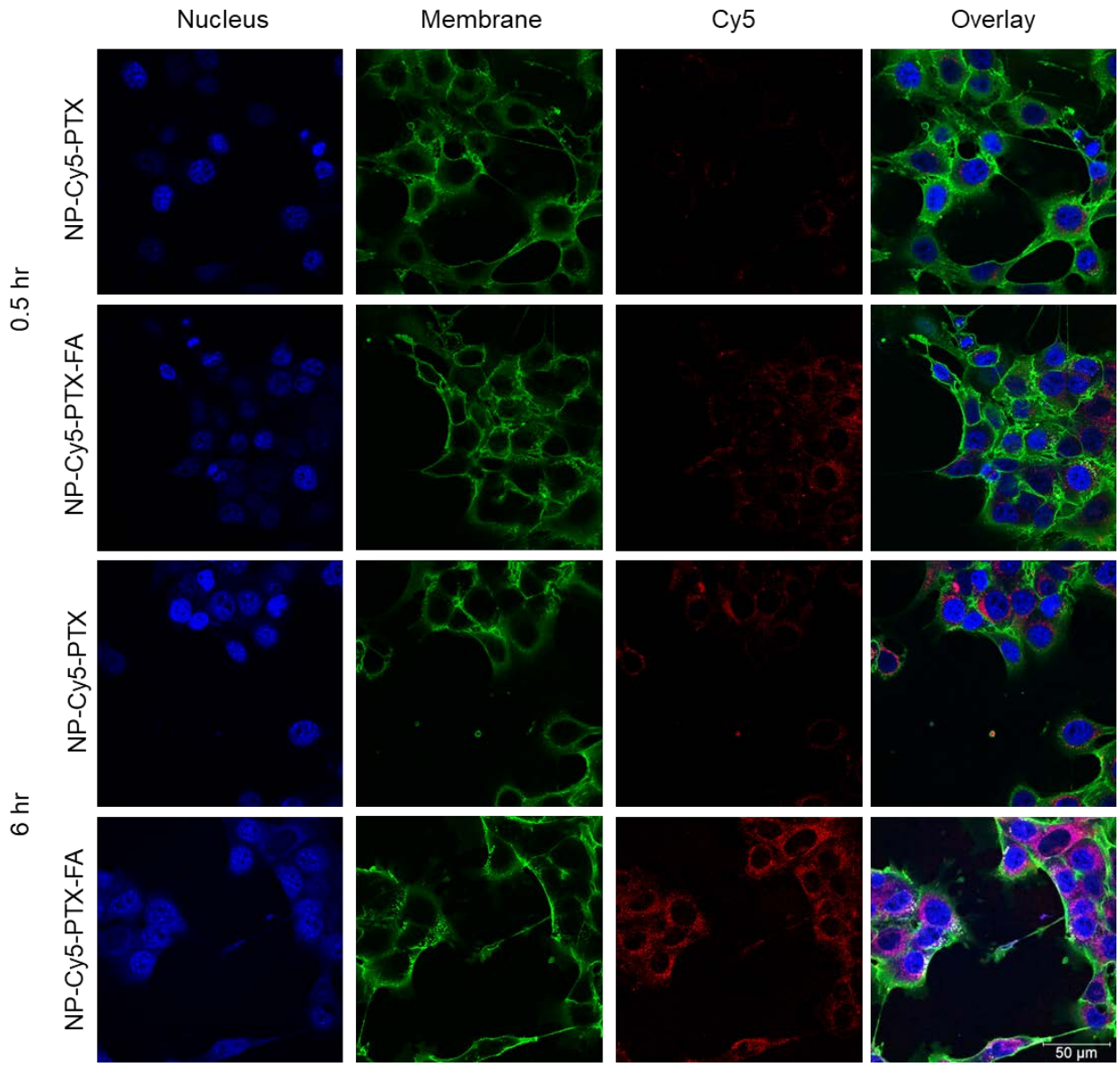

Figure 6-5. Confocal fluorescence images of 4T1 cells treated with NP-Cy5-PTX (nontargeted) or NP-Cy5-PTX-FA (targeted). Cells were treated for 0.5 hour (top two rows) and 6 hours (bottom two rows) at 37°C. The first column shows cell nuclei stained in blue, the second column shows cell membrane in green, the third column show the fluorescent NP-Cy5-PTX and NP-Cy5-PTX-FA in red, and the last column show the overlay of all three images for each row.

To evaluate the efficacy of NP-PTX-FA on cell killing, 4T1 cells were treated with free PTX, NP, NP-PTX, and NP-PTX-FA for 24 and 48 hours, and cell viability was evaluated with the Alamar Blue assay. **Figure 6-6a and 6-6b** show the cell viability curves after 24-hour and 48-hour incubation, respectively. As seen in both viability curves, incubation time had an impact

on the efficacy of PTX. Almost an order of magnitude difference in IC50 values was observed (**Figure 6-6c-d**). Base NPs showed little to no cell killing, indicating the base NPs are non-cytotoxic. Free PTX was potent in killing cells, with IC50 values of 91 ± 8 μM and 29 ± 1 μM after 24-hour and 48-hour incubation, respectively. The non-targeted NP-PTX showed slightly enhanced cell killing, with IC50 values of 58 ± 4 μM and 14 ± 0.2 μM after 24-hour and 48-hour incubation, respectively. This is likely due to the improved hydrophilicity of the NP system. The conjugation of FA to NPs significantly enhanced the killing compared to non-targeted NP-PTX, with IC50 values of 15 ± 7 μM and 1.2 ± 0.2 μM after 24-hour and 48-hour incubation, respectively. This can be explained due to the enhanced cellular uptake of FA-conjugated NPs that was shown earlier in targeting and internalization results. This shows that NP-PTX-FA is more potent than PTX, with the added benefits of higher water solubility while maintaining a small size, long-term serum stability, ability to be detected under MRI, effective targeting, and controlled drug release.

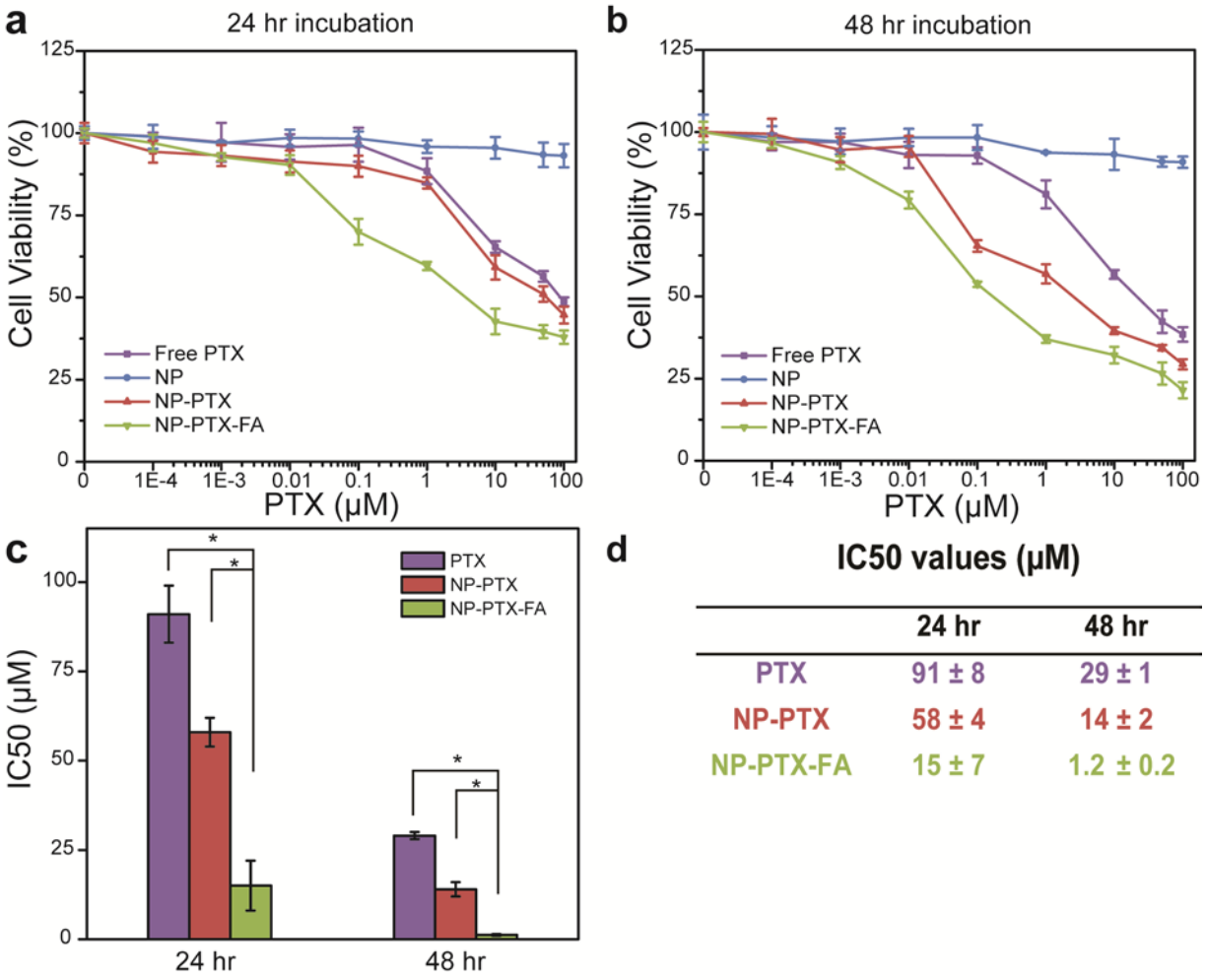

	24 hr	48 hr
PTX	91 ± 8	29 ± 1
NP-PTX	58 ± 4	14 ± 2
NP-PTX-FA	15 ± 7	1.2 ± 0.2

Figure 6-6. In vitro efficacy of various PTX treatments on 4T1 cell line. (a-b) Cell viability as a function of PTX dose after incubation for (a) 24-hour or (b) 48-hour with NP (blue), NP-PTX (red), NP-PTX-FA (green), or free PTX (purple). (c-d) IC50s of free PTX (purple), NP-PTX (red) or NP-PTX-FA (green) treated 4T1 cells after 24 hour or 48 hour incubation (*$p < 0.01$ by Student's *t*-test).

6.4 Conclusions

SPIONs conjugated with PTX and FA were developed for improved drug loading for treatment of breast cancer. This NP formulation has a dual-layer of PEG: short-chain layer for conjugation of hydrophobic PTX and FA, and long-chain layer to increase water solubility. This design helps to overcome the issues of aggregation and poor drug loading capacity exhibited by

many other nanoformulations. These NPs were monodispersed, exhibited excellent stability in biological media, and possessed the small size and surface charge favorable for in vivo application. FTIR and UV-vis confirmed the successful conjugation and quantification of PTX and FA, and UV-vis also confirmed high drug loading and a pH-dependent drug release profile that preferentially releases the drug in tumor microenvironments. Flow cytometry results showed that the FA conjugation enhanced NP uptake in breast cancer cells, indicating successful targeting of breast cancer cells. Viability studies showed that NP-PTX-FA can kill breast cancer cells as effectively as free PTX with additional benefits of improved solubility, imaging capability, and targeted and controlled drug release. Additionally, PTX and FA are versatile drugs and targeting agents for various cancers, so this nanoformulation can be potentially applied to other cancer types.

7. Development of IONPs as T_1 contrast agents

7.1 Introduction

GBCAs are the dominant contrast agents used in the clinic today. However, GBCAs have demonstrated severe side effects that have prompted the FDA to issue many warnings, raising public safety concerns and highlighting the need for non-toxic alternatives. IONPs are an attractive option, yet their magnetic properties largely depend on the synthesis of the core. The factors affecting thermal decomposition are poorly understood, and need further investigation to achieve precise control over the size of IONPs. Using the parameters discussed in Chapter 4, we synthesized and characterized a promising IONP-based T_1 contrast agent. The efficacy of this T_1 contrast agent was evaluated using phantom MRI, and its biocompatibility was demonstrated via cell viability studies on three glioblastoma cell lines.

7.2 Experimental

7.2.1 Materials

All materials were purchased from Sigma-Aldrich (St. Louis, MO) unless otherwise stated.

7.2.2 Synthesis of IOOA

We synthesized oleic acid-coated iron oxide nanoparticles following published methods[7], with modifications. To test the effects of aging time, we altered the time from 30 minutes to 10, 20, 45, and 60 minutes. To test the effects of ramping rate, w altered it from 3.3 °C/min to 2, 2.2, 2.5, 3, and 3.8 °C/min. We tested the effects of stir rate from 300–800 rpm.

7.2.3 Synthesis and purification of phosphine oxide-terminal PEG (mPEG-PO)

We synthesized phosphine oxide-terminal PEG following published methods with modifications.[188] Methoxy-PEG_{2000}-OH was dispersed in toluene, and stirred with phosphoryl chloride ($POCl_3$) at room temperature under nitrogen gas at a molar ratio of 1 $POCl_3$:3 PEG. After 24 hours of stirring, the product was precipitated in hexanes and collected via centrifugation at 6000 rpm for 10 minutes. The product then was dispersed in DI water to hydrolyze remaining chloride groups on the phosphine oxide into hydroxyl groups. The product was frozen and lyophilized to form powdered phosphine oxide-terminal PEG (mPEG-PO).

7.2.4. Ligand exchange with 4 nm IOOA to form water soluble 4 nm IONP

Method: Disperse 20 mg of IOOA into 1 mL hexanes. Disperse 350 mg of mPEG-PO in 1 mL of ethanol. Transfer both to a round bottom flask, seal with a septum, and purge with nitrogen gas. Stir at 70 °C for 4 hours at 200 rpm. After 4 hours of stirring, let the flask come to RT. Transfer the sample to a 15 mL centrifugal tube. Fill with hexanes and centrifuge at 3000 rpm for 5 minutes, and discard the supernatant. Suspend the IONP pellet in 2 mL of EtOH. Fill with hexanes again and centrifuge at 3000 rpm for 5 minutes. Suspend the IONP pellet in 1 mL DI water and transfer to 1.5 mL centrifugal tube. Centrifuge at 10,000 rpm for 10 minutes to remove aggregates. Collect the supernatant and purify via S-200 sephacryl resin equilibrated with deionized water.

7.2.5. 4 nm IONP characterization

TEM images of IOOAs were obtained using an FEI TECNAI F20 TEM (Hillsboro, OR). Core diameters were analyzed using ImageJ, and 100 samples were analyzed to obtain size distribution, mean diameter, and standard deviation. Hydrodynamic size and zeta potential of the

NPs in this experiment were obtained using a DTS Zetasizer Nano (Malvern Instruments, Worcestershire, UK). The particles were analyzed at 50 μg Fe/mL in DI. The distribution of particles was obtained in PBS while the stability of the particles was analyzed for 2 weeks in DMEM with 10% FBS and 1% antibiotic–antimycotic.

7.2.6 Phantom MR imaging

We used T_1-weighted, T_2-weighted, quantitative T_1, and quantitative T_2 magnetic resonance imaging scan sequences to investigate the contrast enhancing capabilities of T_1 IONP. MRI measurements were conducted on a Bruker 4.7 T, 30 cm bore magnet. T_1 IONP in phosphate buffered saline was pipetted into glass vials (3.25 mm I.D., 5 mm O.D., 200 μL volume). The vials were fixed in place inside a water reservoir; the water served as a homogeneous background signal to minimize magnetic susceptibility variations near the samples. The secured vials were placed in a 38 mm ^{1}H radiofrequency quadrature coil (Doty SAIP200-H-38-M). Relaxation properties of T_1 IONP were quantitatively evaluated with a quantitative T_1 rapid imaging with refocused echoes and variable repetition time (RARE-VTR) pulse sequence with echo time (TE) of 6.5 ms, TR = 200 ms, 400 ms, 800 ms, 1500 ms, 3000 ms, and 5000 ms, and 148 x 102 μm^2 in-plane resolution with 1.0 mm slice thickness for one slice. Quantitative T_2 values were measured using a multi-spin multi-echo (MSME) pulse sequence with TR = 2000 ms, TE = 8.5 x n ms (n = 1-25), and 148 x 102 μm^2 in-plane resolution with 1 mm slice thickness for 5 slices. T1-weighted images were acquired with a RARE pulse sequence with TE = 7.0 ms, TR = 1200 ms, and 114 x 78 μm^2 in-plane resolution with 1 mm slice thickness for 5 slices; T_2-weighted images were acquired with a RARE pulse sequence with TE = 27 ms, TR = 820 ms, and 142 x 100 μm^2 in-plane resolution with 1 mm slice thickness for 8 slices. Analysis of MRI data was accomplished with the FMRIB software library (FSL), Paravision 6.0 analysis package

(Bruker), and ImageJ (NIH). T_1 and T_2 values were determined within a circular, 100-voxel region of interest**.**

7.2.7 Cell culture

Three different glioblastoma cell lines (U87, U118, and SF767) were selected for this study. U87 cells were cultured in Minimum Essential Media (MEM) containing 10% Fetal Bovine Serum (FBS) and 1% Penicillin Streptomycin (Pen Strep). U118 and SF767 were cultured in Dulbecco's Modified Eagle's Medium (DMEM) containing 10% FBS and 1% Pen Strep. All the cell lines were grown and passaged according to ATCC recommendations for less than six months after the time of resuscitation.

7.2.8 Cell viability

Cells were seeded in a 96-well plate (6,000 cells per well) and incubated overnight. Cells were incubated with T_1 IONP at concentrations from 0–100 μg/mL. Cells were treated for 24 hours. Cell viability was determined using the Alamar Blue assay. Following incubation with the dye, we used a microplate reader (SpectraMax i3, Molecular Devices, Sunnyvale, CA) to determine the fluorescence intensity at 550-nm excitation and 590-nm emission. The fluorescence intensity of treated cells was compared to the fluorescence intensity of untreated cells to determine viability.

7.3 Results and discussion

7.3.1 Effect of heating rate

In the original Hyeon et al. paper, the methods section specifically state a heating rate of 3.3 °C/min without explanation, and many studies have followed suit in maintaining this heating

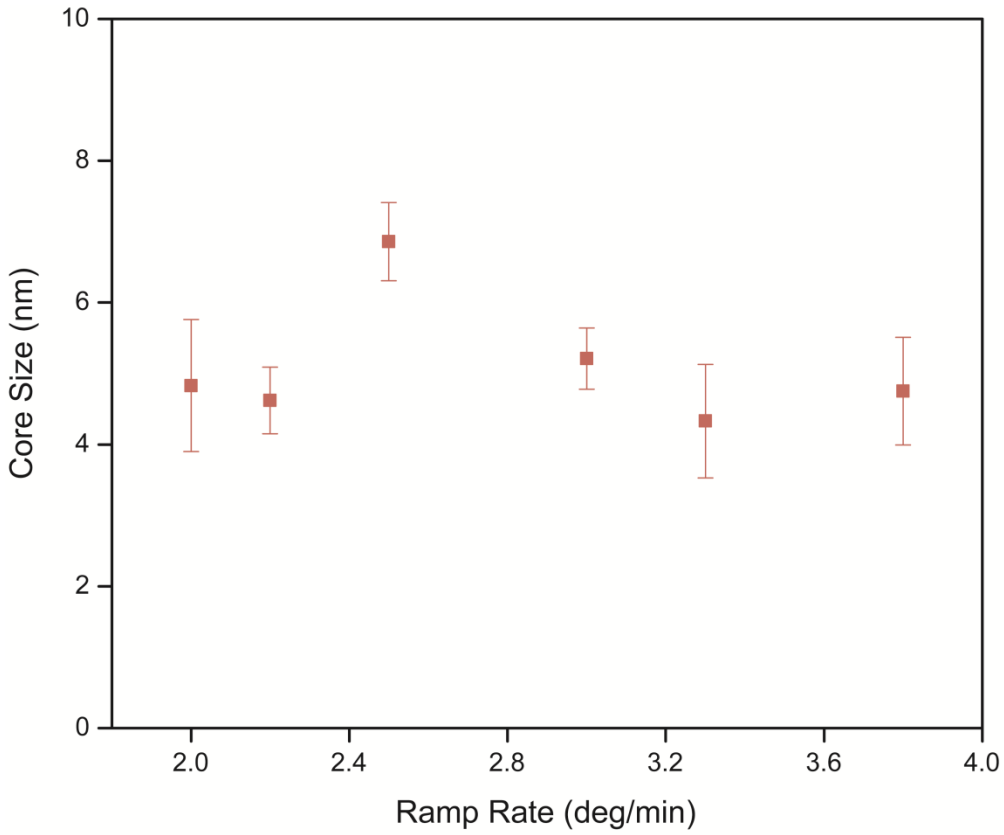

Figure 7-1. The effect of heating rate on the average core size of IOOAs. No noticeable correlation was found between heating rate and core size.

rate of 3.3 °C/min. However, no justification was provided for this precise rate, and in an effort to investigate its significance, IOOA were synthesized with varied heating rates (from 2 – 3.8 °C/min), while holding stirring and aging time constant. The results are seen in **Figure 7-1.**

Altering the heating rate did not show any significant difference in core size of the NPs It is possible that 3.3 °C/min was chosen to have some control over the release of monomers into the mixture. However, as this study shows, 3.3 °C/min does not seem to not have significance.

7.3.2 Effect of aging time

The original Hyeon paper reports a clear separation in nucleation and growth; the authors attribute successful uniform NPs to the distinct delineation between nucleation and growth. They

report nucleation triggered at 200 – 240 °C , and major growth occur at ~300 °C. However, they provide no justification for keeping the aging time at 30 minutes. However, three years later, another member in the same group has found that aging time alters the morphology of the IOOAs, seen in **Figure 7-2**.

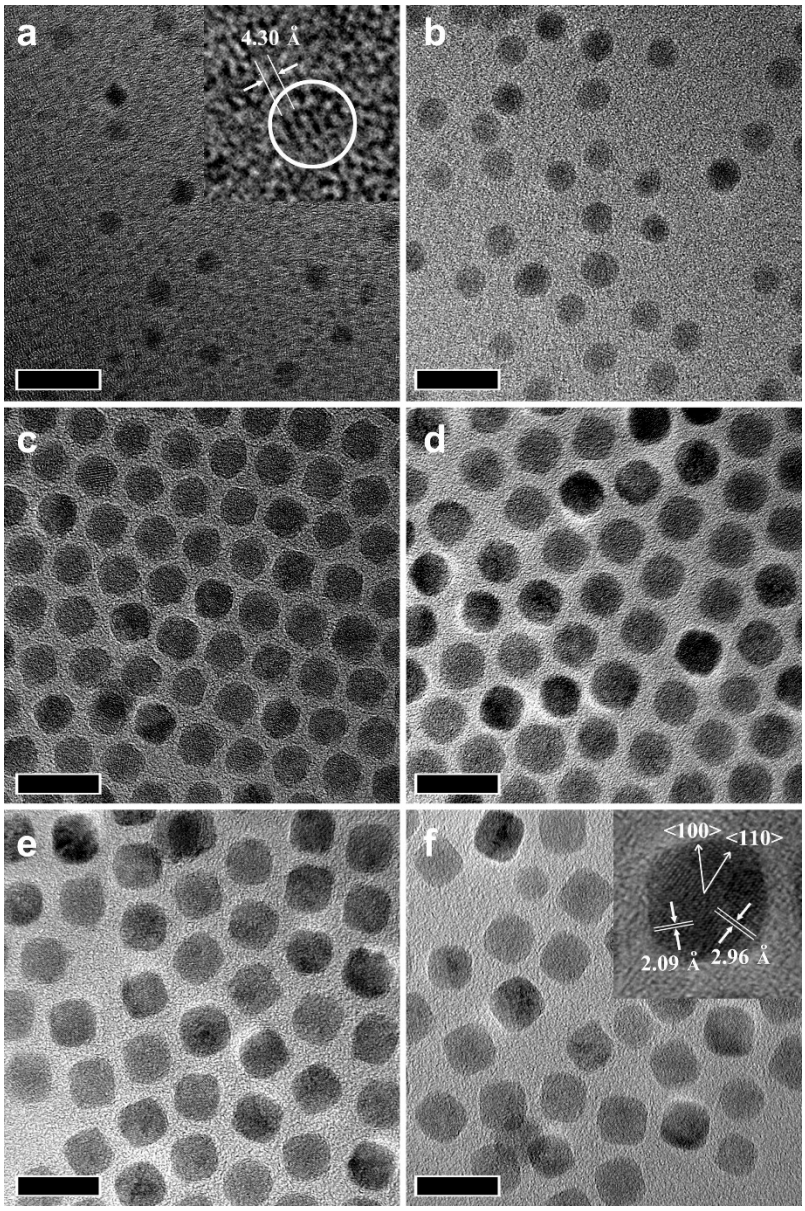

Figure 7-2. TEM images of IOOA after being aged for (a) 0 min, (b) 1 min, (c) 3 min, (d) 6 min, (e) 20 min, and (f) 1 h. All scale bars are 15 nm. Reproduced with permission from[189] , © American Chemical Society 2007)

In their 2007 paper, Hyeon et al. report the same synthetic method in producing IOOAs, yet in this paper greater aging time has shown to affect morphology, with IOOAs turning from spheres to more cubic shape, contrasting to the spherical shapes of their previous paper. To further deduce the effects of aging time, IOOAs were synthesized with varied aging times from 10 minutes to 60 minutes while holding stir rate and heat rate constant. The results are seen in **Figure 7-3**.

Unfortunately, there seemed to be no correlation between core size and aging time. And importantly, all IOOA produced were spherical in morphology; no square NPs were observed,

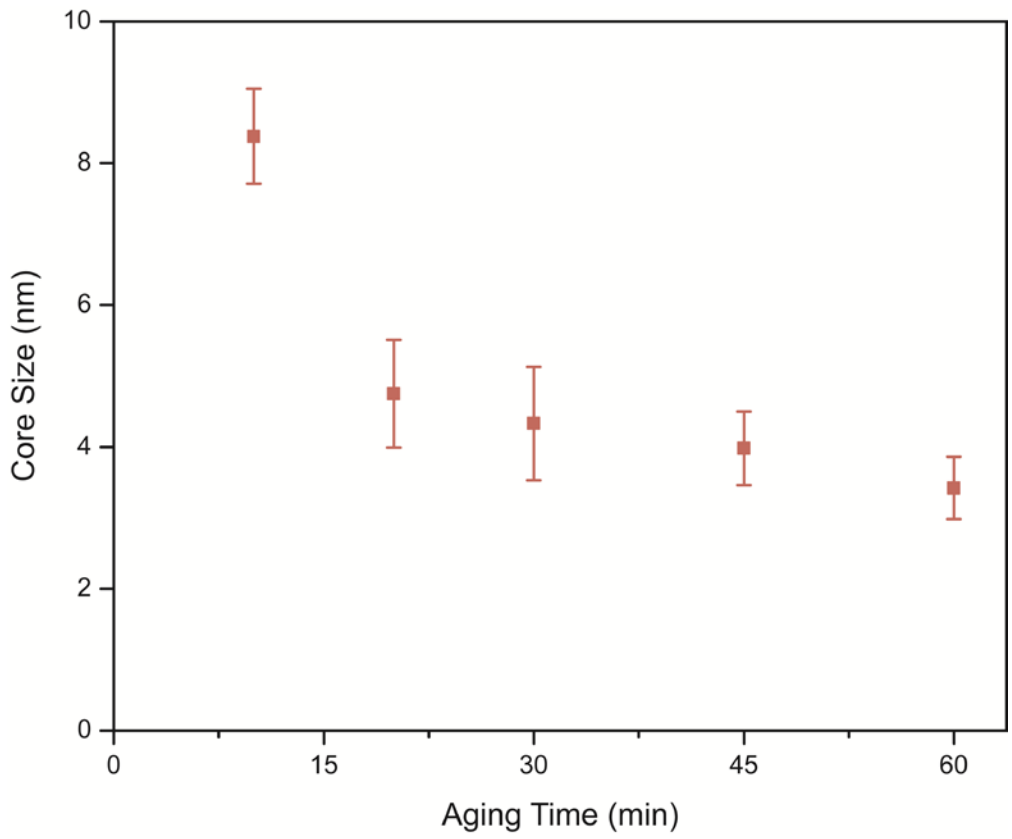

Figure 7-3. Effects of aging time on core size. No noticeable correlation was found between aging time and core size.

even past 20 minutes as reported. However, what was significant is the amount of NPs produced after aging for 10 minutes. It was significantly less, suggesting an aging time of 30 minutes should be maintained to ensure high yield. However, no relationship between aging time and size can be inferred from this study, and it does not further clarify our understanding of nucleation and growth mechanisms as it pertains to NP synthesis. As stated previously, many factors are often neglected, including stir rate.

7.3.3 Effect of stir rate

Stir rate is a factor that is not reported in most methods sections in NP synthesis papers, but it could have a large impact on synthesis by affecting the temperature homogeneity in the reaction. Therefore, we varied stir rate during the IOOA process to assess its effect on core size. The results can be seen in **Figure 7-4**.

Although no correlation between core size and stir rate is evident from the data, some significant deductions can be made. In the 62 syntheses done, >8 nm IOOAs were only produced at stir rates less than 300 rpm. Meanwhile, smaller ~4 nm IOOAs were produced at faster stir rates. There is no linear relationship between core size and stir rate, but the stir rate does seem to have an impact on whether the IOOAs are in the smaller range of 4–5 nm, or the larger 8 nm. This finding is very significant as discussed in Chapter 4; core size impacts whether or not IONPs can function as either T_2 or T_1 contrast agents. IONPs with core sizes smaller than 5 nm can potentially act as T_1 contrast agents, so this is an important discovery.

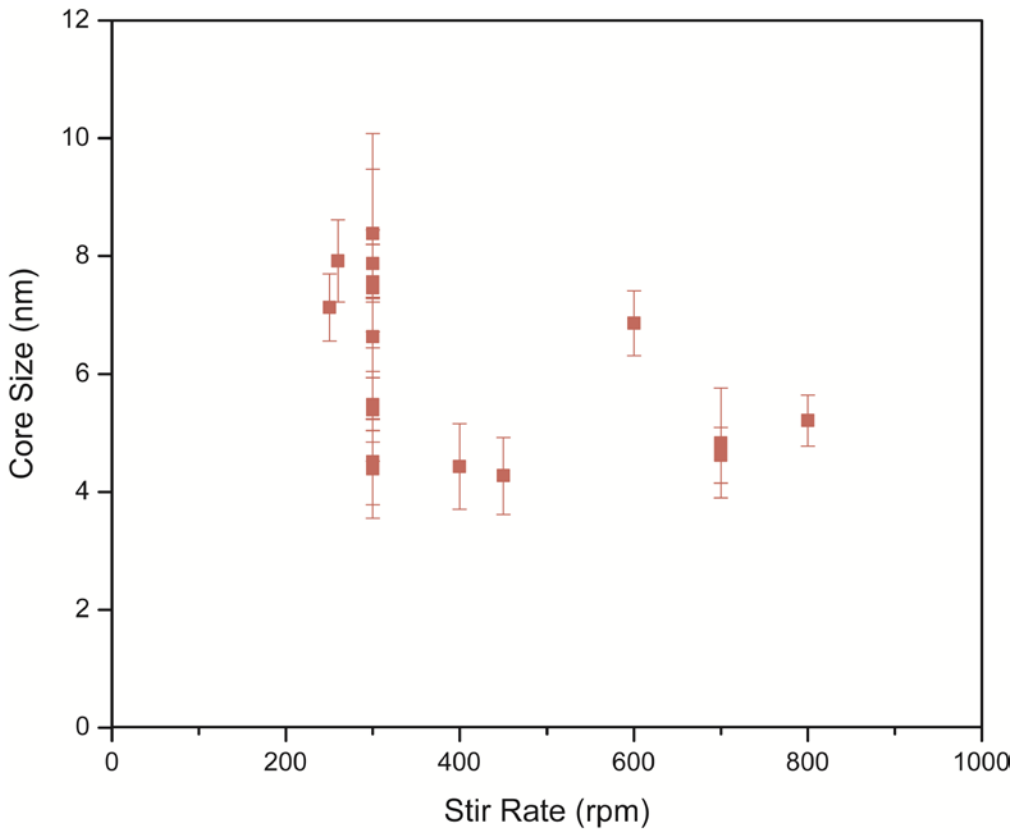

Figure 7-4. Effects of stir rate on core size. Although no noticeable correlation was found between stir rate and core size, larger (>8 nm) particles were synthesized only when the stir rate was slow (<300 nm).

When the stir rate is fast, it is possible that growth is prohibited as the monomers need time to bind to the nucleated particles in order to grow. However, with the stir rate mixing the solution continuously, it is possible that many monomers do not get the opportunity to grow, and go onto nucleating on their own, hence producing smaller sized particles. When the stir rate is slower, monomers can bind to other nucleation sites and promote growth to produce larger sized particles. Using this knowledge, 4 nm IOOA were developed and evaluated for their potential use as T_1 contrast agent.

7.3.4 Optimization of the coating step

Previous application of IONPs with 8 nm core diameters have been used as T_2 contrast agents. These IONPs were made water-soluble via a ligand exchange with silane-PEG following previous methods.[23] However, with the newly developed 4-nm IOOA, ligand exchange with silane-PEG was not successful. As the 4-nm core possesses much higher surface energy than an 8-nm core, it is possible that the amount of silane required is too saturated, causing the silane to crosslink and aggregate particles. Therefore, we developed a new method in coating 4-nm IOOA.

Phosphine oxide groups have demonstrated great binding affinity to iron oxide cores, and methods have been developed to produce phosphine oxide-terminal PEG. A schematic of the modified synthesis can be seen in **Figure 7-5**. With the successful synthesis of m-PEG-PO (methoxy-PEG-phosphine oxide), a ligand exchange was performed on 4-nm IOOAs. After numerous trials using various temperatures, concentrations, solvents, stir rates, and reaction times, we developed a successful batch of T_1 IONPs and characterized their physiological characteristics.

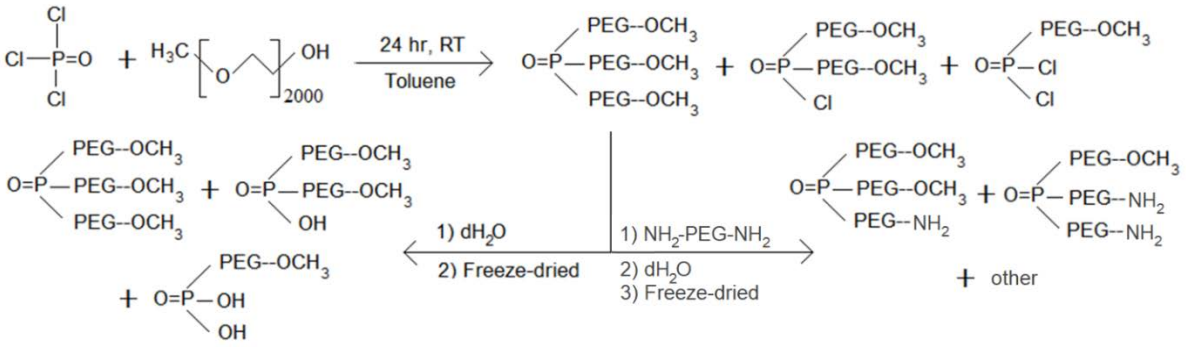

Figure 7-5. Synthesis of m-PEG-PO.

7.3.5 Characterization of T_1 IONP

Table 7-1. Physiological properties of T_1 IONP.

core size (nm)	hydrodynamic size (nm)	zeta potential (mV)	r_2 (sec^{-1} mM^{-1})	r_1 (sec^{-1} mM^{-1})	r_2/r_1
3.86 ± 0.27	21.7 ± 0.93	-4.02 ± 5.9	4.04 ± 0.61	0.73 ± 0.04	5.5

The physiological properties of T_1 IONP are summarized in **Table 7-1**. The core and morphology were evaluated via TEM (images in **Figure 7-6a).** The core size averaged 3.86 ± 0.27 in diameter and was spherical. The canting effect is dominant at this core size, demonstrating great potential as a T_1 contrast agent.[30] Using dynamic light scattering (DLS), we measured hydrodynamic size, averaging 21.7 ± 0.93 nm in PBS. The hydrodynamic distribution can be seen in **Figure 7-6b**. The size falls within the ideal 10–100 nm range, minimizing NP clearance by the kidneys and opsonization.[64] The long-term stability was determined in cell culture media over two weeks, seen in **Figure 7-6d**. Over two weeks, the T_1 IONP grew to ~40 nm, which is still within the ideal range for most biological applications, demonstrating great potential as a T_1 contrast agent. Also using DLS, we measurd the zeta potential of the particles to be -4.02 ± 5.9 mV, nearly neutral, and ideal for minimizing off-target interaction with extracellular matrices.[184] The zeta potential distribution can be seen in **Figure 7-6c**. T_1 IONP showed promising properties for biological applications.

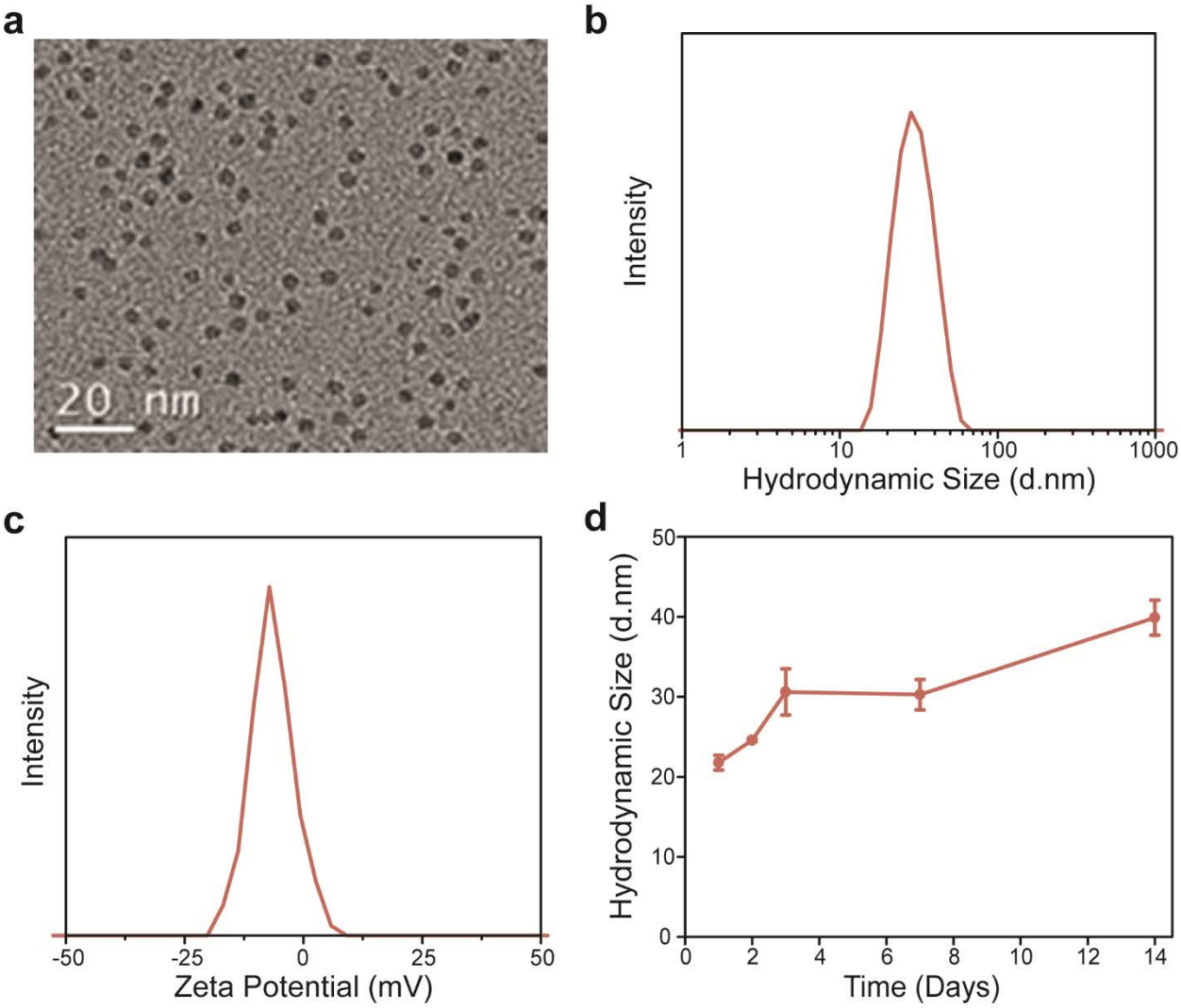

Figure 7-6. Physiological properties of T_1 IONP. (a) TEM image of T_1 IONP core. (b) Hydrodynamic size distribution of T_1 IONP in PBS. (c) Zeta potential distribution of T_1 IONP. (d) Long-term stability in cell culture media.

7.3.6 Magnetic properties of T_1 IONP

Although 4–nm iron oxide cores have been reported as potential T_1 contrast agents, the coating may affect the magnetic properties of the IONPs. Therefore, the magnetic properties had to be evaluated. The relaxivities were evaluated by phantom MRI. Figure 7-7a show the T_1 signal intensity increasing with increasing Fe concentration, demonstrating the T_1 contrast efficiency. The resulting linear plot of $1/T_1$ (R_1) and $1/T_2$ (R_2) vs. Fe concentration can be seen in

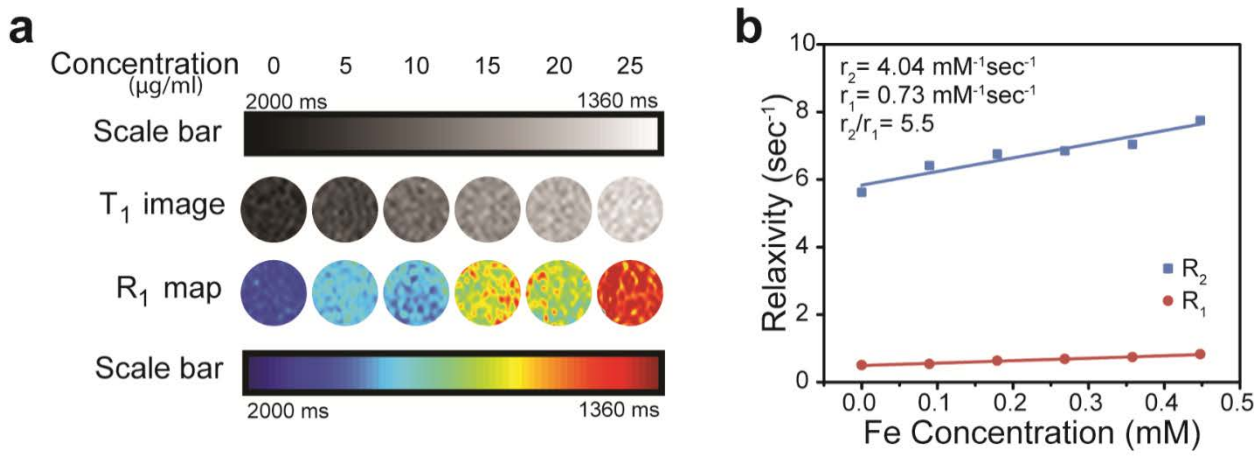

Figure 7-7. Magnetic properties of T_1 IONP. (a) T_1-weighted MR images and T_1 maps of MRI phantom images of T_1 IONP at various Fe concentrations. (b) Plot of R_2 and R_1 as a function of Fe concentration.

Figure 7-7b. The transverse relaxivity, r_2, was calculated to be 4.04 ± 0.61 s^{-1} mM^{-1}, while the longitudinal relaxivity, r_1, was calculated to be 0.73 ± 0.04 s^{-1} mM^{-1}. This calculates to an r_2/r_1 ratio of 5.5, a promising value for a T_1 contrast agent.[30]

7.3.7 Cell viability of T_1 IONP

For T_1 IONPs to be used for biological applications, they must be non-cytotoxic. Three glioblastoma cell lines: U87, SF767, and U118, were chosen to test T_1 IONPs for their cytotoxicity. As seen in **Figure 7-8**, the three cell lines displayed high viability after 24-hour incubation with T_1 IONPs. Starting at 100 μg/mL, T_1 IONP begins to show some toxicity; however, that high concentration is unlikely to be maintained for 24 hours. This study highlights the biocompatibility of T_1 IONP on three different glioblastoma cell lines.

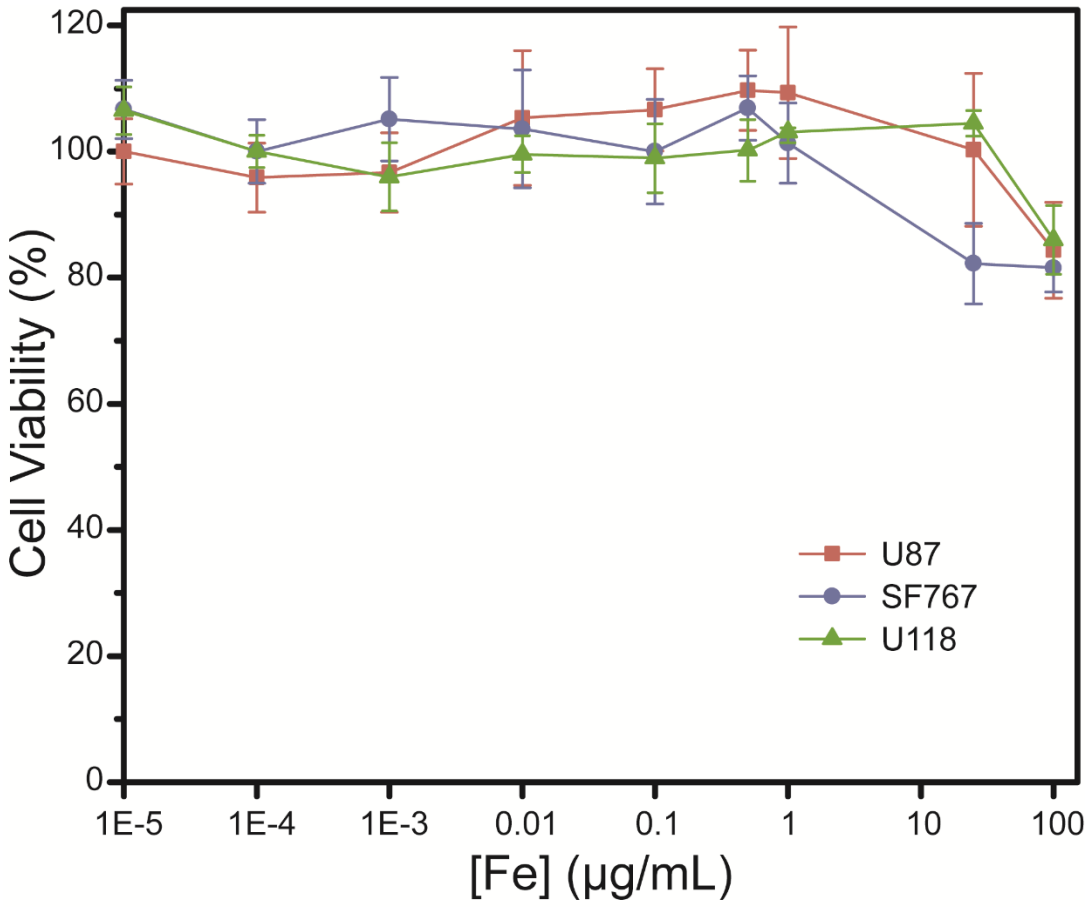

Figure 7-8. Cell viability of T_1 IONP. Three glioblastoma cell lines — U87 (red), SF767 (blue), and U118 (green) — were incubated with T_1 IONP for 24 hours at 37 °C.

7.4 Conclusions

We further investigated the thermal decomposition method by exploring the effects of aging time, heating rate, and stir rate on core size. Using this knowledge, we synthesized 4-nm IONP as a potential T_1 contrast agent. We measured and characterized its physiological properties, and confirmed its T_1 capabilities via phantom MRI. T_1 IONP demonstrated great biocompatibility on various cell lines, and minimal toxicity in cytotoxicity studies.

8. Evaluating the effects of cryoprotection for long-term storage of superparamagnetic iron oxide nanoparticles

One limitation to clinical applications of superparamagnetic iron oxide nanoparticles (SPIONs) is their poor shelf-life due to high surface energy. Currently, most SPION-based systems are stored in aqueous solutions, which are inadequate because of physical and chemical instability caused by water: loaded drugs may leak and SPIONs may oxidize and degrade, reducing efficacy and adversely affecting magnetic properties. Freeze-drying circumvents the instability caused by water, but this process causes its own stresses resulting in aggregation and fusion of nanoparticles (NPs). Here we evaluate common cryoprotectants on their ability to minimize stresses caused by freeze-drying in two types of SPION: one developed by our group and one commercially available from Sigma-Aldrich. Both NPs were initially evaluated for size, stability, and magnetic relaxivity, then freeze-dried with and without five cryoprotectants: glucose, sucrose, dextrose, mannitol, and sorbitol. Sucrose was the most effective while mannitol was the least effective at stabilizing NPs during the freeze drying process. NPs freeze-dried with 10 wt.% sucrose maintained size, stability, and magnetic properties when stored for up to 6 months at –20 °C. This demonstrates an effective long-term storage method for SPIONs, removing an obstacle to their application in a clinical setting.

8.1 Introduction

Magnetic NPs have received significant attention in the biomedical field due to their unique intrinsic properties at the nanoscale with a wide range of possible applications. Superparamagnetic iron oxide nanoparticles (SPIONs), in particular, have been explored for potential use in targeted drug delivery, molecular imaging, and biosensor applications. They

exhibit intrinsic magnetic properties, biocompatibility, biodegradability, and flexible surface chemistry, and have proven to be effective MRI contrast agents.[1,10,16,25,190]

However, SPIONs, along with many NP systems, must be water soluble for clinical applications, thus are typically kept in aqueous solutions, which severely limits their storage life. Although NPs may be stabilized initially during the synthesis, aggregation and settling are common after an extended time due to the high surface energy and small size of NPs.[191] Additionally, over time, water degrades NP systems and can affect intrinsic properties; loaded drugs can leak, and eventually, NP systems may hydrolyze.[192-194] Loss of drugs can lead to off-target side effects reducing specificity and efficacy over time. SPIONs also may lose their MR contrast capabilities due to aggregation.[103,195] Due to the physical and chemical instability, only freshly prepared NPs can be used, severely limiting their practical application.

To improve the lifetime of NP systems for greater clinical utility, freeze-drying, or lyophilization, has been used as a technique to remove the water in these systems. Removing water can solve many of the problems of NP storage, but freeze-drying causes stress that can result in irreversible damage to NP systems.[196-199] During the freezing step of lyophilization, a phase separation occurs, producing ice and a super-saturated solution. Supersaturation of SPIONs can cause aggregation and fusion of NPs due to their instability at high concentrations; supersaturation of salts from buffers has further deleterious effects.[196,200,201] Aggregation of SPIONs may adversely affect magnetic properties and lead to rapid clearance from the body.[103,195,196] Cryoprotectants can prevent or minimize stresses during the freezing step. Common cryoprotectants are sugar or sugar alcohol variants: glucose, sucrose, dextrose, mannitol, and sorbitol. At low temperatures, these sugar molecules vitrify, turning into a glassy

matrix. Within this glassy matrix, NPs are immobilized, preventing NPs from aggregating or fusing.[202,203]

Freeze-drying is predominantly used with polymeric NPs,[196] and cryoprotectants have been used to develop long-term stability, even withstanding extreme conditions such as high temperature and humidity.[204] Freeze-drying with cryoprotectants prevents aggregation, degradation, and drug leakage. It has also been used to transform polymeric NPs into a solid dosage for different administration routes (oral, nasal, pulmonary, etc.).[204]

Despite the benefits, freeze-drying magnetic NPs has largely been overlooked, with few studies done on SPIONs. The role of cryoprotectants to stabilize SPIONs has not yet been explored, and whether cryoprotectants help retain the original properties of SPIONs remains unknown. Here we evaluated the role of cryoprotectants on two types of iron oxide NPs: a commercially available iron oxide NP (CANP), and IOSPM produced by our lab. IOSPM is an iron oxide nanoparticle coated in a siloxane-PEG-monolayer, and has demonstrated excellent biological stability and a myriad of applications.[23,205-210] Both NPs consist of a ~10 nm iron oxide core coated with polyethylene glycol. Transmission electron microscopy (TEM) was used to determine core size and morphology, while we used dynamic light scattering (DLS) to determine hydrodynamic size distribution, zeta potential, and stability of NPs. Phantom MRI determined the relaxivities of the NPs. We then used five cryoprotectants to freeze-dry NPs, and evaluated the efficacy of cryoprotectants in retaining the original properties of the NPs.

8.2 Experimental

8.2.1 Materials

All chemicals were purchased from Sigma-Aldrich (St. Louis, MO, USA) unless otherwise specified.

8.2.2 NP synthesis, freeze-drying, and storage

CANPs were purchased from Sigma-Aldrich and used as is.

IOSPMs were synthesized via the following: ~10 nm oleic-acid coated iron oxide NPs were formed by thermal decomposition of iron-oleate complex following published methods.[7] A ligand exchange used previous methods with modifications[23]: for every 50 mg Fe of oleic-acid coated iron oxide, we used 300 mg of $mPEG_{2k}$-NH_2 and 225 mg of H_2N-PEG2k-NH_2.

All NPs were kept at 1 mg Fe/ml. Samples with cryoprotectants contained 10 wt.% cryoprotectant. All samples were slow-frozen at a rate of –1 °C/min using an isopropanol bath, then flash-frozen in liquid nitrogen to ensure proper freezing. The samples were freeze-dried overnight and then redispersed into DI water at the same concentration of 1 mg Fe/mL before analysis.

Samples for longer storage were sealed with parafilm under $N_{2(g)}$ and stored in –20 °C for 1 month or 6 months. Following storage, they were redispersed into DI water at the same 1 mg Fe/mL concentration.

8.2.3 NP Characterization

The morphology and size of NPs were obtained using FEI TECNAI F20 TEM (Hillsboro, OR). Iron oxide core diameters were measured using ImageJ to obtain core size distribution, mean, and standard deviation.

We measured hydrodynamic size and zeta potential of NPs using a DTS Zetasizer Nano (Malvern Instruments, Worcestershire, UK). Hydrodynamic sizes were measured in PBS and DMEM with 10% FBS and 1% antibiotic-antimycotic at a concentration of 50 μg Fe/mL. Size measurements were taken at day 1, 2, 3, and 7. We measured Zeta potential in 20 mM HEPES (pH = 7.4) at the same concentration.

8.2.4 Phantom MR imaging

We used quantitative T_2 MR imaging scan sequences to investigate the contrast enhancing capabilities of NPs. MR imaging was conducted on Bruker Avance III 600 MHz, 14 T wide bore spectrometer. NPs in DI water were pipetted into glass vials (3.25 mm I.D., 5 mm O.D., 200 μL volume) at concentrations of 0–25 μg Fe/mL. The vials were held in place inside a water reservoir; the water served as a homogeneous background signal to minimize magnetic susceptibility variations near samples. The fixed vials were placed in a 25-mm single-channel ^{1}H radiofrequency receiving coil (PB Micro 2.5). We measured quantitative T_2 values of NPs using a multi-spin multi-echo (MSME) pulse sequence with TR = 2500 ms, TE = 6.7 + 6n ms (n = 0–16), and 78 × 156 μm^2 in-plane resolution with 0.5-mm slice thickness for 14 slices. Analysis of MR imaging data was accomplished with the FMRIB software library (FSL), Paravision 5.1 analysis package (Bruker), and ImageJ (NIH).

8.3 Results and discussion

8.3.1 Initial NP characterization

Table 8-1. Physiological properties of control NPs.

	core size (nm)	hydrodynamic size (nm)	polydispersity index	zeta potential (mV)	r_2 (sec^{-1} mM^{-1})
IOSPM	10.5 ± 0.7	29.0 ± 0.8	0.068 ± 0.007	–9.96 ± 6.6	98.2 ± 4.7
CANP	11.0 ± 0.9	73.5 ± 2.5	0.25 ± 0.003	–10.4 ± 5.9	95.5 ± 2.9

Table 8-1 summarizes basic physiological properties of CANP and IOSPM. The morphology and size of the iron oxide core were characterized via TEM (**Figure 8-1a**). For both NPs, the morphologies were spherical, with the IOSPM (**Figure 8-1a i**) averaging 10.5 ± 0.7 nm, while the CANP (**Figure 8-1a ii**) averaged 11.0 ± 0.9 nm in diameter; both fall within the size range to enable superparamagnetism. However, they differed in hydrodynamic size, as measured using dynamic light scattering (DLS). IOSPMs averaged 29.0 ± 0.8 nm while CANPs averaged 73.5 ± 2.5 nm. Hydrodynamic size influences NP interaction with physiological and cellular barriers. NPs larger than ~100 nm are cleared from the body by the mononuclear phagocyte system (MPS), while NPs smaller than ~10 nm undergo rapid renal clearance, hence the optimal range for prolonged circulation in the body falls between ~10–100 nm.[64] The NPs' long-term stability was determined in cell culture media (**Figure 8-1d**). IOSPMs showed minimal growth in cell culture media, plateauing at 32.7 nm after 7 days. However, the CANPs showed immediate growth, increasing to 118.4 nm after 7 days. Due to their large size, the CANPs are susceptible to being cleared by the MPS.

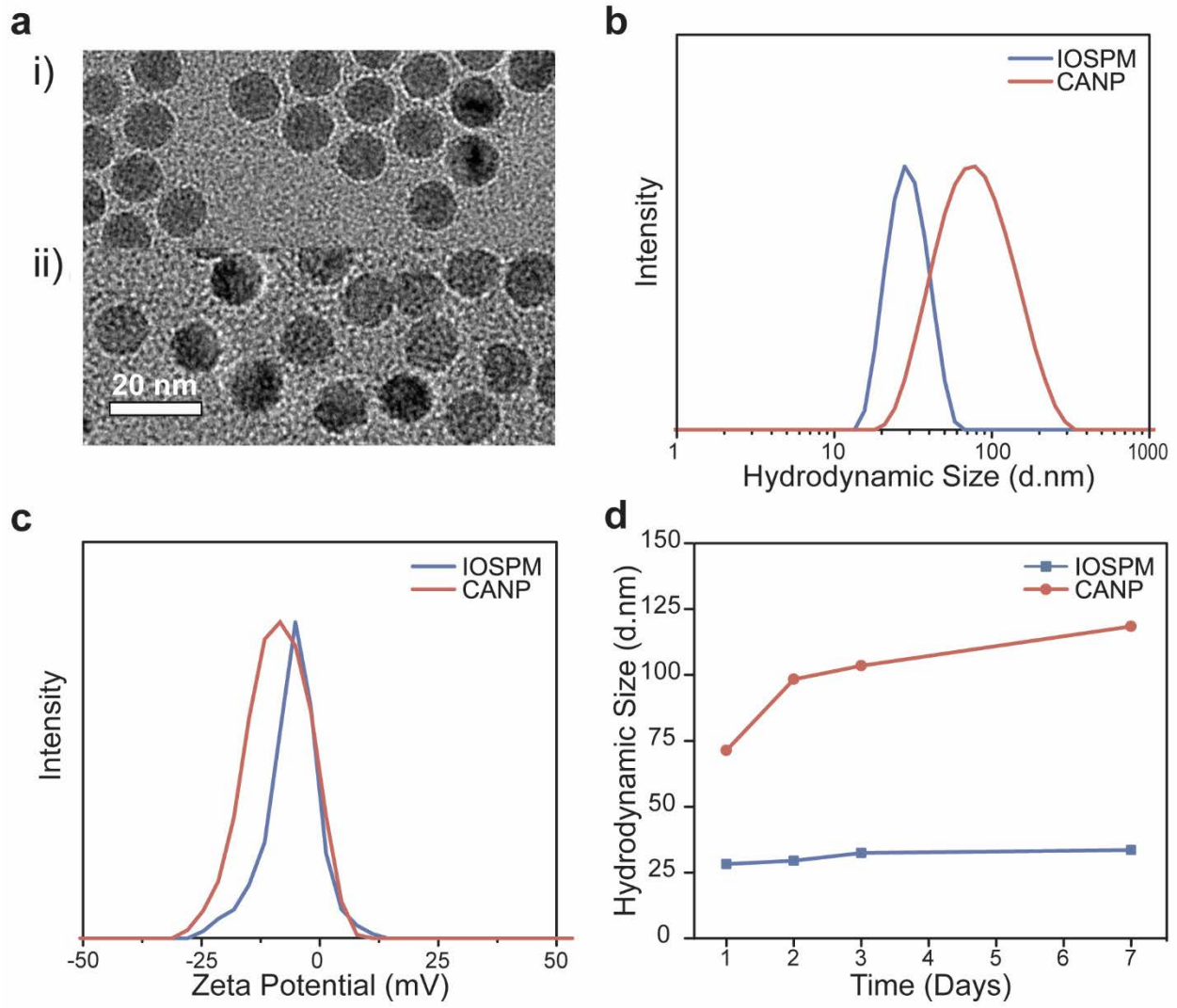

Figure 8-1. Physiological properties of IOSPM and CANPs. (a) TEM images of (i) IOSPM and (ii) CANP. (b) Hydrodynamic size distribution, (c) Zeta potential distribution of IOSPM (blue) and CANP (red). (d) Hydrodynamic sizes of IOSPM (blue) and CANP (red) in cell culture media at 37 °C as a function of time for a period of 1 week.

Zeta potential has a strong influence on NPs' interaction with the extracellular matrix, which could lead to nonspecific uptake. Strongly positively charged surfaces can lead to nonspecific interactions with negatively charged cell membranes, and negatively charged surfaces can lead to nonspecific interactions with positively charged extracellular matrices.[184] **Figure 8-1c** show the zeta potential distribution of NPs. IOSPM measured –9.96 ± 6.6 mV while

CANP measured –10.4 ± 5.9 mV. Both were slightly negative, ideal for minimizing electrostatic interaction with the extracellular matrix.[184]

SPIONs have demonstrated utility as MRI contrast agents, and several formulations have already been approved by the Food and Drug Administration (FDA). Specifically, SPIONs are typically used as T_2 contrast agents (negative contrast agent), which increase contrast by decreasing signal with concentration. The efficacy of T_2 contrast agents is dependent on their transverse relaxivity, r_2, which is determined by measuring the signal intensity at a range of concentrations. The relaxivities of NPs were evaluated by phantom MRI. **Figure 8-2a** shows the T_2 signal intensity decreasing (thus greater negative contrast) with increasing Fe concentration for NPs. The resulting linear plot of $1/T_2$ (R_2) vs. Fe concentration can be seen in **Figure 8-2b**. The transverse relaxivity, r_2, (slope of the curve) was calculated to be 98.2 ± 4.7 s^{-1} mM^{-1} and

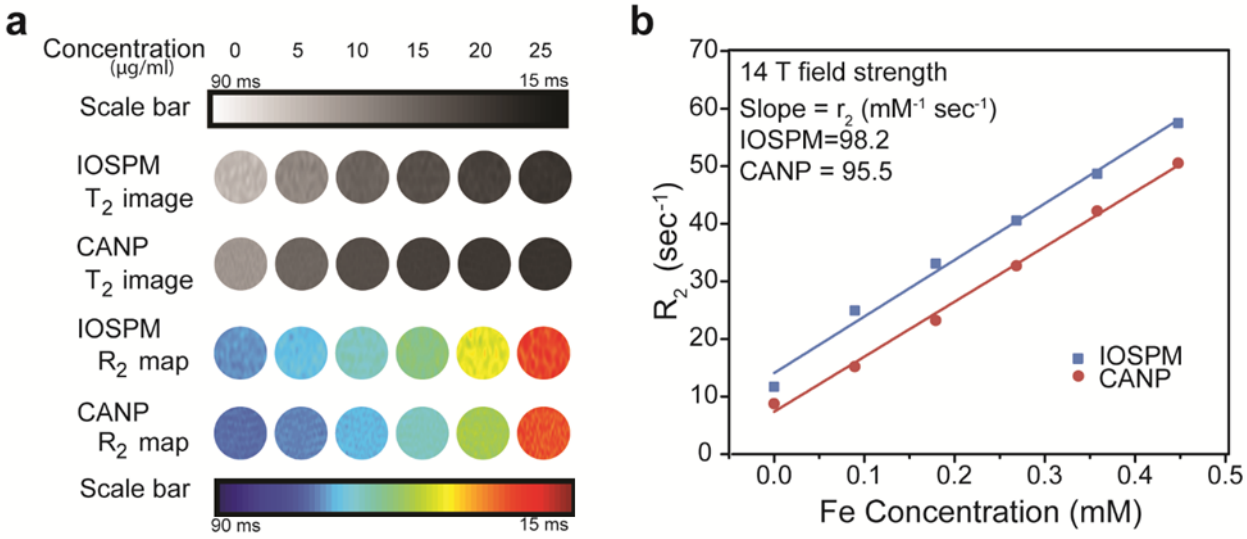

Figure 8-2. Magnetic properties of IOSPM and CANP. (a) T_2-weighted MR images and R_2 maps of phantom MRI images of IOSPM and CANP at Fe concentrations from 0–25 μg/ml. (b) Plot of R_2 vs. Fe concentrations in mM. The slope of the fitted linear line equates to the specific relaxivity of r_2.

95.5 ± 2.9 s^{-1} mM^{-1} for IOSPM and CANP, respectively, at 14 T field strength. Overall, the NPs are quite similar in properties apart from hydrodynamic size and stability.

8.3.2 Stability after freeze-drying

NPs were subjected to freeze-drying with five different cryoprotectants: glucose, sucrose, dextrose, mannitol, and sorbitol, as well as one without any cryoprotectants, and were measured for hydrodynamic size and stability in cell culture media.

All samples were created at the same concentration (1 mg Fe/ml with 10 wt.% cryoprotectant). The samples were slow-frozen at a rate of –1 °C/min before being freeze-dried. In our preliminary experiments, samples that were flash-frozen gave inconsistent results, likely because uneven exposure to liquid nitrogen caused non-uniform freezing. As this project involved a large number of samples, we deemed slow-freezing optimal for consistent results. The samples were left on the lyophilizer overnight before being redispersed into DI water at the initial concentration. We analyzed the samples for their hydrodynamic size distribution, and monitored their stability in cell culture media (**Figure 8-3**). **Figure 8-3a** shows the average hydrodynamic size of the IOSPMs in DI. The control refers to their initial NP size in solution, which was measured to be 29.0 ± 0.8 nm. Compared to the control, the freeze-dried sample without any cryoprotectant nearly doubled in size to 52.6 ± 4.1 nm. The cryoprotectants inhibited this growth, with sucrose showing the most minimal growth at 37.6 ± 0.7 nm, and sorbitol proving least effective at 54.1 ± 1.8 nm. **Figure 8-3c** show the NPs' stability in cell culture media, with sucrose the most effective and mannitol the least effective at preserving stability. Overall, all NPs show minimal growth, maintaining their initial sizes, showing that even when freeze-dried, IOSPMs are quite stable.

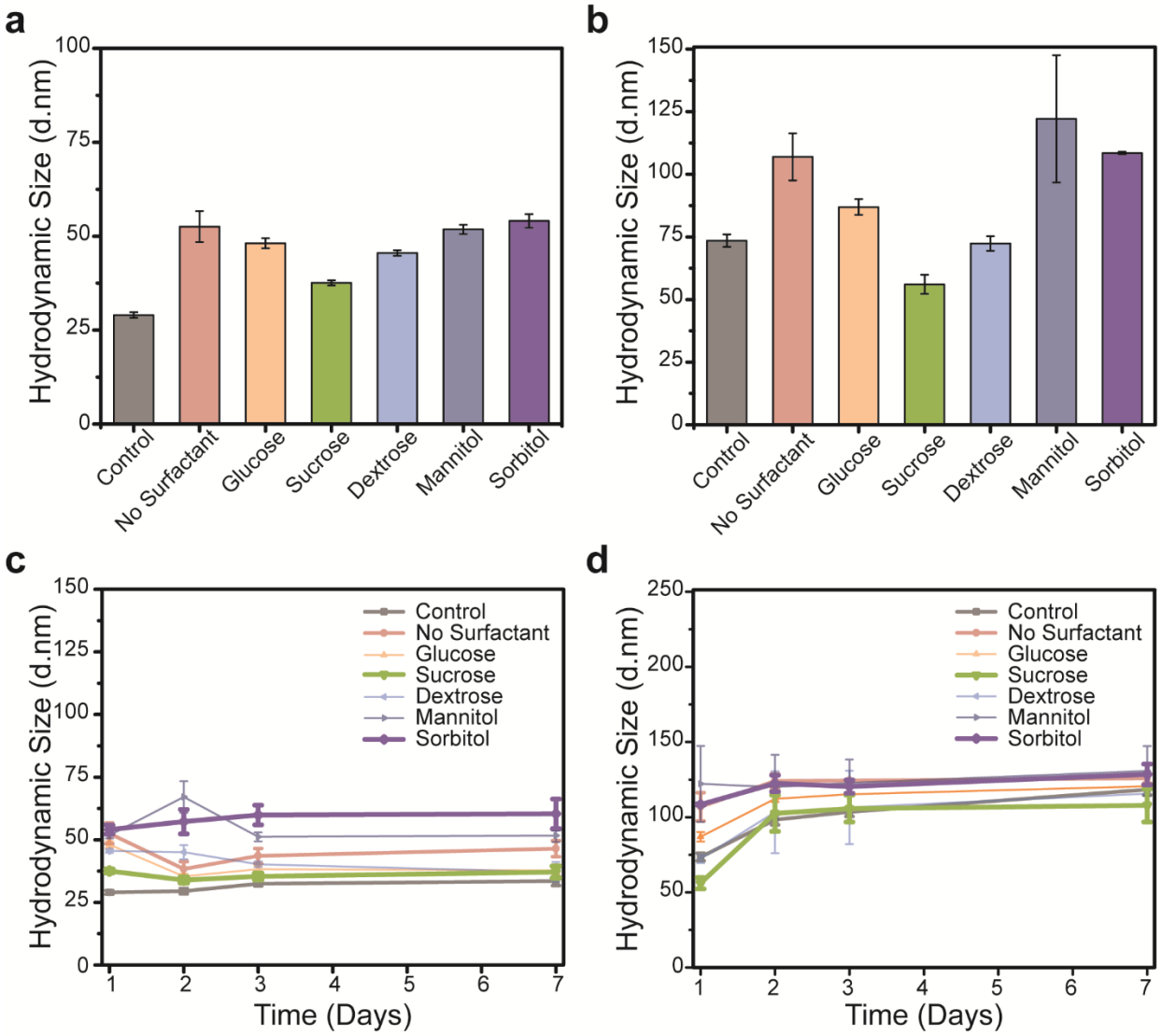

Figure 8-3. Size and stability after freeze-drying (a-b). Hydrodynamic size of control (a) IOSPM and (b) CANP in comparison to freeze-dried nanoparticles with cryoprotectants, and without (c-d). Stability of all (c) IOSPM and (d) CANP in cell culture over 7 days. The most effective cryoprotectant, sucrose (green), and least effective cryoprotectant, sorbitol (purple), are highlighted.

Similar results were observed with CANPs (**Figure 8-3b,d**). Without any cryoprotectants, the CANP increased in size to 107.0 ± 9.4 nm, compared to the control size of 73.5 ± 2.5 nm. However, sucrose decreased the NP size to a smaller diameter of 56.1 ± 3.8 nm, which could indicate sucrose promotes denser PEG packing. At the other extreme, sorbitol proved worse than no cryoprotectant at all at preventing aggregation, with NP size increasing to 120.6 ± 7.3 nm.

Without any cryoprotectants and when using sorbitol as cryoprotectants, CANPs fall out of the desired range of 10–100 nm, meaning the NPs are more likely to be cleared by the MPS. Additionally, as SPIONs are often used as carriers for targeted drug delivery, loading hydrophobic drugs and conjugating targeting ligands are likely to increase the size even further, increasing their susceptibility to undesired clearance from the body. This effect demonstrates the utility of sucrose, as it helped maintain the initial size and stability of the NP, while sorbitol increased the NPs' size and negatively impacted the long-term stability. As sucrose and sorbitol proved to be the most effective and least effective cryoprotectant, they were selected for further testing to determine the effects of cryoprotectants over time.

8.3.3 Stability after freeze-drying and 1 month storage

To facilitate clinical application, the freeze-dried NPs must survive typical storage conditions. After freeze-drying with and without cryoprotectants, the samples were stored under $N_{2(g)}$ and kept in –20 °C, storage conditions that are readily achievable in most clinical settings. The NPs were stored for one month and their hydrodynamic size and stability in cell culture media were monitored.

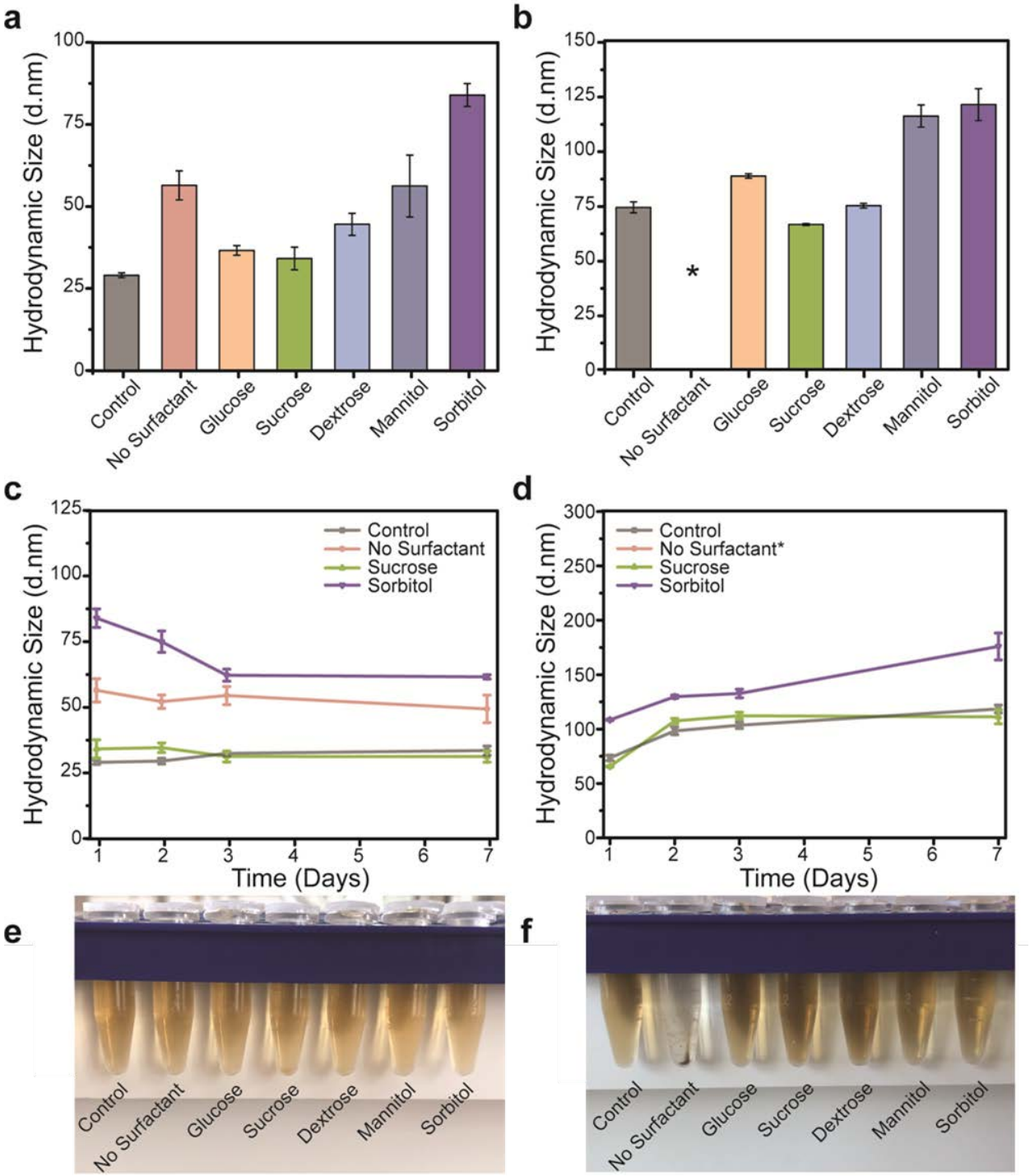

Figure 8-4. Size and stability after freeze-drying and 1 month storage. (a-b): Hydrodynamic size of control (a) IOSPM and (b) CANP in comparison to freeze-dried nanoparticles with cryprotectants, and without. (c-d): Stability of (c) IOSPM and (d) CANP in cell culture over a course of 7 days. (e-f): Corresponding photo of the tested samples of (e) IOSPM and (f) CANP. (* CANP without surfactants was no longer water soluble after freeze-drying and 1 month storage, hence no data could be recorded.)

Figure 8-4a shows the average hydrodynamic size of the IOSPMs in DI water after one month of storage. The trends that were observed prior to storage are still apparent. IOSPMs without any cryoprotectant grew to 56.4 ± 4.4 nm. IOSPMs protected with sucrose showed the greatest benefit with size 34.1 ± 3.5 nm, while sorbitol showed little to no benefit. **Figure 8-4c** shows the NPs' stability in cell culture media, and it is evident that sucrose is effective enough to keep the stability the same as the initial NP, while sorbitol negatively affected stability. Overall, the results after 1 month storage showed minor differences from the results without storage, demonstrating the promise of cryoprotectants in prolonging the lifetime of these SPIONs.

Figure 8-4b,d show the size and stability results of freeze-dried CANPs after one month of storage. Without any cryoprotectants, the CANPs degraded to such an extent that they could not be redispersed into water, seen in **Figure 8-4e,f**. Therefore, no accurate hydrodynamic size could be determined. However, the benefits of sucrose are clearly evident, as the size was 65.7 ± 0.4 nm, smaller than the initial size of 73.5 ± 2.5 nm. Sorbitol again had failed to maintain the initial size, with CANPs growing to 120.6 ± 7.2 nm. The benefits of cryoprotectants in the freeze-drying process are much more apparent with CANPs, where both cryoprotectants tested allowed the NPs to redisperse, as CANPs without any surfactants were no longer water soluble. Sucrose, again, showed the most benefit in maintaining the initial size and stability of freeze-dried NPs.

8.3.4 Stability after freeze-drying and 6 months storage

Having demonstrated the ability of certain cryoprotectants to preserve NPs after 1 month of storage, we extended the storage time to 6 months, to determine their efficacy over a longer period.

Figures 8-5a,c show the average size and stability of IOSPMs after being freeze-dried and stored for 6 months. Even after 6 months, very little growth was seen. Without any cryoprotectants, IOSPMs grew to 58.4 ± 8.5 nm, which is approximately double the control NP. This is comparable to the size after 1 month, indicating that the additional 5 months of storage had little impact on the NPs. Similarly, the effects of sucrose at maintaining size are clear over this longer duration; at 38.74 ± 1.9 nm, NPs stored with sucrose showed no significant increase from their size at 1 month. However, the negative effects of sorbitol were again evident, as sorbitol increased the NPs' size to 111.0 ± 4.4 nm, much worse than the size after 1 month, indicating sorbitol does not preserve NP size over time.

The size and stability results of freeze-dried CANPs after six months of storage can be seen in **Figures 5b,d**. As expected, the sample without any cryoprotectants would not dissolve into DI water (**Figures 5e-f**). Therefore, no hydrodynamic size or stability could be determined. Yet again, sucrose showed the best size and stability, maintaining NP size similar to the control, even after 6 months of storage post freeze-drying. Sorbitol was not effective at maintaining initial size and stability, with NPs being larger than 150 nm after 6 months of storage. Although sorbitol kept the NPs water soluble, size greater than 150 nm increases the likelihood of the NPs being cleared, hence should likely be avoided when preserving NPs for extended periods.

From these experiments, it is evident that sucrose maintains NP size and stability even after freeze-drying and up to 6 months of storage. Sorbitol, while helping CANPs redisperse into water, did not maintain the initial size. Of the five cryoprotectants tested, sucrose showed the most consistent and best results in maintaining the initial size and stability of the NPs, while sorbitol was the least effective.

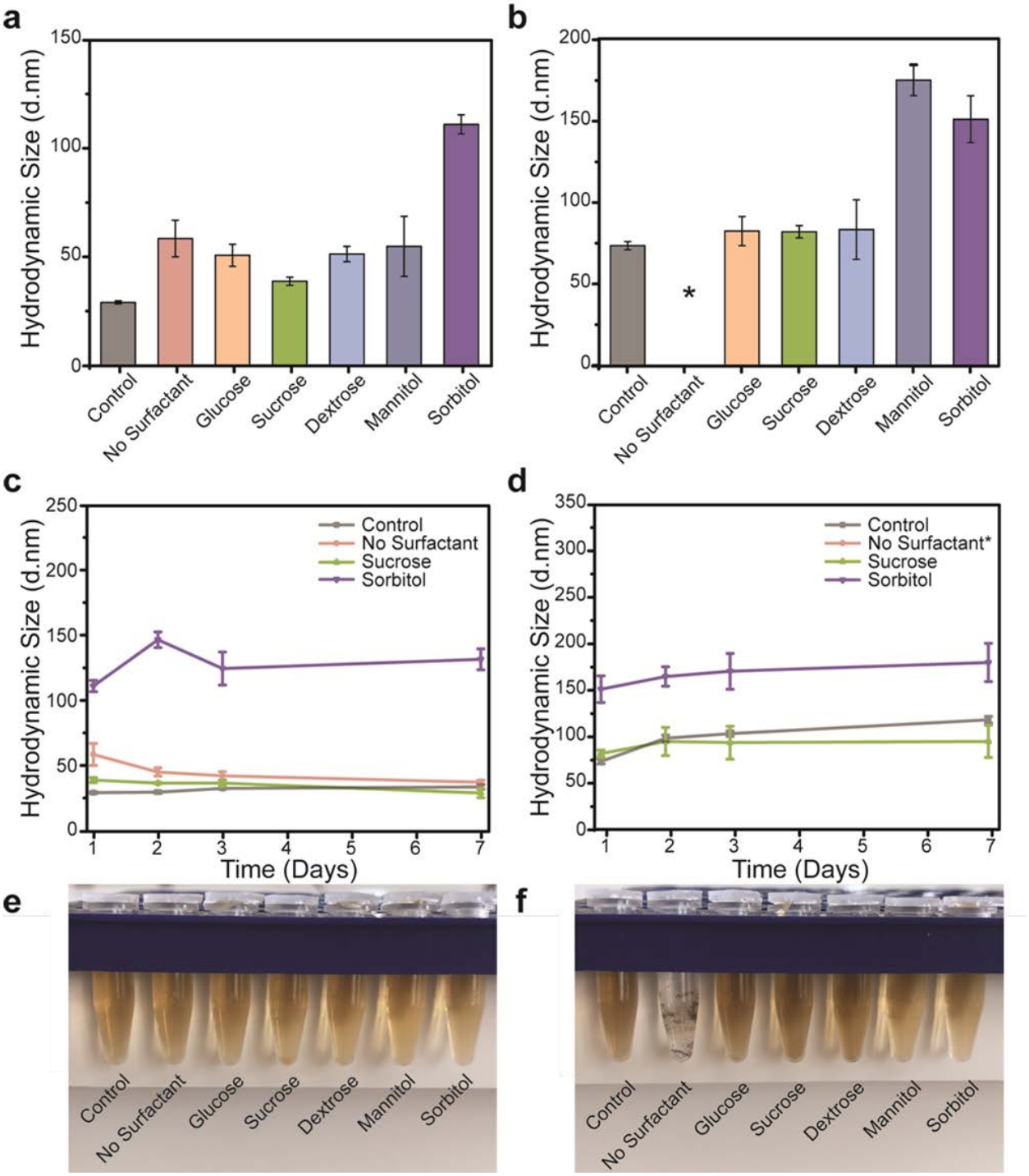

Figure 8-5. Size and stability after freeze-drying and 6-month storage. (a-b): Hydrodynamic size of control (a) IOSPM and (b) CANP in comparison to freeze-dried nanoparticles with cryprotectants, and without. (c-d): Stability of (c) IOSPM and (d) CANP in cell culture over a course of 7 days. Most effective cryoprotectant, sucrose (green), and least effective cryoprotectant, sorbitol (purple) are highlighted. (e-f): Corresponding photo of the tested samples of (e) IOSPM and (f) CANP. (* CANP without surfactants was no longer water soluble after freeze-drying and 1 month storage, hence no data could be recorded.)

8.3.5 Zeta potential after freeze-drying and 6 months storage

Though initial size and stability were maintained using sucrose as a cryoprotectant, zeta potential could have been impacted from freeze-drying and 6 months storage. NPs may have changed in size and morphology, and such alterations to the surface could affect zeta potential. Therefore, given its significant influence on NP interaction with extracellular matrix, it was important to measure zeta potential to see if any significant changes occurred.

Zeta potential of freeze-dried NPs without any cryoprotectants, with sucrose, and with sorbitol, after 6 months of storage were measured using DLS (with the exception of CANP without any cryoprotectants; as previously described, long-term storage led to poor solubility in water, hence CANP samples without cryoprotectants were measured right after freeze-drying without storage). The zeta potential distributions of NPs can be seen in **Figure 8-6**, with values tabulated in **Table 8-2**. There is no significant change with the zeta potential of all NP samples.

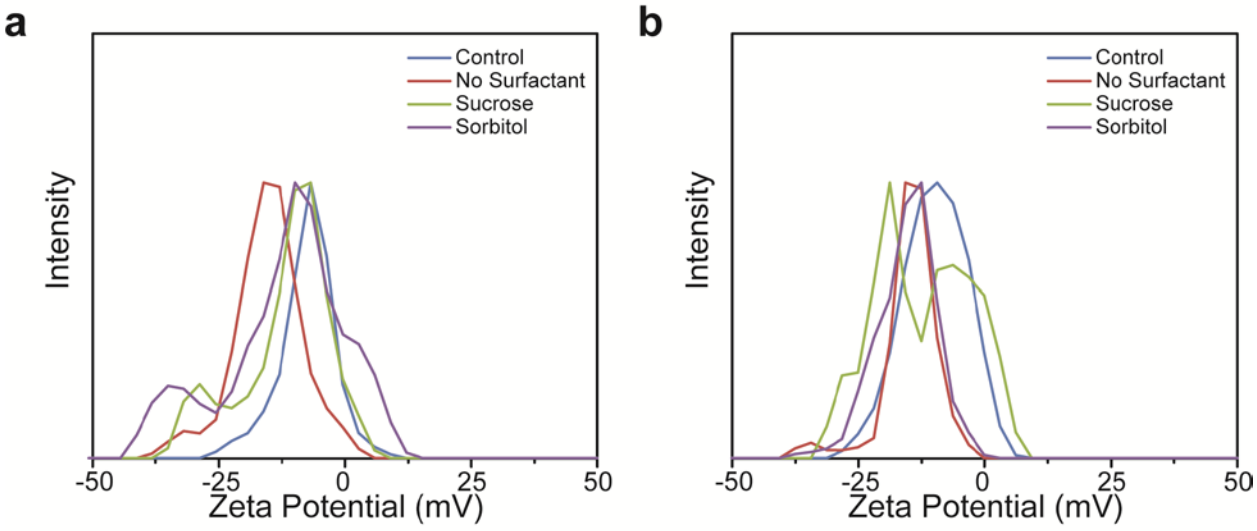

Figure 8-6. Zeta potential after freeze-drying and 6-month storage. (a-b): Zeta potential distributions of various (a) IOSPM and (b) CANP.

Table 8-2. Zeta potential value (mV) of NPs evaluated by DLS after freeze-drying and 6 month storage

	Control	No Cryoprotectant	Sucrose	Sorbitol
IOSPM	–9.96 ± 6.6	–12.9 ± 7.2	–10.3 ± 9.3	–10.8 ± 12.3
CANP	–10.4 ± 5.9	–13.5 ± 5.8	–11.9 ± 9.8	–13.2 ± 6.1

This is likely because NP aggregation does not in and of itself alter surface charge, which is an added benefit in freeze-drying NPs for long-term storage. NPs stored in aqueous solutions have shown changes in zeta potential over time, which could lead to nonspecific uptake and clearance from the body. [211]

8.3.6 Magnetic properties after freeze-drying and 6 months storage

From previous results, it was evident that sucrose was the best cryoprotectant at maintaining the initial size and stability of the NPs, while sorbitol was the least effective. However, as SPIONs are already used clinically as imaging contrast agents[212], maintaining the initial magnetic properties is another priority. While sucrose is able to maintain size, stability, and zeta potential of both NPs after 6 months of storage, the magnetic properties may be altered by oxidation even without a change in NP size. Therefore, NPs were analyzed for their magnetic properties via phantom MRI after freeze-drying and 6 months storage, to ensure the NPs can still function as MRI contrast agents.

Freeze-dried CANP and IOSPM were evaluated without any cryoprotectants, with sucrose, and with sorbitol, after 6 months of storage (with the exception of CANP without any cryoprotectants; as before, CANP samples without cryoprotectants were measured right after freeze-drying without storage due to their poor long-term stability). T_2 signal intensity (in grayscale and colormap) vs. Fe concentration of the IOSPMs and the CANPs are shown in

Figure 8-7a and 8-7b, respectively. Without any cryoprotectants, the signal intensity for CANP is significantly reduced, while sorbitol led to only a minor reduction in signal intensity. CANP freeze-dried with sucrose maintain the same relaxivity of the initial CANP. On the other hand, all samples of the IOSPM showed no reduction in signal intensity, meaning freeze-drying and storage had no impact on the magnetic properties of IOSPMs (Figure 6a). The linear plot of $1/T_2$ (R_2) vs. Fe concentration can be seen in **Figure 8-7c-d** for IOSPMs and CANPs, respectively. The transverse relaxivities (r_2, slope of the curve) of all samples were calculated and tabulated in **Table 8-3**. While there is little difference between the r_2 values of IOSPMs, the transverse relaxivity of CANPs without any cryoprotectant is reduced ~5-fold to 18.7 ± 0.53 sec^{-1} mM^{-1} compared to the control value of 95.5 ± 2.9 sec^{-1} mM^{-1}. This reduction in transverse relaxivity indicates the NPs provide significantly weaker contrast under MRI, indicating low efficacy as a contrast agent. However, using sucrose during the freeze-drying process maintained a similar value to the control at 96.1 ± 6.8 sec^{-1} mM^{-1}, proving that sucrose can not only maintain the size and stability, but also its magnetic properties.

Table 8-3. Transverse relaxivity, r_2 (sec^{-1} mM^{-1}), of NPs evaluated by MRI using a 14 T magnet after freeze-drying and 6-months storage.

	Control	No Cryoprotectant	Sucrose	Sorbitol
IOSPM	98.2 ± 4.7	97.5 ± 3.5	98.8 ± 4.1	101.3 ± 3.9
CANP	95.5 ± 2.9	18.7 ± 0.53	96.1 ± 6.8	70.5 ± 4.6

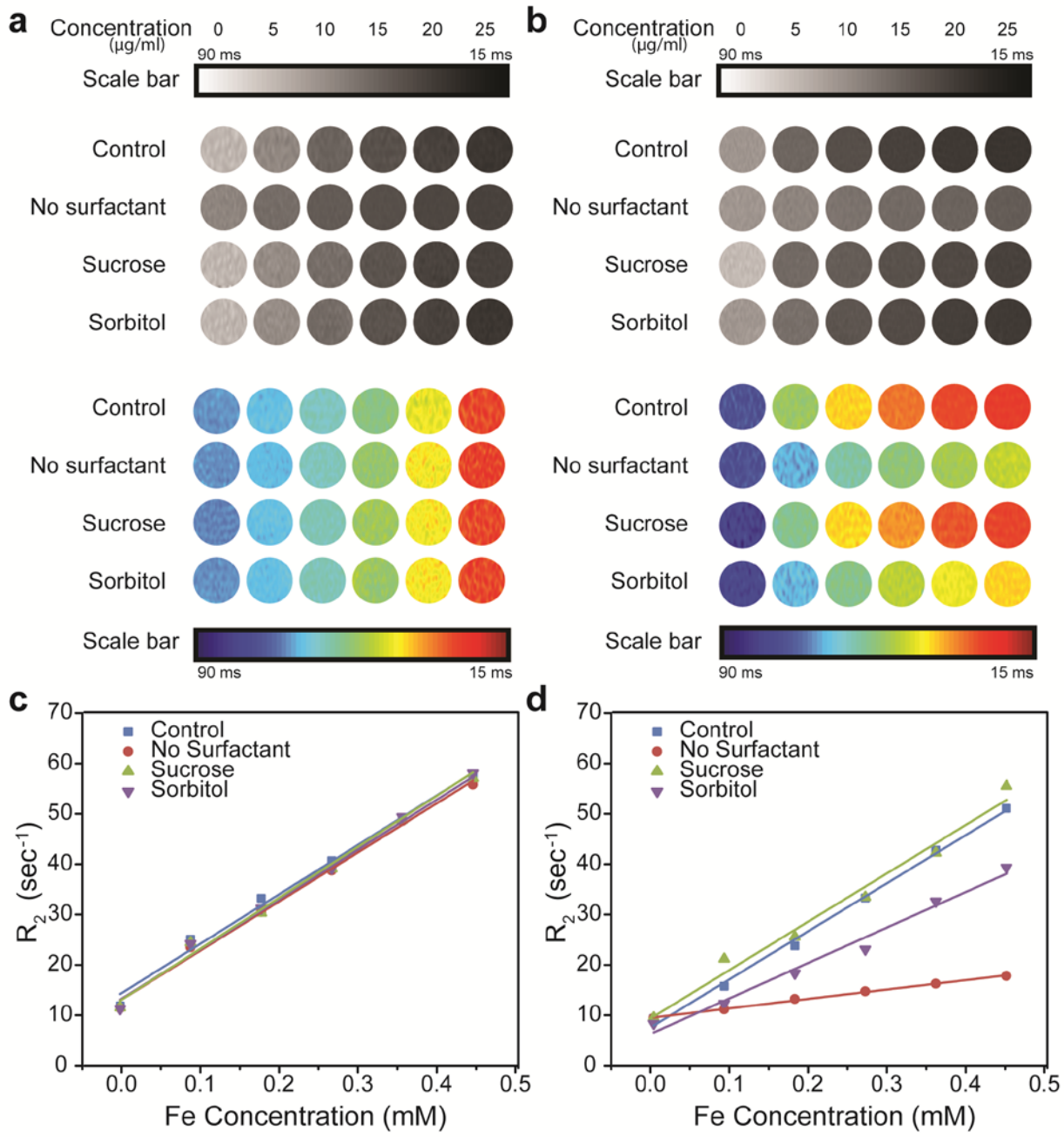

Figure 8-7. Magnetic properties of IOSPM and CANP after freeze-drying and 6 months storage. (a-b): T_2-weighted MR images and R_2 maps of phantom MRI images of (a) IOSPM and (b) CANP at Fe concentrations from 0–25 μg/ml. (c-d): Plot of R_2 vs. Fe concentrations in mM of (c) IOSPM and (d) CANP. The slope of the fitted linear line equates to the specific relaxivity of r_2.

Below their glass transition temperatures, cryoprotectants vitrify and form a glassy matrix, which traps NPs and inhibits aggregation and fusion. Literature reveals the glass transition

temperatures of sugar alcohols are lower than those of sugar molecules. Sorbitol, for example, has a reported glass transition temperature of –1.7 °C, while sucrose has a glass transition temperature of 60 °C.[213-215] All cryoprotectants tested increase the glass transition temperature of the solution over water alone, which has a reported glass transition temperature of –137 °C.[213] We hypothesize that the pronounced stabilizing effect of sucrose is, at least in part, due to its high glass transition temperature relative to the other cryoprotectants studied, allowing vitrification and its protective effects to occur earlier in the freeze-drying process.

The superior stability of IOSPM can be attributed to the presence of a highly dense hydrophilic coating on the surface of the iron oxide core.[23] The strong siloxane bonds between the succinic anhydride silane molecules prevent core-to-core interaction while the hydrophilic PEG chains provide steric stabilization that prevents aggregation. This effective coating likely causes the difference in stability of the 29.0 nm IOSPM and the 72.5 nm CANP, though the minimal information provided by the supplier makes deductions challenging.

8.4 Conclusions

Superparamagnetic iron oxide nanoparticles (SPIONs) have a myriad of applications in the biomedical field. However, their clinical applications are severely limited by their physical and chemical instability in water. Two types of SPIONs — a commercially available NP (CANP) produced by Sigma-Aldrich and one produced by our lab (IOSPM) — were freeze-dried with various cryoprotectants to maintain size, stability, zeta potential, and magnetic properties. NPs were analyzed for their physiochemical properties; IOSPM showed great stability while CANP was prone to aggregation. NPs freeze-dried with sugar variants glucose, dextrose, and especially sucrose, were the most effective in maintaining initial NP size and stability. Sugar alcohols,

mannitol and sorbitol, showed little to no benefit. NPs freeze-dried with 10 wt.% sucrose could be stored up to 6 months in a –20 °C freezer and maintain size, stability, and magnetic properties. These results show that SPIONs can be freeze-dried and stored to improve their shelf-life, taking a step forward in bringing more SPION-based technologies to the clinical setting.

9. Summary of major findings

Iron oxide nanoparticles have shown great potential as an effective material in the biomedical field due to their intrinsic magnetic properties, proven biocompatibility, and flexible surface chemistry that allow versatile applications. However, IONP-based theranostic agents face several challenges for clinical translation, including lack of specificity, insufficient drug loading, and low MR detection limits. The goal of this thesis was to overcome many of the shortcomings of traditional IONP-based theranostic agents by incorporating active targeting for increased specificity, controlled drug release to prohibit side-effects, and to investigate the potential of IONP as an alternative to toxic T_1 contrast agents.

The development of an iron oxide nanoparticle system to target and label dopaminergic neurons was presented in Chapter 5. We demonstrated that IONPs functionalized with targeting agent DN were able to successfully target and label dopaminergic neurons with minimal toxicity. NP-DN showed a 3-fold increase in uptake in dopaminergic neurons over control NP-TR in flow cytometry and confocal imaging experiments. The MR contrast ability of NP-DN, evaluated through cell-based phantom MRI, showed increased contrast over control NP-TR. In Chapter 6, we evaluated IONP functionalized with paclitaxel and folic acid to specifically target and deliver paclitaxel to breast cancer cells. The severe hydrophobicity of paclitaxel severely hinder its clinical application, yet conjugation to IONPs improved its water solubility and achieved high loading (22.8 wt.%) while maintaining a small hydrodynamic size. The conjugation of folic acid enhanced specificity towards breast cancer cells by 2-fold. Additionally, paclitaxel was conjugated via an ester bond that provided controlled release in an acidic environment with minimal release in neutral conditions, minimizing off-target drug release.

Due to the limitation of T_2 contrast agents, IONPs have not found wide spread use in the clinic. As a T_1 contrast agent, GBCAs have been the dominant imaging agent in clinic applications, yet their severe toxicity warrants the development of a more biocompatible alternative. By using the fundamentals that affect T_1 contrast, we developed an IONP-based T_1 contrast agent with a 4-nm core with a PEG coating bound to the core by a phosphine oxide group. The T_1 IONP displayed a very small hydrodynamic size of ~20 nm, with near neutral zeta potential, characteristics ideal for biological application. The T_1 IONP displayed relaxivity values ideal for T_1 contrast agent, with a r_2/r_1 ratio of 5.5, and its capabilities as a T_1 contrast agent were demonstrated using phantom MRI.

Finally, as IONPs transition to the clinic, stability during long-term storage must be considered. Like most NP systems, IONPs are typically kept in aqueous conditions that can hydrolyze and degrade IONPs, which can negatively impact its utility as theranostic agents. Freeze-drying offers a method to store IONPs in powder form that avoids the issues of hydrolysis and degradation, yet freeze-drying applies stresses on NP systems that can be irreversible. Cryoprotectants have been used to minimize freeze-drying stresses, yet their effects on IONPs have not been explored. A variety of cryoprotectants and their effects on maintaining IONP size, stability, zeta potential, and magnetic properties after freeze-drying were evaluated on IONP synthesized in the Zhang laboratory and IONPs that are commercially available. Freeze-drying IONPs in the presence of sucrose at 10 wt.% was determined to be the optimal, maintaining IONP stability in the freeze-dried state for up to 6 months. This improvement in long-term storage is a step forward in bringing more IONP-based technologies to the clinical setting.

10. References

(1) Kievit, F. M.; Zhang, M. *Advanced materials* **2011**, *23*, H217.

(2) Kovtun, O.; Tomlinson, I. D.; Sakrikar, D. S.; Chang, J. C.; Blakely, R. D.; Rosenthal, S. J. *ACS chemical neuroscience* **2011**, *2*, 370.

(3) Brust, P.; van den Hoff, J.; Steinbach, J. *Neuroscience bulletin* **2014**, *30*, 777.

(4) Coenen, H. H.; Elsinga, P. H.; Iwata, R.; Kilbourn, M. R.; Pillai, M. R.; Rajan, M. G.; Wagner, H. N., Jr.; Zaknun, J. J. *Nuclear medicine and biology* **2010**, *37*, 727.

(5) Depboylu, C.; Maurer, L.; Matusch, A.; Hermanns, G.; Windolph, A.; Behe, M.; Oertel, W. H.; Hoglinger, G. U. *NeuroImage* **2013**, *79*, 191.

(6) Sridhar, S.; Mishra, S.; Gulyas, M.; Padmanabhan, P.; Gulyas, B. *International journal of molecular sciences* **2017**, *18*.

(7) Park, J.; An, K.; Hwang, Y.; Park, J. G.; Noh, H. J.; Kim, J. Y.; Park, J. H.; Hwang, N. M.; Hyeon, T. *Nature materials* **2004**, *3*, 891.

(8) Sun, C.; Fang, C.; Stephen, Z.; Veiseh, O.; Hansen, S.; Lee, D.; Ellenbogen, R. G.; Olson, J.; Zhang, M. *Nanomedicine* **2008**, *3*, 495.

(9) Weissleder, R.; Stark, D. D.; Engelstad, B. L.; Bacon, B. R.; Compton, C. C.; White, D. L.; Jacobs, P.; Lewis, J. *AJR. American journal of roentgenology* **1989**, *152*, 167.

(10) Stephen, Z. R.; Kievit, F. M.; Zhang, M. *Materials today* **2011**, *14*, 330.

(11) Blasiak, B.; van Veggel, F. C. J. M.; Tomanek, B. *Journal of Nanomaterials* **2013**, *2013*, 12.

(12) Kim, D.; Kim, J.; Park, Y. I.; Lee, N.; Hyeon, T. *ACS central science* **2018**, *4*, 324.

(13) Kim, J.; Lee, N.; Hyeon, T. *Philosophical transactions. Series A, Mathematical, physical, and engineering sciences* **2017**, *375*.

(14) Lee, S. H.; Kim, B. H.; Na, H. B.; Hyeon, T. *Wiley interdisciplinary reviews. Nanomedicine and nanobiotechnology* **2014**, *6*, 196.

(15) Terreno, E.; Castelli, D. D.; Viale, A.; Aime, S. *Chemical reviews* **2010**, *110*, 3019.

(16) Sun, C.; Du, K.; Fang, C.; Bhattarai, N.; Veiseh, O.; Kievit, F.; Stephen, Z.; Lee, D.; Ellenbogen, R. G.; Ratner, B.; Zhang, M. *ACS Nano* **2010**, *4*, 2402.

(17) Ferrari, M. *Nature Reviews Cancer* **2005**, *5*, 161.

(18) Corot, C.; Petry, K. G.; Trivedi, R.; Saleh, A.; Jonkmanns, C.; Le Bas, J.-F.; Blezer, E.; Rausch, M.; Brochet, B.; Foster-Gareau, P.; Balériaux, D.; Gaillard, S.; Dousset, V. *Investigative radiology* **2004**, *39*, 619.

(19) Wickline, S. A.; Neubauer, A. M.; Winter, P. M.; Caruthers, S. D.; Lanza, G. M. *Journal of Magnetic Resonance Imaging* **2007**, *25*, 667.

(20) Bonnemain, B. *Journal of Drug Targeting* **1998**, *6*, 167.

(21) Wang, Y.-X. J.; Hussain, S. M.; Krestin, G. P. *European Radiology* **2001**, *11*, 2319.

(22) Harisinghani, M. G.; Barentsz, J.; Hahn, P. F.; Deserno, W. M.; Tabatabaei, S.; van de Kaa, C. H.; de la Rosette, J.; Weissleder, R. *N. Engl. J. Med.* **2003**, *348*, 2491.

(23) Fang, C.; Bhattarai, N.; Sun, C.; Zhang, M. *Small* **2009**, *5*, 1637.

(24) Lee, N.; Yoo, D.; Ling, D.; Cho, M. H.; Hyeon, T.; Cheon, J. *Chemical reviews* **2015**, *115*, 10637.

(25) Revia, R. A.; Zhang, M. *Materials today* **2016**, *19*, 157.

(26) Mastrogiacomo, S.; Dou, W.; Jansen, J. A.; Walboomers, X. F. *Molecular Imaging and Biology* **2019**.

(27) Berry, E.; Bulpitt, A. J. 2009.

(28) Hanson, L. G. *Concepts in Magnetic Resonance Part A* **2008**, *32A*, 329.

(29) Goldman, M. *Journal of Magnetic Resonance* **2001**, *149*, 160.

(30) Peng, Y. K., Tsang, S.C.E., Chou, P.T. *Materials today* **2016**, *19*, 336.

(31) Legacz, M., Roepke, K. , Giersig, M. and Pison, U *Advances in Nanoparticles* **2014**, *3*, 41.

(32) Serkova, N. J. *Frontiers in Immunology* **2017**, *8*.

(33) Bai, J.; Wang, J. T. W.; Rubio, N.; Protti, A.; Heidari, H.; Elgogary, R.; Southern, P.; Al-Jamal, W. T.; Sosabowski, J.; Shah, A. M.; Bals, S.; Pankhurst, Q. A.; Al-Jamal, K. T. *Theranostics* **2016**, *6*, 342.

(34) Wan, F.; Wang, L.; Xu, W.; Li, C.; Li, Y.; Zhang, C.; Jiang, L. *Polyhedron* **2018**, *145*, 141.

(35) Hao, R.; Xing, R.; Xu, Z.; Hou, Y.; Gao, S.; Sun, S. *Advanced materials* **2010**, *22*, 2729.

(36) Lauffer, R. B. *Chemical reviews* **1987**, *87*, 901.

(37) Lipinski, M. J.; Briley-Saebo, K. C.; Mani, V.; Fayad, Z. A. *Journal of the American College of Cardiology* **2008**, *52*, 492.

(38) Branca, R. T.; Cleveland, Z. I.; Fubara, B.; Kumar, C. S. S. R.; Maronpot, R. R.; Leuschner, C.; Warren, W. S.; Driehuys, B. *Proceedings of the National Academy of Sciences* **2010**, *107*, 3693.

(39) Rogosnitzky, M.; Branch, S. *BioMetals* **2016**, *29*, 365.

(40) Malikova, H.; Holesta, M. *The Journal of Vascular Access* **2017**, *18*, S1.

(41) Todd, D. J.; Kay, J. *Annual Review of Medicine* **2016**, *67*, 273.

(42) Hasebroock, K. M.; Serkova, N. J. *Expert opinion on drug metabolism & toxicology* **2009**, *5*, 403.

(43) Wang, H.; Revia, R.; Wang, K.; Kant, R. J.; Mu, Q.; Gai, Z.; Hong, K.; Zhang, M. *Advanced materials* **2017**, *29*, 1605416.

(44) Communication, F. D. S. 2015.

(45) Communication, F. D. S. 2017.

(46) Communication, F. D. S. 2018.

(47) Aime, S.; Caravan, P. *J Magn Reson Imaging* **2009**, *30*, 1259.

(48) Taheri, S.; Shah, N. J.; Rosenberg, G. A. *Magnetic resonance imaging* **2016**, *34*, 1034.

(49) Wei, H.; Bruns, O. T.; Kaul, M. G.; Hansen, E. C.; Barch, M.; Wiśniowska, A.; Chen, O.; Chen, Y.; Li, N.; Okada, S.; Cordero, J. M.; Heine, M.; Farrar, C. T.; Montana, D. M.; Adam, G.; Ittrich, H.; Jasanoff, A.; Nielsen, P.; Bawendi, M. G. *Proceedings of the National Academy of Sciences of the United States of America* **2017**, *114*, 2325.

(50) Chiarelli, P. A.; Revia, R. A.; Stephen, Z. R.; Wang, K.; Jeon, M.; Nelson, V.; Kievit, F. M.; Sham, J.; Ellenbogen, R. G.; Kiem, H. P.; Zhang, M. *ACS Nano* **2017**, *11*, 9514.

(51) Briley-Saebo, K.; Bjørnerud, A.; Grant, D.; Ahlstrom, H.; Berg, T.; Kindberg, G. M. *Cell and Tissue Research* **2004**, *316*, 315.

(52) Gu, L.; Fang, R. H.; Sailor, M. J.; Park, J.-H. *ACS nano* **2012**, *6*, 4947.

(53) Pouliquen, D.; Le Jeune, J. J.; Perdrisot, R.; Ermias, A.; Jallet, P. *Magnetic Resonance Imaging* **1991**, *9*, 275.

(54) Moffat, B. A., Ramachandra Reddy, G., McConville, P., Hall, D., Chenevert., T.L., Kopelman, R.R., Philber, M., Weissleder, R., Rehemtulla, A., Ross, B.D. *Molecular Imaging* **2003**, *2*, 324.

(55) Heyn, C.; Bowen, C. V.; Rutt, B. K.; Foster, P. J. *Magnetic resonance in medicine* **2005**, *53*, 312.

(56) Cole, A. J.; David, A. E.; Wang, J.; Galbán, C. J.; Hill, H. L.; Yang, V. C. *Biomaterials* **2010**, *32*, 2183.

(57) Moteki, T.; Sekine, T. *Journal of Magnetic Resonance Imaging* **2004**, *19*, 82.

(58) Kumano, S.; Murakami, T.; Kim, T.; Hori, M.; Okada, A.; Sugiura, T.; Noguchi, Y.; Kawata, S.; Tomoda, K.; Nakamura, H. *American Journal of Roentgenology* **2003**, *181*, 1335.

(59) Fukukura, Y.; Kamiyama, T.; Takumi, K.; Shindo, T.; Higashi, R.; Nakajo, M. *Journal of Magnetic Resonance Imaging* **2010**, *31*, 607.

(60) Pysz, M. A.; Gambhir, S. S.; Willmann, J. K. *Clin Radiol* **2010**, *65*, 500.

(61) Bartlett, D. W.; Su, H.; Hildebrandt, I. J.; Weber, W. A.; Davis, M. E. *Proceedings of the National Academy of Sciences of the United States of America* **2007**, *104*, 15549.

(62) Lee, H. Y.; Li, Z.; Chen, K.; Hsu, A. R.; Xu, C. J.; Xie, J.; Sun, S. H.; Chen, X. Y. *J. Nucl. Med.* **2008**, *49*, 1371.

(63) Xie, J.; Chen, K.; Huang, J.; Lee, S.; Wang, J. H.; Gao, J.; Li, X. G.; Chen, X. Y. *Biomaterials* **2010**, *31*, 3016.

(64) Longmire, M.; Choyke, P. L.; Kobayashi, H. *Nanomedicine* **2008**, *3*, 703.

(65) Kievit, F. M.; Veiseh, O.; Bhattarai, N.; Fang, C.; Gunn, J. W.; Lee, D.; Ellenbogen, R. G.; Olson, J. M.; Zhang, M. *Advanced functional materials* **2009**, *19*, 2244.

(66) Chiarelli, P. A.; Kievit, F. M.; Zhang, M.; Ellenbogen, R. G. *Surg Neurol Int* **2015**, *6*, S45.

(67) Nakamura, Y.; Mochida, A.; Choyke, P. L.; Kobayashi, H. *Bioconjugate chemistry* **2016**, *27*, 2225.

(68) Chen, L.; Zang, F.; Wu, H.; Li, J.; Xie, J.; Ma, M.; Gu, N.; Zhang, Y. *Nanoscale* **2018**, *10*, 1788.

(69) Israel, L. L. *EBioMedicine* **2018**, *30*, 7.

(70) Peer, D.; Karp, J. M.; Hong, S.; Farokhzad, O. C.; Margalit, R.; Langer, R. *Nature nanotechnology* **2007**, *2*, 751.

(71) Matsumura, Y.; Maeda, H. *Cancer Research* **1986**, *46*, 6387.

(72) Sunderland, C. J.; Steiert, M.; Talmadge, J. E.; Derfus, A. M.; Barry, S. E. *Drug Development Research* **2006**, *67*, 70.

(73) Alexis, F.; Rhee, J. W.; Richie, J. P.; Radovic-Moreno, A. F.; Langer, R.; Farokhzad, O. C. *Urol Oncol* **2008**, *26*, 74.

(74) Yang, R.; An, Y.; Miao, F.; Li, M.; Liu, P.; Tang, Q. *International journal of nanomedicine* **2014**, *9*, 4231.

(75) Kumar, M.; Singh, G.; Arora, V.; Mewar, S.; Sharma, U.; Jagannathan, N. R.; Sapra, S.; Dinda, A. K.; Kharbanda, S.; Singh, H. *International journal of nanomedicine* **2012**, *7*, 3503.

(76) Liu, W.; Nie, L.; Li, F.; Aguilar, Z. P.; Xu, H.; Xiong, Y.; Fu, F.; Xu, H. *Biomaterials science* **2016**, *4*, 159.

(77) Zwicke, G. L.; Mansoori, G. A.; Jeffery, C. J. *Nano reviews* **2012**, *3*.

(78) DeBin, J. A.; Strichartz, G. R. *Toxicon* **1991**, *29*, 1403.

(79) Larsen, B., Haag, MA, Serkova, NJ, Shroyer, KR, Stoldt, CR *Nanotechnology* **2008**, *19*.

(80) Roch, A.; Gossuin, Y.; Muller, R. N.; Gillis, P. *Journal of Magnetism and Magnetic Materials* **2005**, *293*, 532.

(81) Nadeem, M.; Ahmad, M.; Akhtar, M. S.; Shaari, A.; Riaz, S.; Naseem, S.; Masood, M.; Saeed, M. A. *PloS one* **2016**, *11*, e0158084.

(82) Manivasagan, P.; Bharathiraja, S.; Bui, N. Q.; Lim, I. G.; Oh, J. *International journal of pharmaceutics* **2016**, *511*, 367.

(83) Vismara, E.; Bongio, C.; Coletti, A.; Edelman, R.; Serafini, A.; Mauri, M.; Simonutti, R.; Bertini, S.; Urso, E.; Assaraf, Y. G.; Livney, Y. D. *Molecules* **2017**, *22*.

(84) Mu, Q.; Jeon, M.; Hsiao, M. H.; Patton, V. K.; Wang, K.; Press, O. W.; Zhang, M. *Advanced healthcare materials* **2015**, *4*, 1236.

(85) Ding, Y.; Zhou, Y. Y.; Chen, H.; Geng, D. D.; Wu, D. Y.; Hong, J.; Shen, W. B.; Hang, T. J.; Zhang, C. *Biomaterials* **2013**, *34*, 10217.

(86) Hsiao, M. H.; Mu, Q. X.; Stephen, Z. R.; Fang, C.; Zhang, M. Q. *ACS Macro Lett.* **2015**, *4*, 403.

(87) Caldorera-Moore, M. E.; Liechty, W. B.; Peppas, N. A. *Accounts of chemical research* **2011**, *44*, 1061.

(88) Pourjavadi, A.; Hosseini, S. H.; Alizadeh, M.; Bennett, C. *Colloid Surf. B-Biointerfaces* **2014**, *116*, 49.

(89) Kievit, F. M.; Wang, F. Y.; Fang, C.; Mok, H.; Wang, K.; Silber, J. R.; Ellenbogen, R. G.; Zhang, M. Q. *Journal of Controlled Release* **2011**, *152*, 76.

(90) Hardiansyah, A.; Yang, M.-C.; Liu, T.-Y.; Kuo, C.-Y.; Huang, L.-Y.; Chan, T.-Y. *Nanoscale Res Lett* **2017**, *12*, 355.

(91) Khandhar, A. P.; Wilson, G. J.; Kaul, M. G.; Salamon, J.; Jung, C.; Krishnan, K. M. *Journal of Biomedical Materials Research Part A* **2018**, *106*, 2440.

(92) Tromsdorf, U. I.; Bruns, O. T.; Salmen, S. C.; Beisiegel, U.; Weller, H. *Nano letters* **2009**, *9*, 4434.

(93) Kucheryavy, P.; He, J.; John, V. T.; Maharjan, P.; Spinu, L.; Goloverda, G. Z.; Kolesnichenko, V. L. *Langmuir : the ACS journal of surfaces and colloids* **2013**, *29*, 710.

(94) Chen, L.; Xie, J.; Wu, H.; Li, J.; Wang, Z.; Song, L.; Zang, F.; Ma, M.; Gu, N.; Zhang, Y. *Journal of Nanomaterials* **2018**, *2018*, 9.

(95) Kim, B. H.; Lee, N.; Kim, H.; An, K.; Park, Y. I.; Choi, Y.; Shin, K.; Lee, Y.; Kwon, S. G.; Na, H. B.; Park, J.-G.; Ahn, T.-Y.; Kim, Y.-W.; Moon, W. K.; Choi, S. H.; Hyeon, T. *J. Am. Chem. Soc.* **2011**, *133*, 12624.

(96) Baaziz, W.; Pichon, B. P.; Fleutot, S.; Liu, Y.; Lefevre, C.; Greneche, J.-M.; Toumi, M.; Mhiri, T.; Begin-Colin, S. *The Journal of Physical Chemistry C* **2014**, *118*, 3795.

(97) Daou, T. J.; Grenèche, J. M.; Pourroy, G.; Buathong, S.; Derory, A.; Ulhaq-Bouillet, C.; Donnio, B.; Guillon, D.; Begin-Colin, S. *Chem. Mat.* **2008**, *20*, 5869.

(98) Daou, T. J.; Greneche, J.-M.; Lee, S.-J.; Lee, S.; Lefevre, C.; Bégin-Colin, S.; Pourroy, G. *The Journal of Physical Chemistry C* **2010**, *114*, 8794.

(99) Linderoth, S.; Hendriksen, P. V.; Bo/dker, F.; Wells, S.; Davies, K.; Charles, S. W.; Mo/rup, S. *Journal of Applied Physics* **1994**, *75*, 6583.

(100) Pereira, A. M.; Pereira, C.; Silva, A. S.; Schmool, D. S.; Freire, C.; Grenèche, J.-M.; Araújo, J. P. *Journal of Applied Physics* **2011**, *109*, 114319.

(101) Mohapatra, J.; Mitra, A.; Tyagi, H.; Bahadur, D.; Aslam, M. *Nanoscale* **2015**, *7*, 9174.

(102) Macher, T.; Totenhagen, J.; Sherwood, J.; Qin, Y.; Gurler, D.; Bolding, M. S.; Bao, Y. *Advanced functional materials* **2015**, *25*, 490.

(103) Yang, L.; Wang, Z.; Ma, L.; Li, A.; Xin, J.; Wei, R.; Lin, H.; Wang, R.; Chen, Z.; Gao, J. *ACS Nano* **2018**, *12*, 4605.

(104) Dar, M. I.; Shivashankar, S. A. *RSC Advances* **2014**, *4*, 4105.

(105) Park, J. C.; Lee, G. T.; Kim, H.-K.; Sung, B.; Lee, Y.; Kim, M.; Chang, Y.; Seo, J. H. *ACS applied materials & interfaces* **2018**, *10*, 25080.

(106) Han, G.; Deng, Y.; Sun, J.; Ling, J.; Shen, Z. *Exp Ther Med* **2015**, *9*, 1561.

(107) Peng, Y.-K.; Liu, C.-L.; Chen, H.-C.; Chou, S.-W.; Tseng, W.-H.; Tseng, Y.-J.; Kang, C.-C.; Hsiao, J.-K.; Chou, P.-T. *J. Am. Chem. Soc.* **2013**, *135*, 18621.

(108) Zhang, W.; Liu, L.; Chen, H.; Hu, K.; Delahunty, I.; Gao, S.; Xie, J. *Theranostics* **2018**, *8*, 2521.

(109) Caravan, P. *Chemical Society Reviews* **2006**, *35*, 512.

(110) Caravan, P.; Farrar, C. T.; Frullano, L.; Uppal, R. *Contrast Media Mol Imaging* **2009**, *4*, 89.

(111) Lavalette, D.; Tétreau, C.; Tourbez, M.; Blouquit, Y. *Biophysical journal* **1999**, *76*, 2744.

(112) LaConte, L. E. W.; Nitin, N.; Zurkiya, O.; Caruntu, D.; O'Connor, C. J.; Hu, X.; Bao, G. *Journal of Magnetic Resonance Imaging* **2007**, *26*, 1634.

(113) Hajesmaeelzadeh, F.; Shanehsazzadeh, S.; Grüttner, C.; Daha, F. J.; Oghabian, M. A. *Iran J Basic Med Sci* **2016**, *19*, 166.

(114) Tong, S.; Hou, S.; Zheng, Z.; Zhou, J.; Bao, G. *Nano letters* **2010**, *10*, 4607.

(115) Dumas, S.; Jacques, V.; Sun, W.-C.; Troughton, J. S.; Welch, J. T.; Chasse, J. M.; Schmitt-Willich, H.; Caravan, P. *Investigative radiology* **2010**, *45*, 600.

(116) Zeng, J.; Jing, L.; Hou, Y.; Jiao, M.; Qiao, R.; Jia, Q.; Liu, C.; Fang, F.; Lei, H.; Gao, M. *Advanced materials* **2014**, *26*, 2694.

(117) Smolensky, E. D.; Park, H.-Y. E.; Berquó, T. S.; Pierre, V. C. *Contrast Media Mol Imaging* **2011**, *6*, 189.

(118) Palma, S. I. C. J.; Marciello, M.; Carvalho, A.; Veintemillas-Verdaguer, S.; Morales, M. d. P.; Roque, A. C. A. *Journal of colloid and interface science* **2015**, *437*, 147.

(119) Herea, D. D.; Chiriac, H. *One-step preparation and surface activation of magnetic iron oxide nanoparticles for bio-medical applications*, 2008; Vol. 2.

(120) Costo, R.; Morales, M. P.; Veintemillas-Verdaguer, S. *Journal of Applied Physics* **2015**, *117*, 064311.

(121) Nagesha, D. K.; Plouffe, B. D.; Phan, M.; Lewis, L. H.; Sridhar, S.; Murthy, S. K. *Journal of Applied Physics* **2009**, *105*, 07B317.

(122) Zhou, P.; Sun, X.; Zhang, Z. *Acta Pharmaceutica Sinica B* **2014**, *4*, 37.

(123) Blanco, E.; Shen, H.; Ferrari, M. *Nature biotechnology* **2015**, *33*, 941.

(124) Longmire, M.; Choyke, P. L.; Kobayashi, H. *Nanomedicine (London, England)* **2008**, *3*, 703.

(125) Gupta, V.; Trivedi, P. In *Lipid Nanocarriers for Drug Targeting*; Grumezescu, A. M., Ed.; William Andrew Publishing: 2018, p 563.

(126) Honair, S., Zahir, F. *Tropical Journal of Pharmaceutical Research* **2013**, *12*, 255.

(127) Xia, Y.; Xiong, Y.; Lim, B.; Skrabalak, S. E. *Angewandte Chemie (International ed. in English)* **2009**, *48*, 60.

(128) Li, Z.; Tan, B.; Allix, M.; Cooper, A. I.; Rosseinsky, M. J. *Small* **2008**, *4*, 231.

(129) Park, J.; Kang, E.; Son, S. U.; Park, H. M.; Lee, M. K.; Kim, J.; Kim, K. W.; Noh, H.-J.; Park, J.-H.; Bae, C. J.; Park, J.-G.; Hyeon, T. *Advanced materials* **2005**, *17*, 429.

(130) Murray, C. B.; Sun, S.; Gaschler, W.; Doyle, H.; Betley, T. A.; Kagan, C. R. *IBM Journal of Research and Development* **2001**, *45*, 47.

(131) Herman, D. A. J.; Ferguson, P.; Cheong, S.; Hermans, I. F.; Ruck, B. J.; Allan, K. M.; Prabakar, S.; Spencer, J. L.; Lendrum, C. D.; Tilley, R. D. *Chemical communications* **2011**, *47*, 9221.

(132) Becker, R.; Döring, W. *Annalen der Physik* **1935**, *416*, 719.

(133) Polte, J. *CrystEngComm* **2015**, *17*, 6809.

(134) LaMer, V. K.; Dinegar, R. H. *J. Am. Chem. Soc.* **1950**, *72*, 4847.

(135) Mer, V. K. L. *Industrial & Engineering Chemistry* **1952**, *44*, 1270.

(136) Reiss, H. *The Journal of Chemical Physics* **1951**, *19*, 482.

(137) Seibyl, J.; Jennings, D.; Tabamo, R.; Marek, K. *Minerva medica* **2005**, *96*, 353.

(138) Ba, F.; Martin, W. R. *Parkinsonism & related disorders* **2015**, *21*, 87.

(139) Cummings, J. L.; Henchcliffe, C.; Schaier, S.; Simuni, T.; Waxman, A.; Kemp, P. *Brain : a journal of neurology* **2011**, *134*, 3146.

(140) Huang, W. S.; Chiang, Y. H.; Lin, J. C.; Chou, Y. H.; Cheng, C. Y.; Liu, R. S. *Journal of nuclear medicine : official publication, Society of Nuclear Medicine* **2003**, *44*, 999.

(141) Kimmel, H. L.; Nye, J. A.; Voll, R.; Mun, J.; Stehouwer, J.; Goodman, M. M.; Votaw, J. R.; Carroll, F. I.; Howell, L. L. *Synapse* **2012**, *66*, 501.

(142) Wang, W.; Sonders, M. S.; Ukairo, O. T.; Scott, H.; Kloetzel, M. K.; Surratt, C. K. *Molecular pharmacology* **2003**, *64*, 430.

(143) Booth, T. C.; Nathan, M.; Waldman, A. D.; Quigley, A. M.; Schapira, A. H.; Buscombe, J. *AJNR. American journal of neuroradiology* **2015**, *36*, 229.

(144) Dodel, R. C.; Hoffken, H.; Moller, J. C.; Bornschein, B.; Klockgether, T.; Behr, T.; Oertel, W. H.; Siebert, U. *Movement disorders : official journal of the Movement Disorder Society* **2003**, *18 Suppl 7*, S52.

(145) *Clinical neuropharmacology* **2000**, *23*, 34.

(146) Benamer, T. S.; Patterson, J.; Grosset, D. G.; Booij, J.; de Bruin, K.; van Royen, E.; Speelman, J. D.; Horstink, M. H.; Sips, H. J.; Dierckx, R. A.; Versijpt, J.; Decoo, D.; Van Der Linden, C.; Hadley, D. M.; Doder, M.; Lees, A. J.; Costa, D. C.; Gacinovic, S.; Oertel, W. H.; Pogarell, O.; Hoeffken, H.; Joseph, K.; Tatsch, K.; Schwarz, J.; Ries, V. *Movement disorders : official journal of the Movement Disorder Society* **2000**, *15*, 503.

(147) Booij, J.; Speelman, J. D.; Horstink, M. W.; Wolters, E. C. *European journal of nuclear medicine* **2001**, *28*, 266.

(148) de Verdal, M.; Renard, D.; Collombier, L.; Boudousq, V.; Kotzki, P. O.; Labauge, P.; Castelnovo, G. *European journal of neurology* **2013**, *20*, 382.

(149) Utiumi, M. A.; Felicio, A. C.; Borges, C. R.; Braatz, V. L.; Rezende, S. A.; Munhoz, R. P.; Bressan, R. A.; Ferraz, H. B.; Teive, H. A. *Arquivos de neuro-psiquiatria* **2012**, *70*, 667.

(150) Catafau, A. M.; Tolosa, E.; Da, T. C. U. P. S. S. G. *Movement disorders : official journal of the Movement Disorder Society* **2004**, *19*, 1175.

(151) Marshall, V. L.; Patterson, J.; Hadley, D. M.; Grosset, K. A.; Grosset, D. G. *Nuclear medicine communications* **2006**, *27*, 933.

(152) Marshall, V. L.; Reininger, C. B.; Marquardt, M.; Patterson, J.; Hadley, D. M.; Oertel, W. H.; Benamer, H. T.; Kemp, P.; Burn, D.; Tolosa, E.; Kulisevsky, J.; Cunha, L.; Costa, D.; Booij, J.; Tatsch, K.; Chaudhuri, K. R.; Ulm, G.; Pogarell, O.; Hoffken, H.; Gerstner, A.; Grosset, D. G. *Movement disorders : official journal of the Movement Disorder Society* **2009**, *24*, 500.

(153) Cha, J. H.; Zou, M.-F.; Adkins, E. M.; Rasmussen, S. G. F.; Loland, C. J.; Schoenenberger, B.; Gether, U.; Newman, A. H. *Journal of medicinal chemistry* **2005**, *48*, 7513.

(154) Park, J. A., K.; Hwang, Y.; Park, J.-G.; Noh, H.-J.; Kim, J.-Y.; Park, J.-H.; Hwang, N.-M.; Hyeon, T *Nat. Mater.* **2004**, *3*, 891.

(155) Stephen, Z. R.; Kievit, F. M.; Veiseh, O.; Chiarelli, P. A.; Fang, C.; Wang, K.; Hatzinger, S. J.; Ellenbogen, R. G.; Silber, J. R.; Zhang, M. *ACS Nano* **2014**, *8*, 10383.

(156) Huang, X.; Teng, X.; Chen, D.; Tang, F.; He, J. *Biomaterials* **2010**, *31*, 438.

(157) Jiang, Y.; Huo, S.; Mizuhara, T.; Das, R.; Lee, Y. W.; Hou, S.; Moyano, D. F.; Duncan, B.; Liang, X. J.; Rotello, V. M. *ACS Nano* **2015**, *9*, 9986.

(158) Truong, N. P.; Whittaker, M. R.; Mak, C. W.; Davis, T. P. *Expert opinion on drug delivery* **2015**, *12*, 129.

(159) Park, S. U.; Ferrer, J. V.; Javitch, J. A.; Kuhn, D. M. *The Journal of Neuroscience* **2002**, *22*, 4399.

(160) Robbins, A. K.; Horlick, R. A. *BioTechniques* **1998**, *25*, 240.

(161) Ferrer, J. V.; Javitch, J. A. *Proceedings of the National Academy of Sciences* **1998**, *95*, 9238.

(162) Chen, N.; Ferrer, J. V.; Javitch, J. A.; Justice, J. B. *Journal of Biological Chemistry* **2000**, *275*, 1608.

(163) Hastrup, H.; Karlin, A.; Javitch, J. A. *Proceedings of the National Academy of Sciences* **2001**, *98*, 10055.

(164) Eriksen, J.; Bjørn-Yoshimoto, W. E.; Jørgensen, T. N.; Newman, A. H.; Gether, U. *J Biol Chem* **2010**, *285*, 27289.

(165) Eriksen, J.; Rasmussen, S. G. F.; Rasmussen, T. N.; Vaegter, C. B.; Cha, J. H.; Zou, M.-F.; Newman, A. H.; Gether, U. *The Journal of neuroscience : the official journal of the Society for Neuroscience* **2009**, *29*, 6794.

(166) Gottesman, M. M.; Fojo, T.; Bates, S. E. *Nature reviews. Cancer* **2002**, *2*, 48.

(167) Jordan, M. A.; Wilson, L. *Nature reviews. Cancer* **2004**, *4*, 253.

(168) Ma, P.; Mumper, R. J. *Journal of nanomedicine & nanotechnology* **2013**, *4*, 1000164.

(169) Gelderblom, H.; Verweij, J.; Nooter, K.; Sparreboom, A. *European journal of cancer* **2001**, *37*, 1590.

(170) Kipp, J. E. *International journal of pharmaceutics* **2004**, *284*, 109.

(171) Bernabeu, E., Cagel, M., Lagomarsino, Ed., Moretton, M., Chiappetta, D. A. *International Journal of Pharmaceutics* **2017**, *526*, 474.

(172) Feng, S. T.; Li, J.; Luo, Y.; Yin, T.; Cai, H.; Wang, Y.; Dong, Z.; Shuai, X.; Li, Z. P. *PloS one* **2014**, *9*, e100732.

(173) Duan, X.; Xiao, J.; Yin, Q.; Zhang, Z.; Yu, H.; Mao, S.; Li, Y. *ACS Nano* **2013**, *7*, 5858.

(174) Hwang, A. A.; Lee, B. Y.; Clemens, D. L.; Dillon, B. J.; Zink, J. I.; Horwitz, M. A. *Small* **2015**, *11*, 5066.

(175) Jin, X.; Li, M.; Yin, L.; Zhou, J.; Zhang, Z.; Lv, H. *Nanomedicine : nanotechnology, biology, and medicine* **2017**, *13*, 1105.

(176) Ye, L.; He, J.; Hu, Z.; Dong, Q.; Wang, H.; Fu, F.; Tian, J. *Food and chemical toxicology : an international journal published for the British Industrial Biological Research Association* **2013**, *52*, 200.

(177) Nguyen, V. D., Han, J., Go, G., Zhen, J., Zheng, S., Le, V. H., Park, J.O., Park, S. *Sensors and Actuators B: Chemical* **2016**, *240*, 1226.

(178) Gradishar, W. J. *Expert opinion on pharmacotherapy* **2006**, *7*, 1041.

(179) Sofias, A. M.; Dunne, M.; Storm, G.; Allen, C. *Advanced drug delivery reviews* **2017**.

(180) Vlahov, I. R.; Leamon, C. P. *Bioconjugate chemistry* **2012**, *23*, 1357.

(181) Deutsch, H. M.; Glinski, J. A.; Hernandez, M.; Haugwitz, R. D.; Narayanan, V. L.; Suffness, M.; Zalkow, L. H. *Journal of medicinal chemistry* **1989**, *32*, 788.

(182) Nigst, T. A.; Antipova, A.; Mayr, H. *The Journal of organic chemistry* **2012**, *77*, 8142.

(183) Roberts, I.; Urey, H. C. *J. Am. Chem. Soc.* **1939**, *61*, 2584.

(184) Xiao, K.; Li, Y.; Luo, J.; Lee, J. S.; Xiao, W.; Gonik, A. M.; Agarwal, R. G.; Lam, K. S. *Biomaterials* **2011**, *32*, 3435.

(185) Motlagh, N. S. D., Parvin, P., Ghasemi, F., Atyabi, F. *Biomedical Optics Express* **2016**, *7*, 2400.

(186) Liu, D.; Wu, W.; Chen, X.; Wen, S.; Zhang, X.; Ding, Q.; Teng, G.; Gu, N. *Nanoscale* **2012**, *4*, 2306.

(187) Mu, Q.; Kievit, F. M.; Kant, R. J.; Lin, G.; Jeon, M.; Zhang, M. *Nanoscale* **2015**, *7*, 18010.

(188) Na, H. B.; Lee, I. S.; Seo, H.; Park, Y. I.; Lee, J. H.; Kim, S.-W.; Hyeon, T. *Chemical communications* **2007**, 5167.

(189) Kwon, S. G.; Piao, Y.; Park, J.; Angappane, S.; Jo, Y.; Hwang, N.-M.; Park, J.-G.; Hyeon, T. *J. Am. Chem. Soc.* **2007**, *129*, 12571.

(190) Kievit, F. M.; Zhang, M. *Accounts of chemical research* **2011**, *44*, 853.

(191) Cosgrove, T. *Colloid science : principles, methods and applications*; 2nd ed.; Wiley: Chichester, West Sussex, 2010.

(192) Wang, Y.; Zheng, Y.; Zhang, L.; Wang, Q.; Zhang, D. *Journal of controlled release : official journal of the Controlled Release Society* **2013**, *172*, 1126.

(193) Wu, L.; Zhang, J.; Watanabe, W. *Advanced drug delivery reviews* **2011**, *63*, 456.

(194) Xu, L.; Liang, H. W.; Yang, Y.; Yu, S. H. *Chemical reviews* **2018**, *118*, 3209.

(195) Hak, S.; Goa, P. E.; Stenmark, S.; Bjerkholt, F. F.; Haraldseth, O. *Magnetic resonance in medicine* **2015**, *74*, 858.

(196) Abdelwahed, W.; Degobert, G.; Stainmesse, S.; Fessi, H. *Advanced drug delivery reviews* **2006**, *58*, 1688.

(197) Bozdag, S.; Dillen, K.; Vandervoort, J.; Ludwig, A. *The Journal of pharmacy and pharmacology* **2005**, *57*, 699.

(198) Layre, A. M.; Couvreur, P.; Richard, J.; Requier, D.; Eddine Ghermani, N.; Gref, R. *Drug development and industrial pharmacy* **2006**, *32*, 839.

(199) Schwarz, C.; Mehnert, W. *International journal of pharmaceutics* **1997**, *157*, 171.

(200) Liu, A.; Watanabe, T.; Honma, I.; Wang, J.; Zhou, H. *Biosensors & bioelectronics* **2006**, *22*, 694.

(201) Okamoto, H.; Mori, K.; Ohtsuka, K.; Ohuchi, H.; Ishii, H. *Pharmaceutical research* **1997**, *14*, 1181.

(202) Chang, L. L.; Pikal, M. J. *Journal of pharmaceutical sciences* **2009**, *98*, 2886.

(203) Tang, X.; Pikal, M. J. *Pharmaceutical research* **2004**, *21*, 191.

(204) Dulieu, C.; Bazile, D. *Pharmaceutical research* **2005**, *22*, 285.

(205) Chiarelli, P. A.; Revia, R. A.; Stephen, Z. R.; Wang, K.; Jeon, M.; Nelson, V.; Kievit, F. M.; Sham, J.; Ellenbogen, R. G.; Kiem, H.-P.; Zhang, M. *ACS nano* **2017**, *11*, 9514.

(206) Wang, K.; Kievit, F. M.; Sham, J. G.; Jeon, M.; Stephen, Z. R.; Bakthavatsalam, A.; Park, J. O.; Zhang, M. *Small (Weinheim an der Bergstrasse, Germany)* **2016**, *12*, 477.

(207) Wang, K.; Kievit, F. M.; Jeon, M.; Silber, J. R.; Ellenbogen, R. G.; Zhang, M. *Advanced healthcare materials* **2015**, *4*, 2719.

(208) Mu, Q.; Jeon, M.; Hsiao, M.-H.; Patton, V. K.; Wang, K.; Press, O. W.; Zhang, M. *Advanced healthcare materials* **2015**, *4*, 1236.

(209) Fang, C.; Kievit, F. M.; Veiseh, O.; Stephen, Z. R.; Wang, T.; Lee, D.; Ellenbogen, R. G.; Zhang, M. *Journal of controlled release : official journal of the Controlled Release Society* **2012**, *162*, 233.

(210) Fang, C.; Veiseh, O.; Kievit, F.; Bhattarai, N.; Wang, F.; Stephen, Z.; Li, C.; Lee, D.; Ellenbogen, R. G.; Zhang, M. *Nanomedicine* **2010**, *5*, 1357.

(211) Berg, J. M.; Romoser, A.; Banerjee, N.; Zebda, R.; Sayes, C. M. *Nanotoxicology* **2009**, *3*, 276.

(212) Vallabani, N. V. S.; Singh, S. *3 Biotech* **2018**, *8*, 279.

(213) Katkov, II; Levine, F. *Cryobiology* **2004**, *49*, 62.

(214) Simperler, A.; Kornherr, A.; Chopra, R.; Bonnet, P. A.; Jones, W.; Motherwell, W. D.; Zifferer, G. *The journal of physical chemistry. B* **2006**, *110*, 19678.

(215) Yu, L.; Mishra, D. S.; Rigsbee, D. R. *Journal of pharmaceutical sciences* **1998**, *87*, 774.